Microstructure control and iodine doping of bismuth telluride

Thesis by

Nicholas A. Heinz

In Partial Fulfillment of the Requirements
for the Degree of
Doctor of Philosophy

California Institute of Technology
Pasadena, California

2014
(Defended June 11, 2014)

Acknowledgments

I would like to start by thanking my adviser Jeff Snyder. I'll always be grateful to him for taking a chance on somebody who, according to him, has a strong resemblance to Steve Buscemi, which I later learned meant that he thought I was "funny lookin', but in a general sort of way." I also need to thank Teruyuki Ikeda, as he was my mentor for a significant portion of my time at Caltech, and has always been an unending source of information regarding metallurgy and microstructure.

I owe a great deal to both Doug Medlin and Josh Sugar for helping me learn how to operate a transmission electron microscope without too many headaches. I greatly enjoyed the time I spent at Sandia National Laboratories in Livermore, California.

To Eric Toberer and Andrew May for their significant contributions prior to and after my joining the group. It was a massive undertaking getting everything in the laboratory up and running, and then continuing the functionality long after it suited their needs.

I wish to thank everyone who has ever helped with any project big or small that I've worked on over the last six years. The entire lab is indebted to Kasper Borup for the endless supply of help he provided regarding instrumentation. The same can be said of Wolfgang Zeier who is the group's resident refinement specialist. Also, Zachary Gibbs and his love of computer science led to multiple versions of modeling software that benefited many more people other than myself. I want to thank everybody else in the Snyder group and past visitors too. It's the group itself that makes science fun, and I think everyone has done a great job, and will continue to do so.

My family has been an extremely important part of my academic career as well. My parents and brother always kept me humble and sane, while my sister kept things colorful. I have to thank the friends that I've made while being at Caltech as well, in particular Jonny, Jenne, Andrew, Aaron, Tara, Kim and Tim good times were had, and more to come.

I owe an enormous amount to Randell Makinson as well. He took me in ten years ago when I first started at USC, and I was extremely fortunate to be a part of his life. I know the feeling is mutual, and I'll always miss you.

Last but not least, to the man who has provided the finest of $4 lunches to world for the last 4 years, I couldn't have done it without you, Ernie.

Abstract

On the materials scale, thermoelectric efficiency is defined by the dimensionless figure of merit zT. This value is made up of three material components in the form $zT = T\alpha^2/\rho\kappa$, where α is the Seebeck coefficient, ρ is the electrical resistivity, and κ is the total thermal conductivity. Therefore, improving zT would require the reduction of κ and ρ while increasing α. However, due to the inter-relation of the electrical and thermal properties of materials, typical routes to thermoelectric enhancement come in one of two forms. The first is to isolate the electronic properties and increase α without negatively affecting ρ. Techniques like electron filtering, quantum confinement, and density of states distortions have been proposed to enhance the Seebeck coefficient in thermoelectric materials. However, it has been difficult to prove the efficacy of these techniques. More recently, efforts to manipulate the band degeneracy in semiconductors has been explored as a means to enhance α.

The other route to thermoelectric enhancement is through minimizing the thermal conductivity, κ. More specifically, thermal conductivity can be broken into two parts, an electronic and lattice term, κ_e and κ_l, respectively. From a functional materials standpoint, the reduction in lattice thermal conductivity should have a minimal effect on the electronic properties. Most routes incorporate techniques that focus on the reduction of the lattice thermal conductivity. The components that make up κ_l ($\kappa_l = \frac{1}{3}C\nu l$) are the heat capacity, C, phonon group velocity (ν), and phonon mean free path (l). Since the difficulty is extreme in altering the heat capacity and group velocity, the phonon mean free path is most often the source of reduction.

Past routes to decreasing the phonon mean free path have been through alloying and grain size reduction. However, in these techniques the electron mobility is often negatively affected because in alloying any perturbation to the periodic potential can cause additional adverse carrier scattering. Grain size reduction has been another successful route to enhancing zT because of the significant difference in electron and phonon mean free paths. However, grain size reduction is erratic in anisotropic materials due to the orientation-dependent transport properties. However, microstructure formation in both equilibrium and non-equilibrium processing routines can be used to effectively reduce the phonon mean free path as a route to enhance the figure of merit.

This work starts with a discussion of several different deliberate microstructure varieties. Control of the morphology and finally structure size and spacing is discussed at length. Since the material example used throughout this thesis is anisotropic, a short primer on zone melting is presented as an effective route to growing homogeneous and oriented polycrystalline material. The resulting microstructure formation and control is presented specifically in the case of In_2Te_3-Bi_2Te_3 composites and the transport properties pertinent to thermoelectric materials is presented. Finally, the transport and discussion of iodine-doped Bi_2Te_3 is presented as a re-evaluation of the literature data and what is known today.

Contents

Acknowledgments **iii**

Abstract **iv**

List of Figures **x**

List of Tables **xiii**

1 Introduction **1**

1.1 Thermoelectric energy conversion 1

1.2 Thermoelectric figure of merit 2

1.3 Pertinent material 4

1.4 Summary of research 6

2 Experimental methods **8**

2.1 Introduction 8

2.2 Synthesis procedures 8

2.2.1 Indium-based bismuth telluride 8

2.2.2 Iodine-doped bismuth telluride 10

2.3 Characterization 11

2.3.1 Chemical characterization 11

2.3.2 Electron transport measurements 11

2.3.3 Thermal transport measurements 12

2.3.4 Optical characterization 12

2.4 Single parabolic band modeling 12

3 Applying quantitative microstructure control in advanced functional composites **15**

3.1 Structure Types 15

3.1.1 Grain size reduction 15

3.1.2 Grain boundary phase 16

3.1.3 Lamellar and dendritic structures 17
3.1.4 Precipitates 17
3.2 Morphology control 17
3.2.1 Solidification morphology 18
3.2.2 Eutectoid reaction morphology 21
3.2.3 Nucleation and growth precipitation morphology 22
3.2.4 Non-equilibrium processing morphology 23
3.3 Control of length scale and implications 24
3.3.1 Solidification 24
3.3.2 Eutectoid reaction 26
3.3.3 Nucleation and growth precipitation 28
3.3.4 Non-equilibrium processing 32
3.4 Microstructure characterization 33
3.5 Beyond κ_l, tuning carrier concentration 36
3.6 Conclusions 37

4 Zone melting **48**
4.1 Introduction 48
4.2 Zone melting theory 48
4.2.1 Zone leveling techniques 52
4.3 Zone melting of pertinent materials 53
4.3.1 Constitutional supercooling in zone melting 55

5 Microstructure formation and control in bismuth telluride **57**
5.1 Introduction 57
5.2 Experimental 58
5.3 Results and Discussion 60
5.3.1 Further examination of microstructure 66
5.4 Conclusion 67

6 Transport properties of indium-alloyed and indium telluride nanostructured bismuth telluride **69**
6.1 Introduction 69
6.2 Indium-alloyed bismuth telluride 69
6.2.1 Doping efficiency 69
6.2.2 Electron transport 70
6.2.3 Thermal transport 72

6.2.4 Figure of merit 74
6.3 Indium telluride structured bismuth telluride 74
6.3.1 Doping efficiency 74
6.3.2 Electron transport 74
6.3.3 Thermal transport 75
6.3.4 Figure of merit 75
6.4 Conclusion 75

7 Transport properties of iodine-doped bismuth telluride 79
7.1 Introduction 79
7.2 Orientation and doping 79
7.3 Electron transport 82
7.4 Thermal transport 83
7.5 Single parabolic band modeling 84
7.6 Figure of merit 85
7.7 Comparison to literature 86
7.8 Conclusion 89

A Derivation of concentration profiles in direct normal solidification and zone melting 90
A.1 Solute concentration profile for direct normal solidification 90
A.2 Solute concentration profile for zone melting 91

B Material evaluation for transport measurements: use of the Seebeck coefficient 93
B.1 Introduction 93

C Hot pressing and nanostructuring of $Bi_{90}Sb_{10}$ alloys to concurrently improve mechanical and thermoelectric properties 97
C.1 Introduction 97
C.2 Methods 98
C.3 Results and discussion 99
C.3.1 Silver samples 99
C.3.2 Arsenic samples 100
C.3.3 Hot pressing 101
C.3.4 Transport properties in arsenic composites 102
C.4 Conclusion 104

D Interfacial disconnections at Sb_2Te_3 precipitates in PbTe: Mechanisms of strain accommodation and phase transformation at a tetradymite/rocksalt telluride interface 106

D.1 Introduction . . . 106

D.2 Defect crystallography at rocksalt/tetradymite interfaces . . . 108

D.3 Experimental methods . . . 111

D.4 Experimental obsevations . . . 112

D.4.1 Orientation and morphology . . . 112

D.4.2 Defect analysis . . . 114

D.5 Discussion . . . 117

D.5.1 Relationship of the interfacial disconnections to the misfit strain . . . 117

D.5.2 Nucleation of new tetradymite layers . . . 120

D.6 Conclusions . . . 122

Bibliography 124

List of Figures

1.1 Schematic of a thermoelectric module . . . 2
1.2 Schematic of transport data that make up zT . . . 3
1.3 Crystal structure of tetradymite bismuth telluride . . . 5

2.1 Induction zone melting furnace schematic . . . 9

3.1 Examples of deliberate microstructure types . . . 16
3.2 Solidification morphology based on phase diagram . . . 39
3.3 Eutectoid morphology . . . 40
3.4 Nucleation and growth processing route . . . 40
3.5 3D FIB-SEM of PbTe-Sb_2Te_3 . . . 41
3.6 HRTEM image of PbTe-Sb_2Te_3 interface . . . 41
3.7 Cooling rate effects on solidification morphology . . . 41
3.8 Eutectoid reaction effects of undercooling . . . 42
3.9 Fraction transformed and ILS as a function of time . . . 42
3.10 Thermal conductivity as a function of ILS . . . 43
3.11 Supersaturation effects of nucleation and growth . . . 43
3.12 Thermal conductivity of undoped PbTe-Ag_2Te . . . 44
3.13 Slow cooling vs. isothermal annealing effects in PbTe-Sb_2Te_3 . . . 44
3.14 Undercooling effects in nucleation and growth . . . 45
3.15 PbTe-Sb_2Te_3 and Bi_2Te_3-In_2Te_3 results of nucleation and growth . . . 45
3.16 Non-equilibrium processing routes for microstructure control . . . 46
3.17 SAXS results for Mg_2Si materials . . . 46
3.18 Observed ILS vs. true ILS schematic and experimental results . . . 47
3.19 Thermal conductivity for p-type and n-type PbTe-Ag_2Te . . . 47

4.1 Bulk normal solidification vs. zone melting schematic . . . 49
4.2 Differences between $k_0 < 1$ and $k_0 > 1$ . . . 50
4.3 Differences in solute concentration profile for bulk normal solidification vs zone melting 51

4.4 Heirarchy of zone melting techniques 52
4.5 Schematics of the varied methods of solute distribution based on values of k. 53
4.6 Concentration profiles for materials grown in this thesis 54
4.7 SEM micrograph of mixing vs. un-mixing of the molten zone 55

5.1 Psueo-binary phase diagram of Bi_2Te_3-In_2Te_3 58
5.2 Initial SEM of Bi_2Te_3-In_2Te_3 composite material 59
5.3 Size and spacing histogram for Bi_2Te_3-In_2Te_3 composite material 61
5.4 EBSD results for Bi_2Te_3-In_2Te_3 composite material 63
5.5 SEM results from further examination of Bi_2Te_3-In_2Te_3 system 66
5.6 SEM showing the effects of zone leveling in the Bi_2Te_3-In_2Te_3 composite system . . . 67

6.1 Doping efficiency in indium alloyed Bi_2Te_3 70
6.2 Electron transport in indium alloyed Bi_2Te_3 71
6.3 Optical absorption in indium alloyed Bi_2Te_3 72
6.4 SPB modeling of indium alloyed Bi_2Te_3 73
6.5 Thermal transport of indium alloyed Bi_2Te_3 73
6.6 zT of indium alloyed Bi_2Te_3 74
6.7 Doping efficiency in In_2Te_3-Bi_2Te_3 composite 75
6.8 Electron transport in In_2Te_3-Bi_2Te_3 composite 76
6.9 SPB modeling of In_2Te_3-Bi_2Te_3 composite 77
6.10 Thermal transport of In_2Te_3-Bi_2Te_3 composite 77
6.11 zT of In_2Te_3-Bi_2Te_3 composite 78

7.1 XRD results showing orientation in iodine doped Bi_2Te_3 80
7.2 SEM showcasing homogeneous iodine doped material 81
7.3 Plot of $|n_H|$ vs. at. % iodine showcasing doping efficiency 81
7.4 Temperature dependent data for n_H, μ_H, ρ, and α for iodine doped Bi_2Te_3 82
7.5 Optical absorption spectra for undoped and doped Bi_2Te_3 83
7.6 κ and $\kappa_l + \kappa_{bp}$ for iodine doped samples in this work 84
7.7 Single parabolic band modeling of $|\alpha|$ and $|\mu_H|$ as a function of $|n_H|$ 85
7.8 Temperature dependent and carrier concentration dependent zT. 86
7.9 Comparison of iodine series to that of Goldsmid 87
7.10 Comparison of iodine doped samples in this work to that of Fleurial et al 88

B.1 Consistency in the values of Seebeck for Cp_1-Cp_3 94
B.2 Consistency in the values of Seebeck for Cp_4-Cp6 95
B.3 Consistency in the values of Seebeck for I_2-I_5 96

C.1 Backscattered SEM of Ag samples in Bi-Sb alloys 98
C.2 Backscattered SEM of As samples in Bi-Sb alloys 100
C.3 SEM results of hot pressing in Bi-Sb alloys 101
C.4 Room temperature resistivity data for Bi-Sb alloys 102
C.5 Room temperature Seebeck coefficient data for Bi-Sb alloys 104
C.6 Room temperature thermal conductivity data for Bi-Sb alloys 105

D.1 Crystal structures of rocksalt and tetradymite systems. 107
D.2 6/5 disconnection schematic 110
D.3 10/10 disconnection schematic 112
D.4 Tetradymite plate growth diagram 113
D.5 BF TEM image showing morphology 113
D.6 Mid range TEM image and SAD with annotation 114
D.7 HRTEM showing burgers circuit 115
D.8 HRTEM precipitate tip 115
D.9 HRTEM dislocation core positions 116
D.10 HRTEM circuit path example 117
D.11 Defect core position plot 118
D.12 Burgers vector density projections for different disconnection types 119
D.13 HRTEM outlying how to calculate Burgers circuit 121
D.14 Proposed step nucleation mechanism in PbTe-Sb_2Te_3 system 122

List of Tables

3.1 Enthalpy and entropy of fusion per g-atom, and χ values for simple metals and more complex compounds pertinent to the discussion of solidification morphology. 19
3.2 The number density, N_v, and heats of solution, ΔH_s, for Ag_2Te and Sb_2Te_3 in PbTe. 32
3.3 Major microstructural morphologies and their quantification techniques 35

5.1 Diffusion coefficients of transition metals in Bi_2Te_3 at $T = 450°C$ for $t = 72$ hr from the literature. For the cases of Ag and Au, the extremities of the expressions for $D_{\|}$ and $D_{\perp}$ were calculated, and the average of those values was taken and used in the comparison. Diffusion coefficients for the 500°C samples are larger, and therefore are not displayed here. 61
5.2 Volume fraction data for 7 at. % In Bi_2Te_3 samples at both 500°C and 450°C, as calculated by applying the lever rule to the EDS measurements and from the average thickness and spacing data $\left(X_{vol} = \frac{thickness}{spacing}\right)$. 62
5.3 Energy dispersive x-ray spectroscopy (EDS) data for samples of interest homogenized at 555°C for 96 hours, annealed at 500°C and 450°C for 72 hours (Fig. 5.2), and also the Bridgman grown crystal. All precipitates measured in the precipitated sample had a minimum thickness of ∼1 μm for accurate measurements. Likewise, matrix areas where the largest precipitate spacing occurred were utilized for the same purpose. . . 64

C.1 Short caption for BiSb table 103

D.1 Summary of defect parameters 111

Chapter 1

Introduction

1.1 Thermoelectric energy conversion

The thermoelectric effect is a solid state effect in which thermal energy is directly converted into electrical energy. The phenomenon stems from the fact that charge carriers travel in effect of a temperature gradient. Fig. 1.1 is a schematic of a thermoelectric module consisting of an n-type and p-type leg that is electrically in series and thermally in parallel. The charge carriers can be thought of as particles that diffuse from the hot side to the cold side. The result of such a configuration is commonly referred to as power generation. However, the charge carriers can be forced to move to one side of the module through an electromotive force, which causes one side to get hot, and the other side to get cold. This configuration would be considered a solid state cooling device in which the working fluid is made of electrons. Solid state heating applications have long been dominated by Joule heating, and thermoelectric heating devices are not as common.

Thermoelectrics have been successfully incorporated into applications for remote applications where power system stability is vital. One of the most well known applications is in NASA-JPL's Voyager program. Two deep space probes were sent to explore our solar system in 1977. The mission was wildly successful, as Voyager 1 and 2 uncovered significant information about our universe [1, 2]. Even more impressive is the fact that today the power systems aboard each probe have been stable enough for the last 37 years. While there isn't a hallmark success story for thermoelectric cooling, these modules are still widely used in practice due to their sensitive temperature control and lack of vibration during use.

One issue that has kept thermoelectric devices out of more significant terrestrial applications is their low efficiency. These inefficiencies arise from the difficulty in maintaining appropriate thermal transfer from source to device, but also the conversion efficiency of the materials themselves. The latter has been the area of reasearch of much of the field; however, today there seems to be a shift in focus towards the module design side of things because of economic evaluations [3] and re-evaluations of materials physics [4].

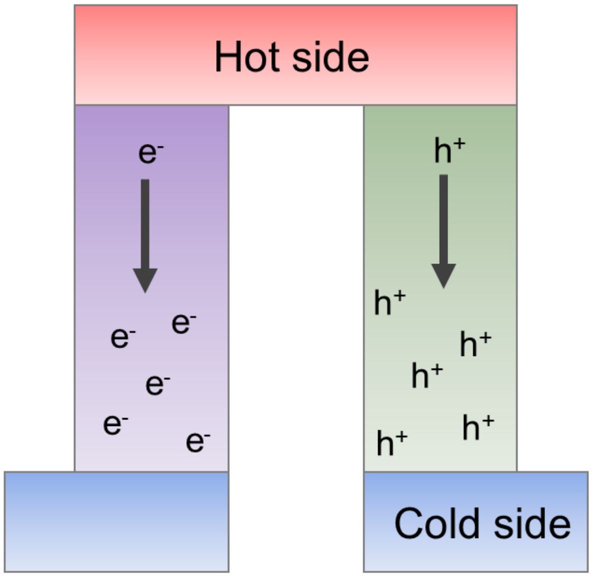

Figure 1.1: A thermoelectric module, with an n-type and p-type leg electrically in series and thermally in parallel. As shown, the charge carriers travel from the hot side to the cold side in the case of power generations.

1.2 Thermoelectric figure of merit

The efficiency on a materials level is dictated by the figure of merit, zT. The figure of merit is defined as

$$zT = \frac{\alpha^2 T}{\rho\kappa}, \tag{1.1}$$

where α is the Seebeck coefficient, ρ is the electrical resistivity ($\rho = 1/\sigma$, σ being the electrical conductivity), and κ is the thermal conductivity. The Seebeck coefficient is the potential created in the presence of a temperature gradient in a material ($\alpha = \frac{\Delta V}{\Delta T}$) and can be envisioned from an allegory to particles in a cylinder. If heat is applied to one end of the cylinder, the particles will diffuse to the cold end. Since in practice the particles are electrons, and they carry charge, the electrostatic gradient produces a potential. Since it also follows that the restriction of travel of these carriers should be low, it is a small leap to understand why a low resistivity is desired.

In order to maintain a ΔT necessary to produce enough of a potential to create a noticeable thermoelectric effect, a low thermal conductivity is required. However, the issue becomes how to fully optimize zT. The ideal case would be to maximize α while minimizing ρ and κ. However, this is difficult due to the inter relation of electron transport to each property. As can be seen in Fig. 1.2, the behavior of each of these properties does not allow for the extrema of the values to equate to the maximum zT.

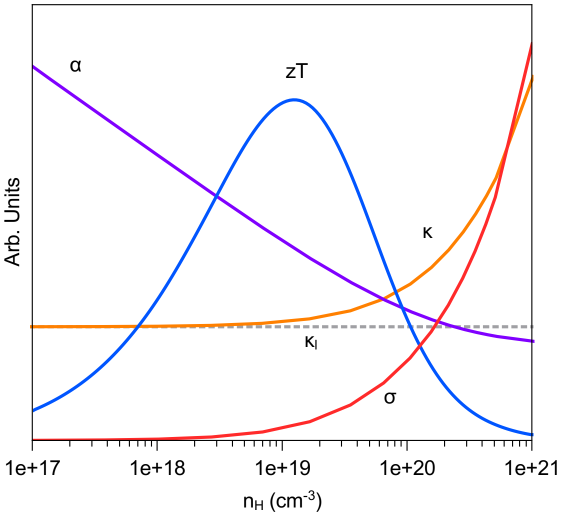

Figure 1.2: The balance between transport properties in thermoelectic materials does not allow the extrema of any property to result in the maximum zT. Therefore it is important to understand how to propertly optimize and enhance thermoelectric materials for maximum materials efficiency.

The starting point in optimization of any thermoelectric material is to establish what the inherent maximum zT is from optimizing the carrier concentration. However, further improvements are made in one of two main routes. The first is altering the band structure in some way to achieve an increase in the Seebeck coefficient without adversely affecting the electrical conductivity. Previously, electron filtering [5] and density of states distortions [6] have been proposed as such mechanisms. However, today efforts to engineer increased degeneracy of relevant conducting bands has been shown to be an effective route to enchancing the Seebeck coefficient and ultimately zT.

The other route is by decreasing the thermal conductivity, which can be thought of as two components, one being a lattice component, and the other an electronic component ($\kappa = \kappa_l + \kappa_e$). Since the electronic portion is directly proportional to the electrical conductivity by the Wiedemann-Franz law ($\kappa_e = \sigma LT$), it is deleterious to reduce this portion. The focus of thermal conductivity reduction is focused on the lattice portion. The lattice thermal conductivity in its simplest form has three components:

$$k_l = \frac{1}{3}C\nu l, \tag{1.2}$$

where C is the specific heat, ν is the phonon group velocity (often approximated as the speed of sound), and l is the phonon mean free path.

Out of these three parameters only two (ν and l) are ever engineered due to the complexity in reducing a material's specific heat. However, materials can be chosen based on their crystal chemistry, as complex unit cells are known to provide very low values of ν and ultimately κ_l. However, this is considered more in the realm of new materials discovery than it is actual thermal engineering.

The most frequently reduced quantity in κ_l is the mean free path l. It is known that the phonon and electron mean free paths are significantly different, with the phonon l being the larger of the two. Therefore, if the phonon mean free path can be significantly reduced without affecting the phonon mean free path, the potential for enhancing a material's zT is possible. This idea was proven as an effective means for thermal conductivity reduction as early as 1981 in the Si-Ge system [7]. It was shown that if the grain size was reduced to less than 5 μm, the lattice thermal conductivity was significantly reduced without adversely affecting the other transport properties. This technique has since been applied to many other material systems with varied success [8].

In additional to grain size reduction, the introduction of secondary phases has been shown to be an effective method to reduce κ_l as well [9, 10, 11, 12]. In these techniques both equilibrium and non-equiblibrium processing routes are able to achieve structures that are effective phonon scattering centers. These structures are formed in an analagous route to increasing mechanical strength, often referred to as a material's microstructure. The second phases that are formed have an array of morphologies, sizes, and number densities that are reviewed in a later chapter (Chapter 3).

1.3 Pertinent material

Bismuth telluride is a long-studied material of interest in the field of thermoelectric materials that exhibits the behavior of an efficient thermoelectric material at room temperature [13]. It is because of the room temperature efficiency that it is one of the most manufactured thermoelectric materials today.

The crystallization of bismuth telluride is rhombohedral; however, it is often convenient to view the conventional hexagonal unit cell. Fig. 1.3 is a representation of the crystal structure (space group $R\bar{3}$mH) of bismuth telluride [14]. The crystal structure is made up of three building blocks five layers thick. The block sequence is -[Te_2-Bi-Te_1-Bi-Te_2]$_0$-[Te_2-Bi-Te_1-Bi-Te_2]$_{1/3}$-[Te_2-Bi-Te_1-Bi-Te_2]$_{2/3}$, where the fraction indicates the block's translation along z in the hexagonal unit cell [15]. Along with Bi_2Te_3, Bi_2Se_3 and Sb_2Te_3 are of interest the the thermoelectric community and fall under the general category of tetradymite compounds.

The anisotropic crystal structure of Bi_2Te_3 often effects the mass, charge carrier and thermal transport as well. For instance, the coefficient of linear expansion's anisotropy is ~1.5, and the difference in resistivity can be upwards of a factor of 5 [16]. However, Bi_2Te_3 has been found to be an efficient thermoelectic material perpendicular to the z direction despite these anisotropies.

When synthesized under stoichiometric conditions, Bi_2Te_3 displays p-type conduction. However, the conductivity can be well controlled to make either p-type or n-type material. The conductivity control is typically understood as follows: Bi excess produces p-type material, while Te excess results

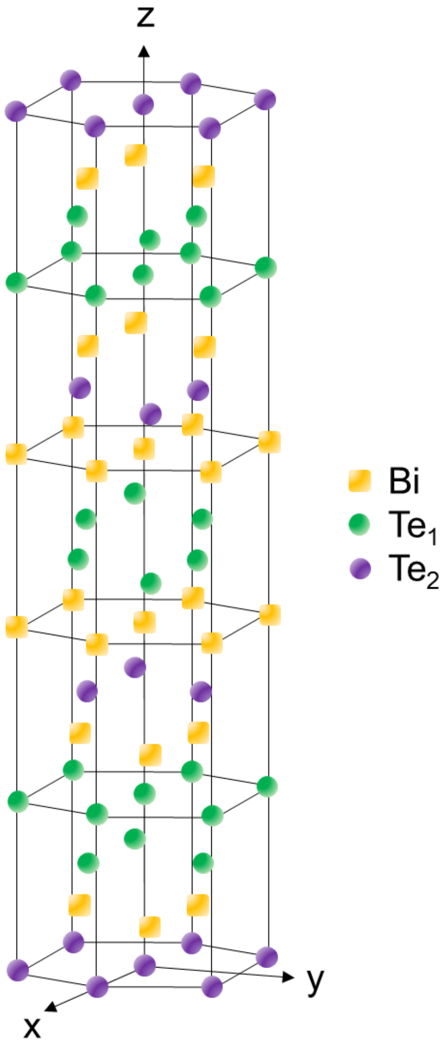

Figure 1.3: The conventional unit cell of bismuth telluride is shown. The two chalcogen sites are shown as spheres of different colors and the bismuth atoms are represented by squares.

in n-type material. The native defects controlling this are of the anti-site type, in which an ion resides in the opposing sublattice [17, 18]. For example, if a tellurium atom were to sit on a bismuth site (Te_{Bi}) it would donate an electron to conduction due to the single excess valence electron. It has also been reported that Halogens are efficient n-type dopants, and replacement of bismuth with group IV cations can control the p-type properties [13].

Most reported versions of $\mathrm{Bi_2Te_3}$ are alloyed with either antimony or selenium as well [19]. The alloying acts to reduce the thermal conductivity due to point defect scattering. However, due to the multi-band nature of both the valence and conduction bands, efforts are ongoing to understand the influence of these alloys from the perspective of the electron transport.

Due to the nature of the crystallographic anisotropy, typically synthesis routines have involved melt-based single crystal growth. The two most frequently used techniques are the Bridgman method

[20] or zone melting [21]. Bismuth telluride crystals cleave easily along the double tellurium layers, and therefore it is relatively easy to establish crystallographic directions parallel or perpendicular to z.

More recently, there has been a significant movement toward powder processing methods to create high zT tetradymite based materials [8]. The drive toward powder processing is to reduce the lattice thermal conductivity by decreasing the material grain size such that the effective phonon mean free path is reduced accordingly. However, characterizing these materials is difficult because in the consolidation process, material texturing can be erratic and difficult to control.

1.4 Summary of research

Microstructure control relevant to thermoelectric materials is introduced. The typical structures pertinent to microstructure today are presented and discussed. The control parameters applicable to morphology control are then discussed. Then an at-length discussion is held concerning the size and spacing control for the various microstructural routes. Each microstructural technique was evaluated and based on the overall increased parametric control of nucleation and growth-based precipitation; it was chosen as the best route to optimize zT through lattice thermal conductivity reduction.

Previous work had suggested that the most significant lattice thermal conductivity reduction can be obtained at temperatures below those in which the dominant scattering mechanism was umklapp scattering [10, 9]. Since bismuth telluride is widely known for its thermoelectric efficiency at room temperature, it was chosen as the candidate to explore microstructure generation.

There was limited phase diagram information regarding potential ternary systems that would be adequate candidates for microstructure formation. However, the In_2Te_3-Bi_2Te_3 system was chosen due to the simplicity of the eutectic nature relative to nucleation and growth-based precipitation. This involved requiring a system with a large enough solute solubility to form the desired second phase, but without leaving unnecessary solute dissolved in the matrix.

Microstructure formation of In_2Te_3 in Bi_2Te_3 was investigated by varying the undercooling and supersaturation of In_2Te_3 in Bi_2Te_3. In doing so, an investigation of the solvus line was conducted. It was found that the solvus line of the Bi_2Te_3 rich side had limited supersaturation control, as 7 at. % indium was necessary to force nucleation and growth-based microstructure. Any amount less than 7 at. %, and at any undercooling investigated no microstructure formation.

Zone melting was the chosen method of synthesis for two reasons. The first reason was that it had been established as an appropriate texturing method necessary in such an anisotropic system. However, the primary reason zone melting was chosen was that solute segregation is a significant problem among other crystal growth methods, but this is not the case in zone melting. There are many techniques to obtain a homogeneously distributed solute in zone melting, but as discussed later, it is extremely difficult to do this with other techniques (Chapter 4).

In order to differentiate the results of the alloyed and nanostructured material, the transport properties of each were investigated. There was a significant thermal conductivity reduction due to the presence of the In_2Te_3 precipitates; however, it was determined that the significant room temperature reduction was due to residual indium in the matrix. However, the temperature dependence of the thermal conductivity was different in the two samples, with a lower thermal conductivity in the composite material (Chapter 6). Ultimately it was determined that In_2Te_3 was not a good candidate for thermal conductivity reduction because the decrease in the band gap decreased the critical temperature for bi-polar conduction, and significantly reduced the maximum zT.

However, with the ability to synthesize and characterize Bi_2Te_3 led to an investigation of the properties of extrinsically doped bismuth telluride. In this case iodine was chosen based on Hume-Rothery rules as a substitute for tellurium. It was determined that iodine is an efficient n-type dopant in Bi_2Te_3, and the maximum zT achieved matched well with other iodine doped data [13, 22, 23]. However, when comparing the material to what is considered the standard reference data [19], there is a significant departure. The doping scheme is different in the two works, with this work utilizing iodine as the n-type dopant, but in the standard work the transport properties being controlled by excess tellurium doping. However, it is expected that due to the difference in Seebeck metrology in the two works that the reference data has overestimated values for the Seebeck coefficient.

Chapter 2

Experimental methods

2.1 Introduction

Single crystal bismuth telluride has historically been made via bulk directional solidification of the normal type [13, 22, 23]. The technique often implemented is that of the Bridgman method [20] and resulting data are often reported either parallel or perpendicular to the basal plane. Other methods of bulk single crystal growth, such as the Czochralski method, are often not used due to the high vapor pressure and toxicity of chalcogenides. Zone melting, sometimes referred to as the traveling heater method, can also be implemented in order to obtain either single crystals [19] or oriented polycrystalline data [13, 22, 23]. More recently, a push has been made in the realm of powder metallurgy synthesis to invoke κ_l reduction [8]; however, this method is often difficult to fully characterize and was not used in this thesis.

2.2 Synthesis procedures

2.2.1 Indium-based bismuth telluride

Samples that were prepared for microstructure evaluation were synthesized by melting and annealing [24]. Initial elements of Bi, In, and Te with 99.999 % purity (metals basis) were weighed out and placed in quartz ampoules. The ampoules were then sealed under vacuum at a pressure of $\sim 10^{-5}$ Torr. Samples were melted at 800-900°C, homogenized at 555°C, and then finally precipitate formation was generated between 400-500°C in a vertical tube furnace.

Once the necessary information was understood about microstructure formation, zone melting was implemented to orient the material for the necessary transport measurements. Quartz ampoules with inner and outer diameters of 6 × 10 mm were utilized to minimize material used, as the ingot length was typically ~90 mm in length. Because the distribution coefficients for the 4 at. % and 7 at. % indium samples were close to 0.5 (0.67 and 0.64 respectively), it was necessary to employ the starting charge zone leveling method, whereby the first zone had the composition of the liquidus at the point in which the solidus was 4 and 7 at. % indium, while the rest of the ingot had the composition corresponding to the solidus.

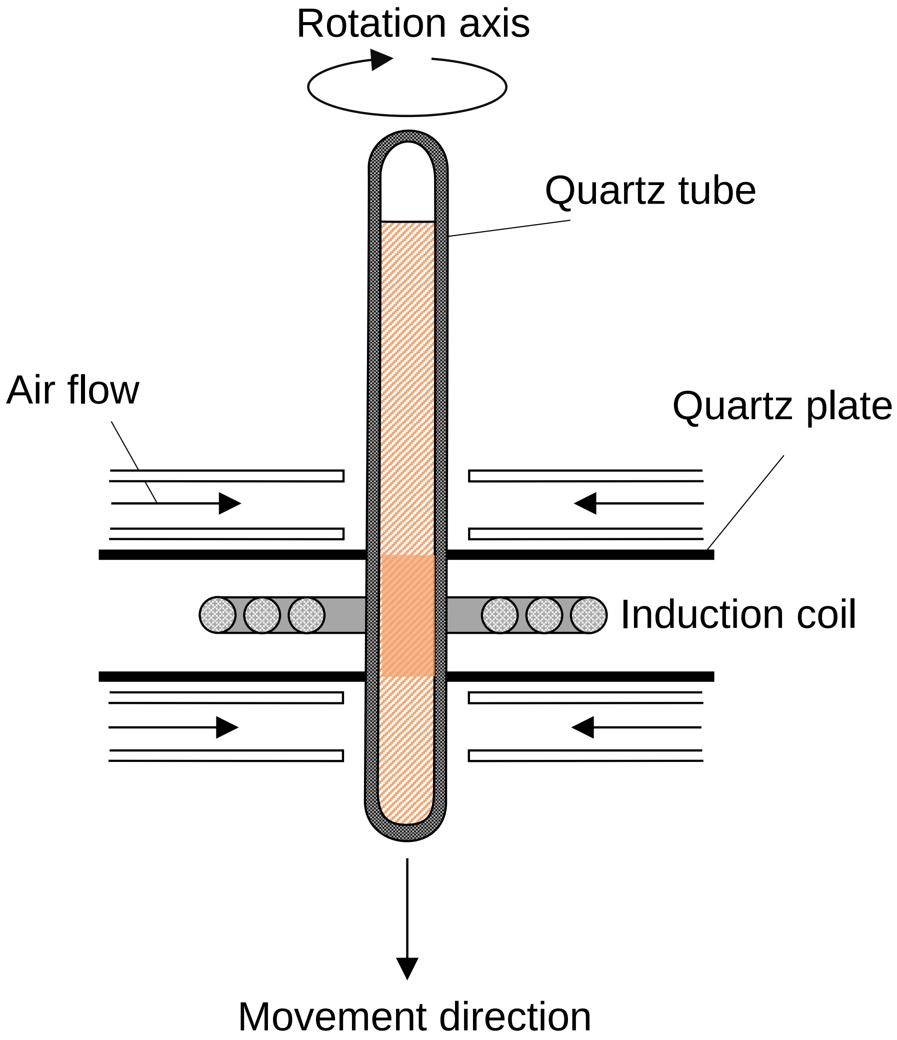

Figure 2.1: A schematic representation of the necessary aspects of the home-built zone melting furnace used to synthesize the materials pertinent to this thesis.

The zone melting for all indium based samples was conducted on a home-built vertical zone melting furnace. The furnace was designed such that evacuated quartz ampoules can be placed directly into the furnace, constantly rotated and with vertical motion control, such that the growth rate can be readily controlled from 0.01 - 30 mm/hr. The temperature is measured using a pyrometer

(Modline 5, IRcon Corp.), whereby the temperature is sent to a temperature controller (Yokogawaka UP550), which then communicates with the induction heating system (Ambrell HOT SHOT) to ultimately control the final sample temperature.

Fig. 4.1 is a schematic of the furnace in the immediate vicinity of the molten zone. As can be seen, a quartz tube is constantly rotated about its long axis with compressed air flowing above and below the molten zone. Quartz plates above and below the molten zone act as barriers between the molten zone and the solid material to maintain the zone length.

The growth rate that produced homogeneous and oriented material was determined to be a maximum of 3 mm/hr. Anything over this rate, and there was segregation of indium in the form of In_2Te_3 (Fig. Phase Diagram). The initial zone leveling of both the 4 at. % and 7 at. % samples revealed that they were homogeneous materials that did not necessitate any additional annealing (Fig. Phase Diagram). Therefore, after zone leveling, samples of minimum 14 mm length were cut on a diamond saw and then placed into similarly evacuated quartz ampoules, and annealed at the necessary temperatures to facilitate nucleation and growth. In this thesis the transport results presented are for a sample annealed at 450°C.

Once annealing was complete, the samples were further cut and polished to carry out transport measurements. For Hall effect and resistivity measurements a parallelpiped with dimensions of approximately $1.5 \times 4 \times 12$ mm^3 was used. Seebeck and thermal conductivity measurement samples were disk-shaped with diameters between 6-12 mm and approximately 1 mm thick.

2.2.2 Iodine-doped bismuth telluride

For all samples of Bi_2Te_3 that were doped with iodine, the binary compound BiI_3 (99.999 % purity, metals basis) was used as the constituent compound to dope the material. A large quantity (typically 100g) of undoped stoichiometric Bi_2Te_3 was synthesized concurrently with a smaller amount of iodine-doped Bi_2Te_3. The smaller, heavily doped material had a nominal iodine content of 1 at. %. Stoichiometric quantities of the un-doped and doped material was weighed out and placed in carbon-coated quartz ampoules, melted at 900°C for a minimum of 12 hours, ground into powder and then loaded into an ampoule for zone melting.

The blending of the un-doped and 1 at. % iodine-doped material was done to decrease the sensitivity in iodine content to better control the carrier concentration. This is necessary due to the difficulty in utilizing BiI_3, as it is a very hygroscopic substance, even in controlled environments. Hall effect measurements were conducted on the lowest and highest doped samples to establish the range of carrier concentrations and verify successful doping.

The zone melting parameters necessary for iodine-doped Bi_2Te_3 are quite forgivable compared to indium alloyed samples. Because iodine solute content is quite low (nominally 0.04-0.2 at.%) the distribution coefficients do not vary much from ~ 1. This means that the number of zones necessary to achieve homogeneous material should be expected to be within the first zone, which is what is found in practice (Appendix B).

2.3 Characterization

2.3.1 Chemical characterization

The phase purity and chemical composition determination of the samples was primarily done using scanning electron microscopy (SEM) coupled with energy dispersive x-ray spectroscopy (EDS), electron back-scattered diffraction (EBSD), and electron microprobe analysis (EPMA), which utilizes wavelength dispersive spectroscopy (WDS). SEM, EDS, and EBSD analyses were performed using a Zeiss 1550 VP SEM. To quantify the iodine content in the doped Bi_2Te_3 samples, EPMA was conducted under the assistance of Chi Ma using a JEOL JXA 8200 system. The standards used were elemental Bi, Se, and Te while RbI_3 was used for the iodine standard.

X-ray diffraction measurements on parallelpiped samples were performed on a Philips PANalytical X'Pert Pro with CuKα radiation (λ_1 = 1.540590 Å, λ_2 = 1.544310 Å), using a step size of 0.008 ° 2θ. The resulting diffraction data were refined using the Rietveld method [25] with the FullProf program, starting with the atomic coordinates determined by Feutelais et al. [14]. All reflections can be indexed to the space group $R\bar{3}$mH, and no secondary reflections are observed.

Rietveld refinements of the discs exhibit a large discrepancy between the observed and calculated intensities, most likely due to the orientation in the ingot grown via zone-melting. Using a modified March's function to accommodate for preferred orientation along the (00n) Miller indices leads to a much better fit of the intensities and corroborates the preferred orientation in these samples.

The results indicate a plate-like habit of the grains, with about 90% of the grains' preferred orientation axis perpendicular to the surface of the parallelpiped. The preferred orientation axis coincides with the reciprocal lattice vector d_{001} and leads to an increase in the observed intensities. Moreover, this indicates that 90% of the grains exhibit their (001) hkl planes parallel to the surface of the flat sample. This can be seen in the better fit for the (006) reflection in Fig. 7.1.

2.3.2 Electron transport measurements

The resistivity and Hall effect measurements were done on a modified MMR technologies variable temperature hall measurement system (VTHS) with a 1.0 T field up to 250°C. Measurements were done under dynamic vacuum, and, due to anisotropic effects in Bi_2Te_3, the 4-point method was used to measure resistivity. An additional contact was placed opposite to one of the resistance voltage contacts in order to obtain Hall data without needing to change the contact geometry. From the Hall coefficient, the Hall carrier concentration was calculated from $R_H = -1/en_H$. The Hall mobility was determined from the measured resistivity and carrier concentration using $\mu_H = 1/n_H e \rho$.

The Seebeck coefficient was measured under dynamic vacuum in a home-built system [26]. The measurement forces a temperature gradient across the sample to oscillate between ±7.5 K, while a constant average temperature is maintained at each point. The thermocouples used were made of niobium-chromel, and resistive cartridge heaters maintained the temperature inside a BN cylinder. The system employs a 4-point in-line method that allows for the temperature and voltage to be measured at the same point on the sample. Prior to measurement, the samples are sandwiched between pieces of graphite foil, which helps maintain even heating on the surface of the sample.

2.3.3 Thermal transport measurements

Measurements of the thermal diffusivity were done using a Netsch LFA 457. The thermal conductivity was then calculated based on $\kappa = DC_p d$, where D is the thermal diffusivity, C_p is the heat capacity, and d is the density. The heat capacity was estimated using the Dulong Petit value, and even though the Debye temperature of Bi_2Te_3 is fairly high (155 K [27]), this is an accepted approach for Bi_2Te_3. The measurements were performed in an inert argon atmosphere, under a constant flow rate of 50-100 mL/min.

2.3.4 Optical characterization

Diffuse reflectance measurements were performed with the assistance of Zachary Gibbs to characterize the optical band gap in Bi_2Te_3 alloyed with indium and selenium, and the effects of iodine doping. The measurements were performed at room temperature using diffuse reflectance infrared Fourier transform spectroscopy (DRIFTS), using a Nicolet 6700 FTIR spectrophotometer (Thermo Scientific) with the attached Praying Mantis Diffuse Reflection accessory (Harrick), deuterated triglycine sulfate (DTGS) detector and KBr beamsplitter. The samples were all referenced to the provided alignment mirror, which gave the same results as when referenced to KBr powder without the additional impurity features of KBr. The absorption coefficient was obtained using the Kubelka Munk analysis $F(R) = \frac{\alpha}{K} = \frac{(1-R)^2}{2R}$ [28], where R is the fractional reflectance, α is the absorption coefficient and K is the scattering coefficient. In cases in which the particle size is greater than the wavelengths measured (20-2 μm), it is acceptable to assume the scattering coefficient to be independent of frequency.

2.4 Single parabolic band modeling

To analyze the resulting electronic and thermal transport properties, the single parabolic band model was used. In this model, solutions to the Boltzmann transport equation within the relaxation time approximation were used, assuming the only contribution to conduction is from a single relatively isotropic portion of the band structure. The energy dispersion is approximated as $E(k) \propto \frac{\hbar^2 k^2}{2m*}$. This means that the model will break down for systems with multi-band effects, more than one majority carrier, and band non-parabolicity. But even in cases in which the model does not accurately predict the transport it is a good starting point to understand the material in question. For an in-depth analysis and step-by-step approach to developing a single parabolic band model for transport analysis the readers are recommended to consult reference [19].

In the single parabolic band model, the Seebeck coefficient data is used to estimate the reduced chemical potential (η) and Hall coefficient (R_H), in order to estimate the effective mass (m^*). In Eqn. 2.1 λ is a constant determined by the pertinent scattering mechanism, and in the case of acoustic phonon scattering the value is $\lambda = 0$. Eqn. 2.3 is the Fermi integral with ζ as the reduced carrier energy.

Using the experimental data for the Seebeck coefficient and Eqn. 2.1, one can determine the reduced chemical potential, η. If data for n is available, then Eqn. 2.2 can be used to estimate m^*. Then, assuming rigid band behavior, values for α as a function of n can be calculated and plotted. This plot is often referred to as a Pisarenko plot:

$$\alpha = \frac{k}{e}\left(\frac{(2+\lambda)F_{1+\lambda}(\eta)}{(1+\lambda)F_{\lambda}(\eta)} - \eta\right) \tag{2.1}$$

$$n = 4\pi\left(\frac{2m^* kT}{h^2}\right)^{3/2} F_{1/2}(\eta) \tag{2.2}$$

$$F_j(\eta) = \int_0^\infty \frac{\zeta^j d\zeta}{1+\exp^{\zeta-\eta}}. \tag{2.3}$$

The carrier mobility can be calculated using the resulting values for η as well. Eqn. 2.4 is a function of η, and the intrinsic mobility μ_0 is used as a fitting parameter used when solving for μ_H:

$$\mu_H = \mu_0\left(\frac{\pi^{1/2}F_{\lambda}(\eta)}{F_{1/2}(\eta)}\right). \tag{2.4}$$

The Lorenz number L can be calculated, as it is also a function of η (Eqn. 2.5). Once calculated, the electronic thermal conductivity can be calculated using the Wiedemann-Franz law ($\kappa_e = \sigma LT = LT/\rho$). This value can be subtracted from the total thermal conductivity to estimate the lattice thermal conductivity κ_l:

$$L = \frac{k^2}{e^2}\left(\frac{3F_0(\eta)F_2(\eta) - 2F_1(\eta)^2}{F_0(\eta)^2}\right). \tag{2.5}$$

Finally, an estimation of zT can be made as a function of n. Using Eqn. 2.1-2.5 and assuming a constant κ_l the figure of merit can be calculated. Note that data from only a single sample is necessary to determine the approximate value of the figure of merit, as this technique can be used to determine the efficiency of a material system, without requiring the synthesis of multiple samples.

Chapter 3

Applying quantitative microstructure control in advanced functional composites

Reproduced with permission from *Advanced functional materials* **24**, 2135-2153 (2014). Copyright ©Wiley-VCH.

3.1 Structure Types

A practical starting point for understanding microstructural evolution is in identifying the type of structure formed in one of the many available processing routes. There are many structure types where direct observation is often enough to identify, while others are difficult to differentiate and requires additional information. Often the origins of these difficult to differentiate structures are resolved by understanding the driving force behind the phase separation. This is typically done by determining the phase diagram of the material in question through experiments and calculations. The following descriptions are not intended to be a comprehensive list of structure types, rather the intent is to introduce the types of structures often encountered in the course of tuning thermal conductivity.

3.1.1 Grain size reduction

One avenue avidly pursued to reduce the lattice thermal conductivity is to minimize the grain size via mechanical alloying/milling (Fig. 3.1a) and rapid consolidation techniques. In these works, powders are created by ball milling ingots of pre-melted materials (mechanical milling) or the pure elements (mechanical alloying). In both cases, the grain size is reduced to tens of nanometers and is maintained at that size by using rapid consolidation. The composite aspect of these materials usually lies in slight compositional differences, which manifest themselves in the form of component

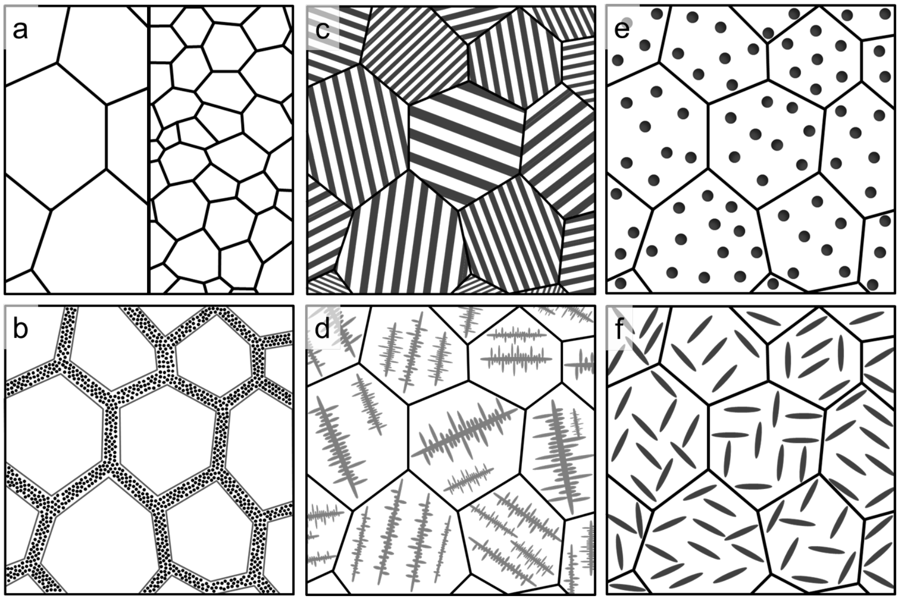

Figure 3.1: Examples of different types of deliberate microstructure in thermoelectric applications. (a) Grain size reduction, (b) grain boundary phases, (c) lamellar structures, (d) dendrite formation, and (e-f) precipitation based microstructure are all promising routes to reducing thermal conductivity.

rich ingrain nanoparticles [8]. There is also evidence to suggest that small impurities at the grain boundaries exist in these types of materials [29] that could inhibit grain growth.

The first system in which thermal conductivity dependence on grain size was studied was in alloys of Si-Ge.[7] It was found that a grain size of 5 μm or less resulted in a 28% decrease in thermal conductivity compared to the single crystal value. Since then, work has been done in Bi_2Te_3/Sb_2Te_3, PbTe, Skutterudites and further enhancements in Si-Ge have been achieved in this fashion [8].

3.1.2 Grain boundary phase

Controlling grain boundary phases is a fairly new and relatively unexplored route to creating functional thermoelectric composites. The current state of the art uses coated powders and hot pressing consolidation to achieve these structures (Fig. 3.1b) [30]. There have been several thermoelectric systems that have been explored in this fashion such as PbSnSe coatings on PbSnTe and also $CoSb_3$ coatings on $LaCoFe_3Sb_{12}$ [31, 32]. Initial studies on alkali-metal coated $(Bi,Sb)_2Te_3$ materials have shown improvements in zT due to a reduction in κ_l as well [33]. However, more work is necessary to understand the structure controlling and carrier scattering mechanisms in these materials because there is evidence of thermal conductivity reduction even in systems with an incomplete grain boundary phase present [34].

3.1.3 Lamellar and dendritic structures

Lamellae are finely spaced (nm-μm) structures that alternate in composition as shown in Fig. 3.1c. They resemble superlattice structures often generated through thin film techniques, with the added advantage of being self-assembled. Lamellar structures can be either completely aligned in a given domain (as in Fig. 3.1c) or can have more of a disordered pattern. The most prevalent material studied with such a structure is pearlite steel [35], but this type of structure has formed in the PbTe-Sb_2Te_3 system of materials as well [36, 37, 38, 39]. This type of microstructure can be generated in the bulk by solidification and eutectic reactions or through solid state techniques such as eutectoid reactions.

Dendrite structures can also be generated by solidification methods and have a tree-like branched form (Fig. 3.1d). In geology, dendritic formation can occur in the large scale crystal habit, as is the case for native copper. However, in materials design dendrites are more typically thought of as a result of an internal phase separation. Analogous to lamellae, dendritic microstructure has been found in the PbTe-Sb_2Te_3 system, however unlike the lamellae, dendrites are typically formed by solidification from the liquid [39, 37].

3.1.4 Precipitates

Nucleation and growth techniques are often used to grow precipitates within grains with varying morphology (Fig. 3.1e-f). Typically the decreasing solubility with decreasing temperature of eutectic, or eutectic-like, phase diagrams is the procedure for growing structures of this type. Systems with high solute solubility (>3 at. %) are often desired as this can correlate to a higher number density of precipitates. A high second phase solubility also indicates that the volume fraction will be large enough to have a significant impact on κ_l. Ideally, simple eutectic, or eutectic-like phase diagrams present approachable ways to exploit the decreasing solubility with decreasing temperature along the solvus line to precipitate out the desired second phase. This often allows for fine structure on account of the temperature control in the two phase region, and also the slow diffusion in the solid state. There has been extensive work done with this technique in age hardening of metals [40], but recently this technique has proven beneficial in the PbTe system in conjunction with Ag_2Te, Sb_2Te_3, and also $PbBi_2Te_4$ [9, 10, 12, 11, 41].

3.2 Morphology control

For each previously mentioned structure type there are different ways to vary the resulting microstructure's morphology. From a seemingly simple binary phase diagram, one can achieve several different structure types by varying the chemical composition, solidification rate, or processing route.

Typically, areas around invariant points associated with solidification reactions, such as eutectic or peritectic points, act as morphology transition indicators for different microstructure types.

3.2.1 Solidification morphology

The point on a phase diagram in which a single phase liquid directly solidifies into solid phases, forgoing any solid-liquid equilibrium region, is referred to as the eutectic point. In discussing binary, or in many thermoelectric cases pseudo-binary, eutectic solidification the microstructural morphology is most easily understood using the ideas of Hunt and Jackson [42]. Early atomistic treatments of solid-liquid interface growth by Jackson considered the free energy change during the atom exchange for an exposed crystal face in contact with its liquid during melting or freezing [43, 44]. It was determined that the material's entropy of fusion, ΔS_f, also known as the entropy of melting, can be used to predict morphology type. The entropy of fusion,

$$\Delta S_f = \frac{\Delta H_f}{T_m}, \tag{3.1}$$

where ΔH_f and T_m are the enthalpy of fusion and the melting point, is the change in entropy upon melting of a pure substance. Under this formalism [44], the entropy increases as the configurational possibilities increase as melting occurs, thus the value is positive.

The entropy of fusion is made dimensionless when divided by the universal gas constant ($\chi = \frac{\Delta S_f}{R}$) and when the free energy change associated with the atom exchange during growth is minimized, there are two distinct mechanisms based on χ. For values of $\chi < 2$ the free energy is minimized resulting in a rough crystal interface indicative of no preferential crystal ordering, and for $\chi > 2$ the minimization dictates a smooth interface, representative of a preferred crystal orientation during growth [43].

It should be specified that the following criteria pertain to solidification at or near the eutectic point, which will be referred to as eutectic solidification. Eutectic compounds can be placed into three discernible categories based on χ [42]. The first is where the entropies of fusion of the two substances are similarly low ($\chi < 2$), the next is where they are completely dissimilar ($\chi < 2$ in one, $\chi > 2$ the other), and the third is where both are similarly high ($\chi > 2$).

In the case of the constituent compounds having low ΔS_f values, the morphology is most often lamellar or rod-like. Examples of this type of behavior exist in such systems as Pb-Sn, Pb-Cd or Sn-Cd [42] where each compound has a similar enthalpy of fusion and melting point (Table 3.1).

There is a more varied morphology, however, when one phase has a lower ΔS_f than the other. The structures in this scenario often have a complex and or irregular shape. Classic cases of such morphologies can be seen in the Pb-Bi or Sn-Bi systems [42] as the low melting point and large enthalpy of fusion give Bi a significantly larger χ than either Sn or Pb (Table 3.1).

In the case of similarly large ΔS_f values, both phases grow with smooth solid-liquid interfaces under a normal nucleation process, which often results in large flat crystal faces. On account of semi-metals or semi-conducting materials often having high entropies of fusion, this type of microstructure is observed in the solidification of such materials.

The atomistic view in the previous discussion works well for simple systems such as metals, however when more complex compounds are considered the total molar content can be misleading with regard to ΔS_f. To extend the predictive guidelines of the entropy of fusion for more complex material systems, it is necessary to convert the units from a per mole basis to one that is per moles of atoms. Also known as the gram-atom (g-atom), this is done simply by dividing the enthalpy of fusion by the number of moles of constituent atoms in one mole of the compound. This conversion takes into account the fact that enthalpy and entropy are extensive properties, and it puts the comparison of simple metals and more complex systems on an even keel by effectively normalizing them by the total number of moles of atoms in one mole of the compound. Therefore, as seen in Table 3.1 the values of ΔS_f for the elemental metals and semi-metals is the same, however for the binary and ternary compounds is decreased by the number of moles of atoms.

In some cases however this conversion is not sufficient to explain the resulting morphology. In the case of the eutectic solidification of TiO_2-$SrTiO_3$ the resulting structures upon solidification have been proven to be faceted, resembling that of split ring resonators [45]. However, as can be seen in Table 3.1 after the g-atom conversion, the values for TiO_2 and two other titanates comparable to $SrTiO_3$ all have values of χ below the transition value for faceted structures. However, upon melting these highly ionic materials the resulting liquid is not completely disordered. Therefore, there is an additional consideration to make for molecular liquids, as there is a significant ordering required upon freezing.

Table 3.1: Enthalpy and entropy of fusion per g-atom, and χ values for simple metals and more complex compounds pertinent to the discussion of solidification morphology.

Compound	T_m (K)	ΔH_f (kJ/g-atom)	ΔS_f (kJ/g-atom K)	χ	Ref.
Pb	600.6	4.77	7.95	0.96	[46]
Sn	505.1	7.15	14.15	1.70	[46]
Cd	594.2	6.21	10.45	1.26	[46]
Bi	544.6	11.11	20.39	2.45	[46]
Si	1687.2	50.21	29.76	3.58	[46]
Ge	1211.4	36.94	30.49	3.67	[46]
Sb_2Te_3	891.2	19.8	22.2	2.67	[47]
PbTe	1197.2	20.7	17.3	2.08	[48]
TiO_2	2143	22.32	10.41	1.25	[49]
$CaTiO_3$	2233	21.3	9.6	1.15	[50]
$BaTiO_3$	1898	15.9	8.4	1.01	[51]

While ΔS_f is a good indicator for whether the growth interface will be diffuse or smooth, resulting in lamellar/rod-like or faceted structures, it does not always predict the resulting solidification morphology. When the solidification occurs at a composition that is far from the eutectic composition, the effects of undercooling play an important role in the solidification morphology. Currently, the impact of undercooling on eutectic solidification has been explored on a preliminary basis, and it has been established that there exists a critical undercooling where the morphology differs from the type predicted by ΔS_f [52]. There is continued work in understanding the mechanism in which this change occurs [53].

However, many applications either allow or require that solidification take place far from the eutectic composition, and the mechanism for freezing of this variety is known as single phase solidification. That is, there is one primary solidifying phase, unlike eutectic solidification in which there are at least two. In the solidification of a eutectic system far from the eutectic composition, the solid phase rejects solute at the solidification front, thereby increasing the solute content in the liquid and decreasing the liquid temperature in the vicinity of the solid-liquid interface. Therefore, the temperature of the liquid at the interface will be lower than the liquidus temperature of the bulk liquid and this effect is known as constitutional undercooling.

This concentration gradient based undercooling can lead to variations in the resulting morphology in single phase solidification. The source of the variation stems from the solid-liquid interface stability. Tiller and Chalmers determined that for a binary single phase solidifying system, in the absence of convection, there is a critical condition in which constitutional undercooling occurs [54],

$$\frac{\nabla T}{\nu} \leq \frac{mC_0}{D}\left(\frac{1-k}{k}\right), \tag{3.2}$$

where ∇T is the temperature gradient in the liquid at the interface, ν is the solidification velocity, m is the slope of the liquidus, C_0 is the equilibrium concentration, D is the diffusion coefficient and k is the distribution coefficient. For values of $\frac{\nabla T}{\nu}$ that do not satisfy this condition, it is predicted that the solidification will result in no microstructure formation. However, for values of $\frac{\nabla T}{\nu}$ that satisfy this condition there will be some form of microstructure generation. Moreover, if the value of $\frac{\nabla T}{\nu}$ is near the critical condition the likely morphology will be that of a lamellar or rod like structure, often referred to as a cellular structure. When the departure from this critical value is large, the morphology is typically dendritic. It should be noted that ΔS_f is still an important parameter in single phase solidification. In that, if faceted structures are predicted, and the value of $\frac{\nabla T}{\nu}$ is sufficiently small, the resulting microstructure will still be atomically smooth, but can produce faceted dendrites [55] or spiraled hopper crystals [56].

Taking this into account, the solidification morphology of single phase solidification has been explored in the more complex PbTe-Sb_2Te_3 system [37, 39]. After the g-atom conversion this material system behaves as one would with dissimilar values of χ. As can be seen in Fig. 3.2, when rich in the lower ΔS_f-PbTe phase, the resulting microstructure is dendritic, while when rich in the higher entropy Sb_2Te_3 phase the microstructure is of a layered and faceted variety. This happens in lieu of the fact that in both materials χ is greater than the transition value. However, because the value for PbTe is very near this transition point it is not unreasonable to find a non-faceted microstructure.

The degree of structure alignment can be controlled in solidification based microstructure formation as well. The formation of eutectic microstructure occurs at the solid-liquid interface, and directional solidification results in an aligned microstructure. In this process the entirety of the material is melted and one end is brought into a zone of decreased temperature initiating solidification. This proceeds until the solid-liquid interface reaches the other end of the sample, solidifying completely. Successful lamellar alignment has been accomplished in the Ag-Pb-Te and Ag-Sb-Pb-Te ternary systems utilizing this method [57, 58]. All of the same morphological control parameters are employed (ΔS_f and $\frac{\nabla T}{\nu}$) in this type of experiment, however, because the solidification is directional, the interface control is substantial, allowing one to tailor the alignment of the resulting microstructure. Often, the scenario of low ΔS_f values involving lamellar or rod-like morphology have the most significant alignment due to the simplicity of growth compared to that of irregular or faceted structures.

3.2.2 Eutectoid reaction morphology

While eutectic solidification involves a single liquid transforming into two (or more) solids upon cooling, a eutectoid reaction is similar and produces similar microstructure. The difference being that the latter reaction pathway involves a single solid dissociating into distinct solid phases. There is a similar type of microstructure formed by a reaction known as spinodal decomposition [59]. It is often, however, difficult to differentiate between lamellar eutectic/eutectoid structures and those formed by spinodal decomposition. The difference lies within the formation pathways, the former involving growth via nucleation [60] and the latter occurring uniformly throughout [59]. Distinguishing between the two reactions directly would involve the impractical in-situ observation of the microstructural evolution. More practically, understanding the phase diagram would reveal the nature of the microstructure's origin. An example of a thermoelectric spinodal is that of the PbTe-GeTe system [61], and while this type of microstructure has been shown to be effective in tuning thermal conductivity it does not fall under the scope of this work.

There is a rich history of directional solidification experiments examining the alignment and morphology of the resulting microstructure [42], but this is not the case with regard to eutectoid reactions [62, 63, 64, 65]. However, it is possible to extend the results of the directional eutectic solidification literature to better understand eutectoid reactions with the added exception of understanding the role of interfacial strain energy. Because the material remains in the solid state throughout a eutectoid reaction, the interfacial interactions are non-negligible [66], complicating eutectoid reactions due to transformation strain at the solid-solid interfaces.

The results of eutectoid directional cooling experiments can be seen in Fig. 3.3, where the metastable $Pb_2Sb_6Te_{11}$ phase reacts to form lamellae of PbTe and Sb_2Te_3. A more isotropic morphology is possible when the material is annealed at a temperature below the eutectoid point, which can be seen in Fig. 3.3. Therefore, the anisotropy of the resulting structures can be controlled via the reaction interface through directional cooling (isotropic structures), or bulk isothermal annealing (anisotropic structures) depending on which type is desired.

3.2.3 Nucleation and growth precipitation morphology

The generation of microstructure based on nucleation and growth of precipitates is described best by the labeled eutectic phase diagram of Fig. 3.4. In accordance to this type of phase diagram, a typical synthesis route to precipitate a secondary β phase in a matrix of α would be to first melt the constituent elements, then homogenize the material in the solid solution region and finally precipitate the desired microstructure.

The initial morphology of precipitates formed during nucleation and growth is best understood based on the dependence of free energy. Nucleation occurs when the overall change in free energy is lowered causing ΔG to be a negative value. To first order, ΔG is represented by

$$\Delta G = -V\Delta G_V + A\gamma, \tag{3.3}$$

where V is the nuclei volume, ΔG_V is the volumetric free energy, A is the nuclei surface area, and γ is the surface free energy. For the stable nuclei initially formed, the morphology will be spheroidal to balance the dominance of the surface free energy to that of the volumetric free energy (Eqn. 3.3 and Fig. 3.5). As the precipitates grow, however, the optimization of the volumetric and interfacial free energies can lead to a myriad of morphologies as the dominant shape of the resulting precipitates is not necessarily an equilibrium shape. Often, the resulting stable structures are the ones that nucleate the fastest [67]. This occurs due to the strong dependence of γ on the nucleation rate, which does not necessitate an equilibrium shape as it could very well be a less stable structure that dominates the growth process.

There are also interfacial elastic energies, based on the elastic constants, that can play a role in governing the morphology of precipitates in this regime [66]. As has been seen in the PbTe-Sb_2Te_3 system, a weak interfacial compatibility condition led to precipitates forming a ribbon like shape as opposed to the disk or lenticular shape previously expected (Fig. 3.5) [68].

However, other simple guidelines for precipitation based morphology lie in the comparison of crystal structures and lattice constants of the materials in question. For example, in the Bi-Sb system both elements share the same crystal structure and have very similar lattice parameters, so based on the Hume-Rothery rules it is not unexpected for them to form a complete solid solution and ultimately little, if any, microstructure [69]. However, Bi and As also share the same crystal structure yet the lattice mismatch is large enough that there is very little solubility [70], indicating the possibilities of significant nucleation based microstructure formation.

However, many examples of nucleation and growth based microstructure in thermoelectric materials is one of differing crystal structures. The differing morphological results are often dictated by which material is the host phase, and which is the secondary phase. In both the PbTe-Sb_2Te_3 and $AgSbTe_2$-Sb_2Te_3 systems the host phase is a rock-salt structured crystal with an embedded tetradymite secondary phase [71, 72], each with the classic FCC-HCP $\{111\}\|\{0001\}$orientation relationship. The primary difference however, is in the dislocation spacing along the interface in each system. Due to the large mismatch (6.7 %) in the PbTe-Sb_2Te_3 system [71], there are a significant number of interfacial dislocations along the interface (arrows, Fig. 3.6). However, the lattice mismatch in $AgSbTe_2$-Sb_2Te_3 is an order of magnitude smaller (0.8 %) [72] and has an appreciably lower interfacial dislocation content, so much so that it is difficult to directly image.

Some systems' combination of crystal structure and lattice mismatch even allow for coherent precipitation to occur, as all previous cases were reported to be semi-coherent. In the case of PbTe-Ag_2Te, it has been reported that the cubic-monoclinic arrangement of $\{001\}\|\{201\}$ and a low lattice mismatch of 1.8 % permits complete coherency in some precipitates [73]. The morphological evolution in this system is slightly complicated as the nucleation and growth temperatures involve cubic phases for both PbTe and Ag_2Te, while upon cooling the Ag_2Te phase transforms into the monoclinic phase.

In all of the previously mentioned cases, the host or matrix phase has been a cubic structure and since there are often several similar crystallographic orientations, four in the $\{111\}\|\{0001\}$ case (top row, Fig. 3.15) and three in the $\{001\}\|\{201\}$ case, there is often a distribution of structure orientations. However, the Bi_2Te_3-In_2Te_3 system, while having a $\{111\}\|\{0001\}$ orientation, is limited to the precipitation in the basal planes as the matrix phase is the HCP crystal. Therefore, the resulting microstructure is aligned with all precipitates oriented in the same fashion in any individual grain (bottom row, Fig. 3.15).

3.2.4 Non-equilibrium processing morphology

Non-equilibrium processing provides additional dimensions of control in material systems in which equilibrium based processing routes do not. The resulting morphology is created by initially forcing a system into a metastable state, and then rapidly bringing it back into equilibrium (detailed in Fig. 3.16). However, akin to the discussion of free energy balancing in nucleation and growth for nuclei formation, the initial shape to balance out the free energy is typically spheroidal due to the small structure size.

This is most likely due to the inherent large chemical driving force in compounds with large heats of solution, increasing the nucleation rate and ultimately the number density. Under the assumption of spherical nuclei and the fact that the equilibrium volume fraction will be fixed by the phase diagram, the structure size is expected to be small, possibly approaching the critical radius for stable nuclei, r^*, according to

$$f_v = \frac{4}{3}\pi r^3 N_v, \tag{3.4}$$

where f_v is the volume fraction, r is the nuclei radius, and N_v is the number density. Therefore, for a fixed value of f_v and an increase in N_v due to the increased nucleation, the nuclei radius will decrease. If the increase in N_v is large enough, it is possible for the actual structure radius to be near the value of the critical radius, r^*. Thus, as discussed in the previous section, the balancing of the volumetric and surface free energies results in a spheroidal morphology (Fig. 3.17).

3.3 Control of length scale and implications

It is important to describe quantitatively what the definition of *fine* microstructure is for thermoelectric materials. The early works in Si-Ge alloys claimed that significant reductions can be achieved at a mean structure size of 2 μm [74, 75, 7]. While this may be true in Si-Ge alloys, the spectral nature of thermal conductivity dictates that structure size and scattering is material dependent, arising from the varied phonon dispersions in different material systems. Therefore, it is reasonable to expect an array of structure sizes and spacings can benevolently affect κ_l for thermoelectric applications. In PbTe for example, calculations were conducted with the conclusion that 80% of the heat carrying phonons had a mean free path that spanned nearly two orders of magnitude ($50-1000$ nm) [76]. Moreover, other authors calculated that if the phonon mean free path was limited to 100 nm in PbTe, there would be a 20% reduction in the total thermal conductivity [77]. It was further asserted that to achieve a thermal conductivity reduction of 40% in PbTe would involve decreasing the phonon mean free path an order of magnitude further to 10 nm. These works elucidate the idea that it is possible to achieve a significant thermal conductivity reduction through structure sizes and spacings larger than recently predicted [78, 79], but smaller than originally thought [74, 75, 80].

3.3.1 Solidification

Solidification of materials at or around critical points, such as eutectic or peritectic reactions, has been known to produce a spectrum of different microstructure types. Even though the resulting microstructural differences often dictate morphology specific parameters to fully quantify the structures, one universal parameter that controls length scale during solidification is the cooling rate, R_{LS}. It is in understanding the cooling rate that can lead to information about the onset and completion of solidification and also quantifiable predictions to size scales of the potential structures.

In order to quantify the cooling rate, R_{LS}, during solidification it is necessary to identify the initiation and termination points of solidification. This information is garnered from experimental T vs t cooling curves. In the simplest case, the material should experience thermal arrest during solidification. Specifically at the points of initiation and completion, the cooling curve will exhibit local extrema in $\frac{\mathrm{d}R_{LS}}{\mathrm{d}t}$. If we assume a simple binary eutectic phase diagram, it would be expected that the initiation and completion stages would occur at the liquidus (initiation) and eutectic (completion) temperatures. From the T vs t curves, the onset of solidification will be a local minimum due to the significant drop in cooling rate as the material traverses from the pure liquid to the solid-liquid region, as it will no longer be compensated by the latent heat of fusion, and the cooling rate will increase once again. Once the onset and completion temperature and time have been well defined, it is a simple matter of calculating $R_{LS} = \frac{\Delta T_{LS}}{\Delta t_{LS}}$.

Once the cooling rate is established, it is possible to be quantitative about controlling the resulting structural features. Cooling rate effects on structure size have been extremely important for improving the yield strength in metals and have been studied extensively [81]. In the case of the PbTe-Sb_2Te_3 thermoelectric system, Ikeda employed the inter lamellar spacing, or layer spacing, λ, for the layered faceted structures and secondary dendritic arm spacing, d_s, as characteristics to compare microstructural sizes [37]. Inter lamellar spacing is the spacing between the central points of the areas of compositional discontinuity. More simply put, it is the spacing between the center points of two adjacent structures in the material. This is calculated for many structures, in many domains across the material. Obviously this trait only applies to materials in which layered structures are the primary type. Secondary dendritic arm spacing is the spacing between the secondary arms that form on dendritic structures. This can be imagined as the primary dendrite arm as a saw blade, and the secondary arms as the teeth on the blade.

Cooling rate is often empirically described for dendritic systems related to d_s by [82]:

$$d_s \propto \frac{1}{R_{LS}^n}, \tag{3.5}$$

where n is an empirical constant and R_{LS} is the liquid-solid cooling rate. The value of $n = 0.32$ in PbTe-Sb_2Te_3 is similar to those reported in the literature, as typical values of n range from 0.25 for most Al alloys up to 0.48 for Sn-Pb alloys [37]. In looking at Eqn. 3.5 it is obvious that for a system of primarily dendritic microstructure formation, the larger the solidification rate the finer the microstructure.

The determining factors controlling the inter lamellar spacing however are not as straightforward. The layer spacing, λ, for a simple eutectic reaction during nucleation is described by [83]:

$$\lambda^2 \nu \propto \text{const.}, \tag{3.6}$$

where ν is the solidification velocity. According to Eqn. 3.6, λ is expected to decrease for an increased solidification velocity. It is a reasonable assumption that this is directly related to the cooling rate, therefore a larger cooling rate will decrease the layer spacing. However, there is an inherent drawback to using solidification techniques with thermoelectric materials due to their low thermal conductivities as it leads to low solidification velocities. For example, to achieve structure sizes on the order of what is typically desired ($\sim$100 nm) in the PbTe-Sb_2Te_3 system, this would require a cooling rate upwards of 10^5 K/s [37], which can be difficult to achieve when the internal heat transfer of the solidifying material is low.

Still, results of measurements in the PbTe-Sb_2Te_3 system involving the structure size dependence on solidification rate support the idea that a faster cooling rate results in finer microstructure (Fig. 3.7). Even though the PbTe-Sb_2Te_3 system's inherent low thermal conductivity requires a very large cooling rate for thermoelectric applications, there are techniques that could potentially achieve this. Splat cooling is a candidate that involves rapidly solidifying a thin layer of liquid on a cooled surface [84]. A version of splat cooling called melt spinning [85] has been widely used in the amorphization of materials, most notably metallic glasses [86]. Melt spinning has been used in thermoelectric materials, however the focus tends to be in making nanocrystalline material [87, 88, 89]. There has been a recent trend of attempting to correlate the effect of cooling rate on the resulting transport properties [90, 91], however quantitative microstructure control is often not considered.

3.3.2 Eutectoid reaction

Controlling microstructure formation via eutectoid reaction works on the idea that if one starts with a solid phase that becomes metastable below some critical temperature, it is possible to generate fine microstructure through the decomposition of this metastable phase into two new, energetically favorable phases ($\gamma \rightarrow \alpha + \beta$). Similar synthesis routes can be used in peritectoid reactions, with the difference being that the metastable phase separates upon an increase in temperature beyond the critical point. However, here the focus will remain on eutectoid reaction based microstructure formation. The parameters for controlling the microstructure size and spacing are the time for the reaction to take place and the temperature at which the event occurs. Early metallurgical works in Cu-Al alloys [62] and Co, Cu and Ni alloys [65] laid the groundwork in establishing that a large undercooling results in a fine layer spacing in eutectoid systems. With regard to thermoelectric materials, we visit the PbTe-Sb_2Te_3 system and find that the starting metastable compound $Pb_2Sb_6Te_{11}$ will react to form lamellae of PbTe and Sb_2Te_3 (Fig. 3.8).

The complexity of the inter lamellar spacing during nucleation makes for difficult modeling, however there have been several investigations to model the coarsening of eutectic and eutectoid microstructure. Graham and Kraft modeled $\lambda(t)$ of the Al-$CuAl_2$ eutectic system based on fault migration [92] which led to a linear time dependence ($\lambda(t) \sim t$) of the lamellar spacing. Cline used a similar approach to model coarsening, however also included fault annihilation and derived a $t^{1/2}$ dependence [93]. However, the data for the PbTe-Sb_2Te_3 system did not present a linear time dependence with respect to lamellar spacing. In fact, as can be seen in Fig. 3.9, there was a decelerated coarsening with time, which is better represented by the power law developed by Cline ($t^{1/2}$) but even this still did not fit well with the data [38].

In order to better understand the coarsening method in the PbTe-Sb_2Te_3 system it would be beneficial to obtain more kinetic data and develop more thorough models. A route to enhance existing models could be to incorporate a Kolmogorov-Johnson-Mehl-Avrami (KJMA)[94, 95, 96, 97, 98] like equation to the methods of either Graham and Kraft[92] or Cline [93]. The KJMA equation, which takes the form

$$f = 1 - \exp(-kt^n), \tag{3.7}$$

and represents the percentage of volume fraction transformed in nucleation and growth based microstructure, could establish a more realistic deceleration in lamellar spacing.

The temperature dependence of lamellar spacing was very well described by Zener [83] in his studies of the kinetics of austenite decomposition. He developed the idea that the layer spacing at the onset of coarsening is related to the undercooling by

$$\lambda = \frac{4\gamma T_E V_m}{\Delta H \Delta T}, \tag{3.8}$$

where γ is the surface energy, T_E is the eutectoid temperature, V_m is the molar volume, ΔH is the enthalpy difference between the eutectoid and supercooled material at the onset of nucleation, and ΔT is the undercooling. This expression implies that the further below the eutectoid temperature the reaction takes place, the smaller the layer spacing. This idea is well supported by the λ data of PbTe-Sb_2Te_3 (Fig. 3.9) as the lamellar spacing decreases as the undercooling increases. The benefits of the resulting spacing due to the large undercooling can be seen in the lattice thermal conductivity data (Fig. 3.10) as well, where there is a large decrease in κ for large ΔT. The temperature dependence of this spacing is limited, however, as it is unlikely that for extremely large undercoolings the reaction kinetics will allow significant microstructure formation. The beginning of such a limitation can be seen in Fig. 3.9, as the dependence of λ on the reaction temperature decreases for the samples below 500°C.

A secondary parameter to tune would be the surface, or interface energy, γ. Due to the inherent difficulty in directly tuning the surface energy, it is more a consideration that can be taken to promote smaller lamellar spacings that are beneficial for thermoelectrics. For example, if the two constituent materials involved in the reaction are known to have low energy incoherent interfaces, this could be an important deciding factor that can help reduce the inter lamellar spacing.

There is also the added benefit of eutectoid reactions over eutectic reactions for thermoelectric applications because of the kinetic nature of solid state reactions. Diffusion in the liquid state is considerably faster than in the solid state, so when a eutectoid reaction takes place, the diffusion is markedly slower. The end result of such diffusion is that the resulting microstructure often has a higher number density for a similar volume.

It should be noted that measured layer spacing for in-grain lamellae is strongly dependent on the orientation relative to the viewing plane. Lamellae that lie perpendicular to the viewing plane will appear to have a smaller layer spacing than those that are not. Therefore, when measuring layer spacing, it is necessary to account for this discrepancy and calculate the true lamellar spacing [100].

3.3.3 Nucleation and growth precipitation

Because the synthesis procedure for nucleation and growth based precipitation as described in Fig. 3.4 is also a solid state reaction, it has the same microstructural advantages as that of eutectoid microstructure. However, the nucleation and growth of precipitate based microstructure is dependent on three parameters. The temperature at which the phase segregation takes place, the composition of the material based on the phase diagram, and the duration of the event all control the resulting size and spacing during the transformation. This type of microstructure formation is often used with great success in the strengthening of Al [101] and Fe [102] alloys and is often referred to as age or precipitate hardening [103]. There is an overlap in control parameters between eutectoid and nucleation and growth based reactions, however. In the latter case the composition is not as limited by critical points on the phase diagram, therefore allowing more variability in the volume fractions of constituent phases.

There is, however, a compositional limitation set by the phase diagram for nucleation processes. If a eutectic phase diagram is considered, this limitation is dictated by the maximum solubility of the secondary phase in the host material. As can be seen in Fig. 3.4, a typical synthesis route to precipitate a secondary β phase in a matrix of α would be to first melt the constituent elements, then homogenize the material and finally precipitate the desired microstructure. Therefore, it is imperative to have a strict understanding of the solvus line (the line separating the α or β phases from the $\alpha + \beta$ region) to quantitatively control the resulting microstructure. Unidirectional solidification experiments, such as the Bridgmann method, can be used to determine the maximum solubility [12, 41, 104], and isothermal annealing experiments can be conducted to map out the pertinent portions of the solvus line.

Once there has been some determination of the solvus line, it is necessary to understand the effects of undercooling (ΔT) and supersaturation (Δc). In this case, the undercooling is defined as the difference in temperature from the solvus line and the temperature of the material when $T < T_{\text{solvus}}$. The supersaturation on the other hand corresponds to the amount of excess solute in the material when $c > c_{\text{solvus}}$.

Fig. 3.11a is a schematic of a binary eutectic phase diagram, and the corresponding free energy curves associated with the isotherm indicated by the horizontal dashed line (Fig. 3.11b). It is assumed that the two compositions considered have a similar undercooling with the main difference being the supersaturation levels; with one having a higher solute content than the other ($c_2 > c_1$).

As can be seen in Fig. 3.11b, the lowest free energy curve for compositions c_1 and c_2 is the common tangent, indicating that the lowest energy configuration dictates a phase separation. Moreover, the chemical driving force, which is related to the tangent of G_α (at c_1 or c_2) at the composition near the tangent point of G_β, increases as the composition is increased from c_1 to c_2. Therefore, the larger chemical driving force for c_2 (ΔG_2) indicates there will be a stronger drive for nucleation than c_1 (ΔG_1).

This supersaturation trend can be seen in the nucleation and growth work done within the PbTe-Ag_2Te system (Fig. 3.12) [10]. The Ag_2Te content was increased in four increments over the same isotherm, and resulted in an increased number density due to the increased nucleation driven by the larger supersaturation. Because of this, there was a large reduction in the thermal conductivity reduction as seen in Fig. 3.12 and was the basis for improving both n- and p-type PbTe.

The variable composition cooling experiments in the PbTe-Sb_2Te_3 system (Fig. 3.13) had slightly contradictory results, however [11]. Two similarly structured samples of different composition were analyzed and the lower solute concentration sample resulted in a larger number density, which would imply a larger chemical driving force. However, the synthesis routine consisted of slow cooling (10 K/hr) as opposed to isothermal annealing, and the larger solute containing sample's solvus temperature was higher, schematically depicted with triangles in Fig. 3.11a, which led to a longer duration in the two-phase region and significant coarsening. This is an example of how the undercooling and supersaturation can change simultaneously, which makes decoupling their effects difficult.

Despite this difficulty however, it is possible to describe the effects undercooling in the context of the critical free energy and radii of nucleation. From a thermodynamic standpoint, in order for nucleation to occur there must be an overall lowering of the free energy due to the volume of the second phase formed. This is opposed by the increase in free energy due to the surface energy between the matrix and secondary phase. In nucleation during solidification, these are the important terms that dominate the phase formation, however in solid state nucleation there is a misfit strain relation to consider because the newly formed phase often does not fit perfectly into the allotted volume on account of differing lattice parameters, crystal structures, and often both.

Taking into account this misfit strain, the total free energy change (ΔG) is altered from Eqn. 3.3 to

$$\Delta G = \frac{4}{3}\pi r^3 \left(-\Delta G_V + \Delta G_S\right) + 4\pi r^2 \gamma, \tag{3.9}$$

where γ is the surface free energy, and ΔG_V and ΔG_S are the volumetric and strain free energy terms. If a spherical nucleus is assumed, then the critical radius, r^*, and critical free energy for nucleation, ΔG^*, are

$$r^* = \frac{2\gamma}{(\Delta G_V - \Delta G_S)}, \tag{3.10}$$

and

$$\Delta G^* = \frac{16\pi\gamma^3}{3(\Delta G_V - \Delta G_S)^2}, \tag{3.11}$$

where ΔG_V is proportional to ΔT, which is the undercooling. The temperature dependence of these critical values can be seen schematically in Fig. 3.14 as the undercooling is inversely proportional to both. The expected trend of finer microstructure with larger undercooling is observed in several thermoelectric systems, as seen in Fig. 3.15, including but not limited to PbTe-Sb_2Te_3 and Bi_2Te_3-In_2Te_3 [11, 24]. In these cases the precipitate size and spacing decreased drastically as the undercooling increased for various annealing temperatures.

Based on the thermodynamic equations describing undercooling, it would be expected that arbitrarily increasing the undercooling would correspond to a proportional increase in nucleation. For long annealing times this may be true, however, there are kinetic limitations to consider. For example, increasing the undercooling such that it approaches absolute zero would not likely result in significant microstructure formation in most materials due to the lack of diffusion at such temperatures. In fact, due to the balancing of thermodynamics and kinetics, the fastest nucleation rate is often at an intermediate undercooling [105].

In practice it is commonly difficult to separate the effects of supersaturation and undercooling because of the slope of the solvus line. As can be seen in Fig. 3.11 and 3.14, as one changes either the annealing temperature or the composition, it simultaneously affects both the undercooling and supersaturation. Therefore, from a materials architecture standpoint, it is necessary to establish the degree of sensitivity of each parameter by conducting individual studies of both undercooling and supersaturation to attempt to determine which has the greatest influence regarding microstructure optimization.

Fortunately there is a simple and effective determining length scale to judge how rapid nucleation is, and also when nucleation is complete. This information lies in the characteristic diffusion length l:

$$l \propto \sqrt{Dt}, \tag{3.12}$$

where D is the temperature dependent diffusion coefficient of the solute, and t is the time in which the diffusion at this temperature takes place.

According to the soft impingement effect [67], when the distance between precipitates is less than or equal to l it is expected for nucleation to have reached its conclusion. This should be treated as an order of magnitude approximation, but is an important feature because of its simplicity. For example, if the diffusion coefficient of a secondary phase diffusing in a host matrix material is known, it can be estimated how long it would be necessary to anneal a sample to reach complete nucleation for a desired structure spacing. For materials with very low diffusion coefficients this can save an experimentalist a large amount of time in determining the best candidate for microstructure formation.

There is room for improvement regarding the tuning of the interfacial area per unit volume, an important parameter in thermal conductivity control. For thermoelectric applications it is desired to have a large interfacial area per unit volume as it has been shown that this results in a large reduction in κ [106, 77]. However, in nucleation and growth, altering the supersaturation and undercooling only significantly alters the number density. Assuming geometrical similarity for the same morphological microstructure (maintaining the same aspect ratio, volume fraction, and average diameter to inter-plate distance) [11], the three dimensional limitation to interfacial area per unit volume is governed by

$$A_V = C N_v^{1/3}, \tag{3.13}$$

where A_V is the interfacial area per unit volume, C is a constant and N_V is the number density of precipitates. In order to improve the ratio of interfacial area to volume by a factor of two, it would involve an eight fold increase in the number density, a demand that often times far outreaches the possibilities in a nucleation and growth based scheme. Therefore, unless the interfacial area to volume is naturally in the optimal regime to allow for significant thermal conductivity control, it is difficult to significantly alter A_V via supersaturation and undercooling alone.

However, material selection in and of itself can be considered a control parameter. The heat of solution is directly proportional to the chemical driving force (ΔG in Fig. 3.14b) [107], whereby a larger heat of solution leads to a larger chemical driving force, and stronger nucleation. Therefore, a precipitating candidate with a large heat of solution can be chosen as this acts to increase the intrinsic value of N_V. This is evident when comparing the number density data of PbTe-Ag_2Te and PbTe-Sb_2Te_3. For comparable annealing temperatures and annealing times the number density of the Ag_2Te structures outnumbers that of Sb_2Te_3 as seen in Table 3.2. This is due to the fact that ΔH_s is much higher for Ag_2Te than Sb_2Te_3 in PbTe.

Table 3.2: The number density, N_v, and heats of solution, ΔH_s, for Ag_2Te and Sb_2Te_3 in PbTe.

Precipitate	T (°C)	t (hr)	N_v (μm^{-3})	ΔH_s (kJ/g-atom)	ref.
Ag_2Te	500	72	55 ± 30	14.0 ± 3.5	[104, 10]
Sb_2Te_3	450	38	15 ± 3	4.4 ± 0.2	[104, 41]

3.3.4 Non-equilibrium processing

In the previous section it was discussed that a large heat of solution leads to a large chemical driving force for nucleation, which in turn results in a large precipitate number density (Table 3.2). However, materials with large heats of solution tend to have little solubility and typically form line compounds. Therefore, eutectoid and the typical nucleation and growth reactions are insufficient methods to produce a second phase necessary for thermoelectric applications in these types of materials.

Fortunately, steps have been made via metastable non-equilibrium processing, such as rapid solidification (RS), mechanical alloying (MA) and mechanical milling (MM) to improve such solubility limits. Turnbull described the methods as routes to "energize and quench" the metastable states [108]. The techniques involve imparting enough energy to the material ("energize") to take it far from equilibrium and then attempt to retain this configuration ("quench"). In an RS process the far from equilibrium energized state is the (disordered) liquid state, or more specifically, it is the amorphous solid state that forms immediately after quenching, and rapid cooling attempts to maintain the far from equilibrium state. In MA/MM, the energized state is the localized highly disordered state where the milling media comes into contact with the material and there is very little lattice relaxation after this event (if any) due to the low processing temperature.

As can be seen in Fig. 3.16a, when the material at composition c_1 is at temperature T_2, the liquid state has the lowest free energy, thus this high entropy state is the most stable. However, if the cooling rate is rapid enough (Fig. 3.16b), immediately after quenching the energized free energy curve (G_{en}), which could be a metastable crystal structure or amorphous state, is reached and even though G_α is not the lowest energy configuration, the system can rest in this metastable state because it has a lower free energy than the previously occupied energized state. This scenario occurs if T_1 is low enough to prevent phase decomposition, which would require long range diffusion. The relaxation from G_{en} to G_α is possible because it can occur via short range diffusion, therefore, there can be short range lattice relaxation and the material can be maintained on the G_α curve, as seen by the middle point in Fig. 3.16b, thus increasing the solubility from c_e to c_1.

The free energy curves look very similar for MA/MM compared to RS processes as can be seen in Fig. 3.16c. During an MA/MM process, milling media (often stainless steel spheres) constantly fractures and welds material. As depicted in Fig. 3.16c, a material at composition c_1 that undergoes a milling event is locally brought up to the energized state, and after enough time (~20-100 hours

[109, 110, 111]) all of the material is brought up to this energized state. Just like in RS, this state can be either a metastable crystal structure or an amorphous state, however unlike rapid solidification, MA/MM processes have an easier time maintaining this state because the reaction kinetics are significantly slower on account of the low processing temperature.

Also different than RS processing is that the increased affected surface area in MA/MM events results in the ability to take a material further from equilibrium than is usually possible by rapid solidification. This is beneficial as the further from equilibrium state leads to a larger solubility extension for systems with a larger heat of solution. Finally, since thermal conductivity severely limits the solidification rate, it can be difficult to achieve the cooling rates necessary to increase the solubility in an RS process as thermoelectric materials tend to have very low thermal conductivities.

Additionally, non-equilibrium processing decreases the microstructural restrictions set by the equilibrium phase diagram. By superseding the equilibrium solubility limit it allows for a wider array of nanostructuring elements to be chosen that may have not been possible by equilibrium methods. This is especially true for materials that have large energy requirements to reach a non-equilibrium state, such as in line compounds.

An example of a thermoelectric material that is a line compound with a large heat of solution is Mg_2Si. It was shown that upon Si excess ($Mg_{63.3}Si_{36.7}$) and significant milling times (120 h) it was possible to eliminate the pure Si peaks from the X-ray diffraction spectra, whereby upon consolidation via hot pressing, the Si and Mg_2Si peaks would revert back to the normal spectrum resulting in fine microstructure (Fig. 3.17) [112]. It is not known whether this was due to an amorphization of the material, or if the size of the Si particles became sufficiently small to broaden the peaks in the X-ray spectra, however transmission electron microscopy (TEM) and small angle X-ray scattering (SAXS) measurements verified nanoparticle formation, and established the resulting bimodal size distribution peaking at values of 7 nm and 40 nm, consistent with the TEM results. It was shown that through this technique the lattice thermal conductivity (κ_l) could be significantly reduced relative to pure Mg_2Si, however further work is needed to control the electron mobility and oxidization from the extended milling to use this material in a thermoelectric application.

3.4 Microstructure characterization

Microstructure quantification relies heavily on characterization techniques in order to make suitable conclusions about the resulting structures. It is beneficial to know what techniques are available and also which are appropriate to use at a given time. In characterizing lamellar structures by scanning electron microscopy for example, the observed spacing as obtained from micrographs is not the true value. In fact, unless the lamellae are completely parallel to one another and perpendicular to the observation plane the spacing will be skewed as shown in Fig. 3.18a. Fortunately, the experimentally determined lamellar spacing distribution can be straightforwardly fit to [100]:

$$F = \frac{\int_{\lambda_1}^{\lambda_2} N_\lambda \, \mathrm{d}\lambda}{\int_0^\infty N_\lambda \, \mathrm{d}\lambda}, \tag{3.14}$$

where F is the fraction of lamellar spacings for a given interval ($\Delta\lambda$) and N_λ is the number of lamellar spacings, with

$$N_\lambda = \frac{1}{\lambda^3} \left(\int_0^\lambda \mathrm{e}^{-\frac{(\lambda_0 - \lambda_{0,\mathrm{avg}})^2}{2\sigma^2}} \frac{\lambda_0^2}{\sqrt{\lambda^2 - \lambda_0^2}} \mathrm{d}\lambda_0 \right), \tag{3.15}$$

where λ, $\lambda_{0,avg}$, and σ are the *apparent* lamellar spacing, average *true* lamellar spacing, and the standard deviation of the average *true* lamellar spacing. Once the values of $\lambda_{0,avg}$ and σ are determined it is possible to calculate the true lamellar spacing distribution, as can be seen in Fig. 3.18b for the PbTe-Sb_2Te_3 system. This method is valid when the true lamellar spacing distribution is Gaussian and for regions of the SEM micrographs in which the microstructure is lamellar. This method breaks down for areas in which the lamellae have coarsened and/or the transformation mechanism results in non-lamellar microstructure. In such cases there is a technique developed by Cahn and Fullman [113] that necessitates a larger sample size, however with sufficient data converges to the true spacing distribution. The issues in determining true vs. apparent spacings exist for other morphology types as well, and there are other established methods in determining those values [11].

Transmission electron microscopy has also been used to incorporate pertinent quantities of observed defects, such as dislocation density, boundary length, and precipitate size/spacing [114] into established thermal models [115] to better understand the correlations of microstructure and lattice thermal conductivity. Although, a word of caution about transmission electron microscopy preparation is necessary in the discussion of microstructure observation. In PbTe based specimens, it was determined that artificial nanoscale “features” can be created during the ion milling step of materials preparation. It was discovered that unless the sample was cooled to a range of 140-160 K artificial features of a similar size and morphology were created [73]. Therefore it is important to be aware the potential artifacts that can be created, intentional or otherwise.

Quantities which can characterize the size scales pertinent to these structuring techniques are summarized in Table 3.3. A direct way of measurement is to analyze the two dimensional micrographs and convert the results to three dimensional quantities using stereological relations [116]. Number density, N_v (per volume), for example, can be evaluated from the two dimensional N_A (number density per area) using the stereological relation $N_v = N_A d^{-1}$, where d is the average feature size. This value varies depending on the feature morphology as d for spherical particles is the diameter [116] and it is the radius for circular plates [11].

In order to obtain statistically sound information for a given sample, it is necessary to analyze a large number of micrographs. In SEM observations, caution should be exercised if the size scale is in the nanometer range since the samples may become transparent to the incident beam. Otherwise, such quantities as number density, N_v, volume fraction, f_v, or feature size, d, of structure phases can be overestimated. Therefore, it is necessary to establish methods to corroborate the independent techniques. Volume fractions of constituent phases (f_i) can be obtained by the Rietveld analysis of powder X-ray diffraction (XRD) spectra and volume fraction can be calculated in systems that have established phase diagrams via the lever rule. To obtain information regarding size scales such as feature size, d, thickness, t, or spacing, l, powder XRD with the aid of Scherrer's equation [117] or small angle X-ray or neutron scattering can be used if the structures are less than 100 nm.

The interrelations between these quantities listed in Table 3.3 can be used to check the consistency of measurements or to determine a quantity which is not measured. In the right column, interface density (A_v, area per unit volume) is listed using average feature size (and volume fraction). The number of intersections per length on a random line in a three dimensional space N_l is related to A_v as $N_l = \frac{1}{2}A_v$ [116]. Therefore, if the mean intersection length ζ is defined as $\zeta \equiv N_l^{-1} = 2A_v^{-1}$, ζ readily describes the average distance with which phonons encounter boundaries.

Table 3.3: Major microstructural morphologies and their quantification techniques

Morphology	Process Reaction	Quantity	Inter-relation	Interface density
Grain Size	Powder metallurgy Solidification	Grain diameter, d	–	$3d^{-1}$ [a]
Grain boundary phase	Powder metallurgy Solidification + Precipitation	Grain diameter, d Thickness, t Volume fraction, f_v	$f_v = 3dt^{-1}$	$6d^{-1}$ [a b c]
Dendrite	Solidification	Secondary dendrite arm spacing, d_s	–	–
Lamellae	Eutectic Eutectoid	Interlamellar spacing, λ Lamellar width, t_1, t_2 Volume fraction, f_1, f_2	$\lambda = t_1 + t_2$ $f_1 = t_1\lambda^{-1}$ $f_2 = t_2\lambda^{-1}$ $f_1 + f_2 = 1$	$2\lambda^{-1}$ [d]
Modulated Structure	Precipitation Spinodal decomposition	Wavelength, L Volume fraction, f_v	–	–
Rod precipitates	Eutectic Eutectoid Monotectic Monotectoid Precipitation	Number per volume, N_v Rod diameter, d Rod length, l Volume fraction, f_v	$f_v = N_v l\pi \left(\frac{d}{2}\right)^2$ $f_v = N_p\pi \left(\frac{d}{2}\right)^2$ N_p: per area perpendicular to rods aligned	$4f_v d^{-1}$ [e]
Plate precipitates	Precipitation	Number per volume, N_v Area per plate, A_p Thickness, t Volume fraction, f_v	$f_v = N_v A_p t$	$2f_v t^{-1}$ [ef]
Spherical precipitates	Eutectic Eutectoid Monotectic Monotectoid Precipitation	Number per volume, N_v Diameter, d Volume fraction, f_v	$f_v = \left(\frac{4}{3}\right) N_v\pi \left(\frac{d}{2}\right)^3$	$6f_v d^{-1}$

---

[a] d is equivalent sphere diameter. For other model shapes see [116]

[b] For $t \ll d$

[c] Phase boundary density, which is two times the grain boundary area per volume, is shown for A_v

[d] The interlamellar spacing should be the "true" interlamellar spacing [100]

[e] Only the large surface is taken into account

[f] Phase boundary density, which is two times the plate area per volume is shown for A_p

3.5 Beyond κ_l, tuning carrier concentration

Upon quantitatively establishing a successfully structured material, it is necessary to verify the extent to which the optimal carrier concentration can be approached. If the resulting microstructure acts to inhibit electron transport, the resulting nanostructured material would run the risk of removing the benefits from the thermal conductivity reduction. This would lead to a resulting material with an overall lower zT than one started with, an obvious mishap sometimes seen in functional material design.

The most successful system with regard to optimized thermoelectric properties structured via nucleation and growth is the PbTe-Ag_2Te system. Seen in Fig. 3.19 is the thermal conductivity data for both Na and La doped PbTe. This is a remarkable feat, as the Ag addition not only was a suitable candidate for microstructure generation, but also left the carrier concentration low enough ($\sim 10^{17}$ cm^{-3}) that it could be considered an intrinsic semiconductor [9, 10]. Upon addition of La there was a significant increase in carrier concentration and on account of the Seebeck coefficient optimization, resulted in enhanced thermoelectric properties as an n-type semiconductor. A similar story resulted in the Na doped case, however the conductivity was p-type.

An often encountered problem with carrier concentration control, however, is the generation or depletion of carriers due to the microstructure formation. For example, in the case of Sb_2Te_3 structures in PbTe via nucleation and growth, the equilibrium composition of the cases that have the best results for thermoelectric applications tend to be over doped (n-type) due to excess Sb dissolved in the matrix, well beyond the optimal carrier concentration for n-PbTe [12]. In order to combat this, it would be necessary to counter dope the material with an acceptor impurity (such as an alkali metal) or decrease the amount of residual dopant in the matrix in order to decrease the carrier concentration to the desired level.

Increasing the number of constituent elements in these materials has drawbacks, however. Most high efficiency thermoelectric materials are binary compounds and incorporating an element to generate microstructure transforms them into ternary compounds. The chance of the nanostructured compound having the optimal carrier concentration for thermoelectric purposes is possible but low, so it is expected that a material structured and then extrinsically doped will ultimately be quaternary in nature.

The resulting chemical complexity can lead to solubility limits in these types of materials. For instance, the solubility of Na in PbTe is limited by the inclusion of Ag_2Te as evidenced by the maximum carrier concentration achieved being less than the optimal value in Na doped PbTe without structures [9, 118]. While in the case of the extremely low solubility system of Bi and As, the alloying of Bi with Sb increases the solubility of As with respect to (Bi,As) in order to achieve fine microstructure [119, 120]. It is unclear whether these limits correspond to a change in thermodynamics, or if the source of the inhibition is the interfacial strain induced by the microstructure. Whatever the case may be, it is important to understand the difficulties associated with microstructure formation of this nature.

The chemical complexity becomes especially important in materials due to either crystal or microstructural anisotropy where directionally dependent transport measurements are necessary to understand the fundamentals governing materials design. Such systems require advanced synthesis techniques for single crystal growth or grain orientation/texturing such as directional solidification or zone melting. However, through rigorous understanding of the phase diagram of a given system it is possible to alleviate this concern because the most important parameters to utilize these synthesis techniques require a critical knowledge of the liquidus and solidus lines. Furthermore, as previously discussed, the nature of the solvus line is vital in certain aspects of microstructure formation and control.

3.6 Conclusions

Presented here are several techniques that involve composite formation and quantitative microstructure control to reduce the lattice thermal conductivity as a means to improve zT for thermoelectric applications. Relevant to microstructure control are the tunable parameters, such as temperature, composition and time, which are the most important first order controls. Here we go beyond these parameters and show how materials design can be controlled when considering other synthesis specific properties such as entropy of fusion, crystal structure similarity and lattice parameter mismatch. Because much of this microstructure control stems from the energetics and relationships of phases in equilibrium phase diagrams, computational techniques to determine these phase diagrams [121, 122, 123] will rapidly become a powerful tool as they become faster and more accurate.

Even though thermal conductivity reduction is a proven method to significantly enhance zT in thermoelectric materials, it will be necessary to move beyond this technique to advance the state of the art. Next generation materials design will have to also incorporate improved electronic properties to see real success as functional materials. However, these advances may be closer to reality than at first glance, as strides are being made in a new avenue of thermoelectric design through band structure engineering techniques [124]. These techniques act to improve the thermoelectric properties by manipulation of the band structure in a material, with examples as simple as alloying to widen band gap [125] or the more intricate band alignment to increase the band degeneracy for a given carrier concentration [118, 126, 127, 128].

While the application of band structure modifications is relatively new, it is certainly possible to combine the effects of band structure engineering with thermal conductivity reduction by nanostructuring and achieve a synergistic result. In fact, in the case of the Na doped PbTe-Ag_2Te system it is already taking advantage of the increased band degeneracy of PbTe with sufficient Na doping. The results are not as prominent as one would desire with respect to peak zT because of the limited Na solubility in the presence of Ag_2Te, however the average zT in this material is one of the highest on record due to the near room temperature thermal conductivity reduction [9].

This is just one of the possibilities regarding the coupling of power factor enhancement and thermal conductivity reduction. While this avenue of thermoelectric optimization has not been fully explored, it is a clear indication that future materials design in bulk thermoelectrics will need to seek simultaneous enhancements of material properties.

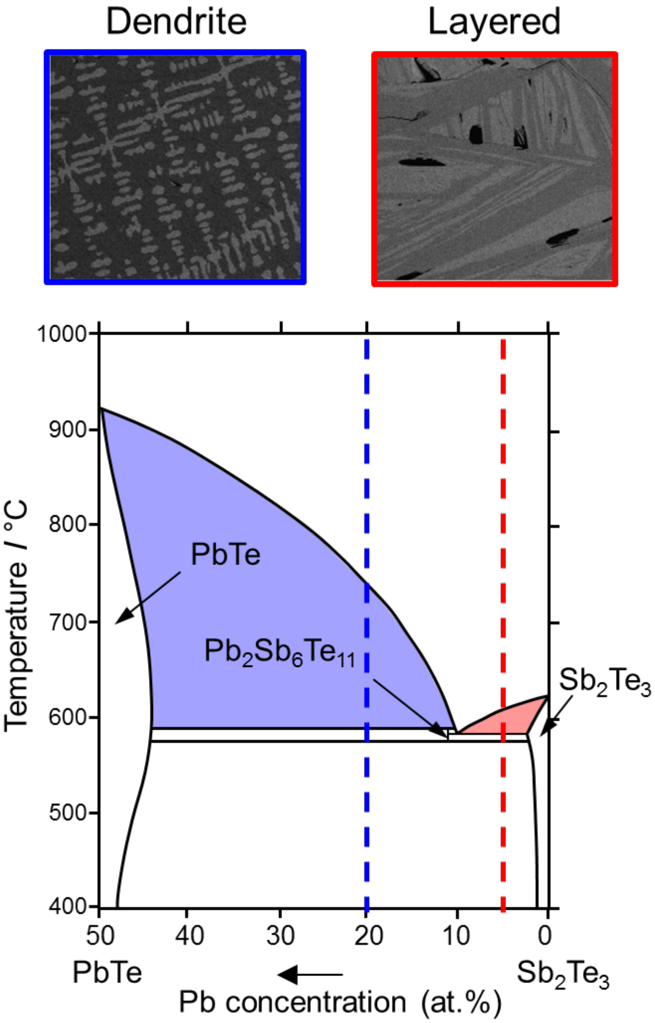

Figure 3.2: Even in the same material system it is possible to generate different microstructure based on the details outlined in Eqn. 3.1 and 3.2. In the case of the pseudo-binary PbTe-Sb_2Te_3 system, to the PbTe side of the eutectic solidification experiments yield a dendritic microstructure, while to the Sb_2Te_3 portion experiments yield a layered faceted microstructure [37] (figure adapted from [39]).

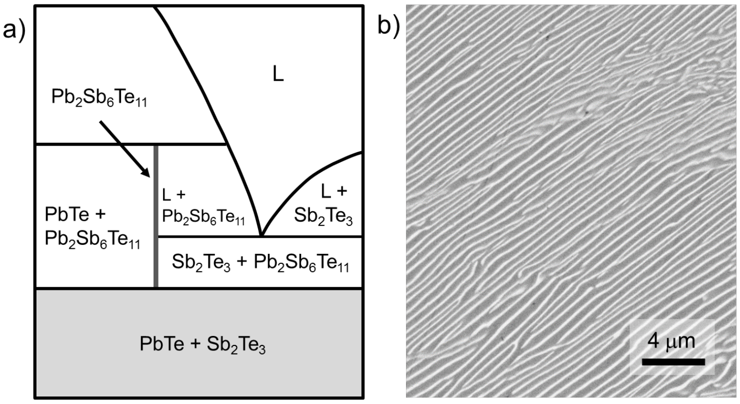

Figure 3.3: (a) A magnified section of the PbTe-Sb_2Te_3 phase diagram near the $Pb_2Sb_6Te_{11}$ eutectoid compound [39] and (b) an electron micrograph of the resulting directional cooling experiments for the eutectoid reaction of $Pb_2Sb_6Te_{11}$ to PbTe-Sb_2Te_3. The resulting microstructure is aligned in a similar fashion to the directional solidification experiments that were the basis of the morphological control [42]. (Figure adapted from [39]).

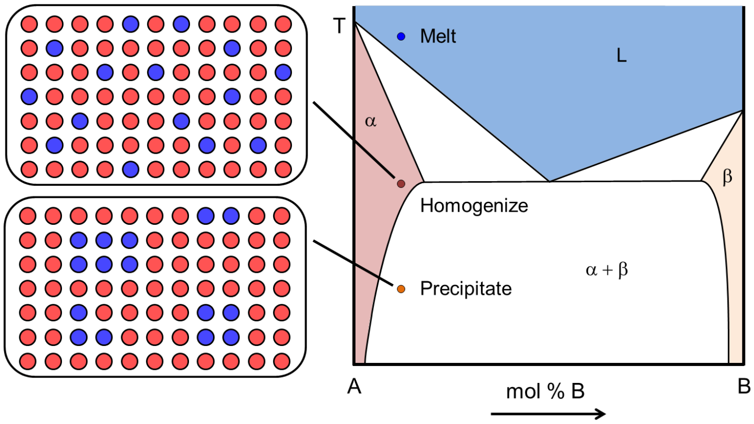

Figure 3.4: A schematic of the processing route undertaken in nucleation and growth based microstructure formation. The material is initially melted, then homogenized and finally the isothermal annealing temperature is decreased such that it exploits the decreasing solubility with temperature to form a second phase.

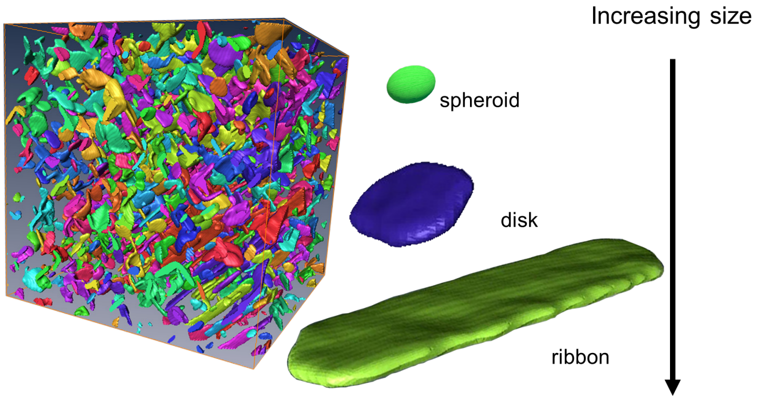

Figure 3.5: A three dimensional reconstructed SEM image of a PbTe-Sb_2Te_3 section and the resulting size dependent morphologies. As the size of the precipitate increases the morphology changes from a spheroid to a disk and finally a ribbon like morphology [68].

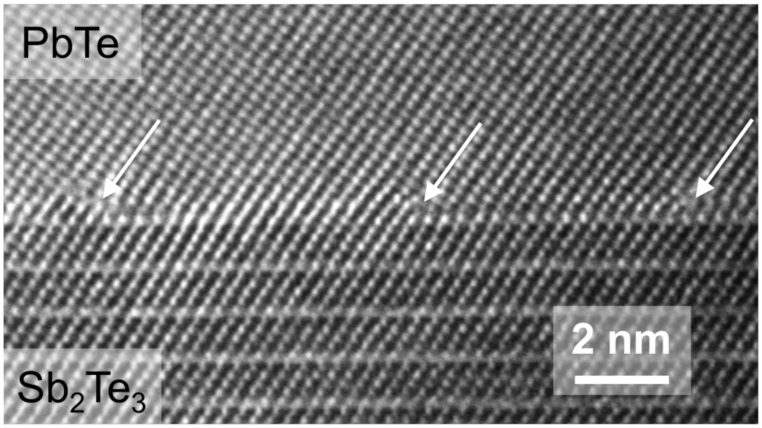

Figure 3.6: A high resolution transmission electron microscope (HRTEM) image of interfacial dislocations at the boundary of Sb_2Te_3 (bottom) in PbTe (top). The arrows indicate the location of the dislocation cores at the interface.

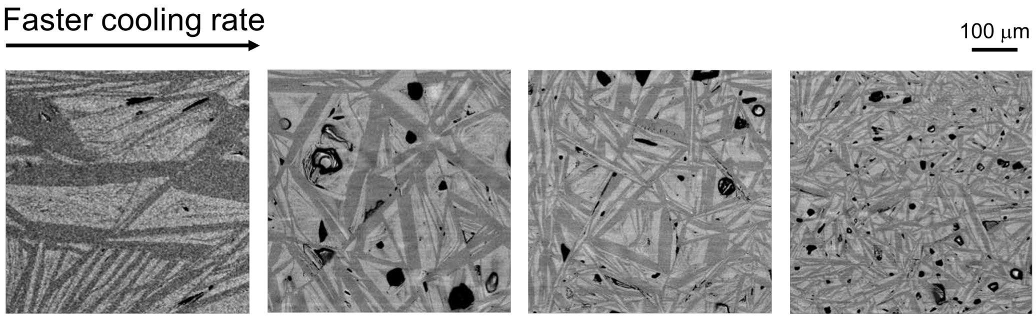

Figure 3.7: The trend of smaller structure size with increased cooling rate is seen in the solidification experiments of Ikeda involving PbTe-Sb_2Te_3 [37, 39].

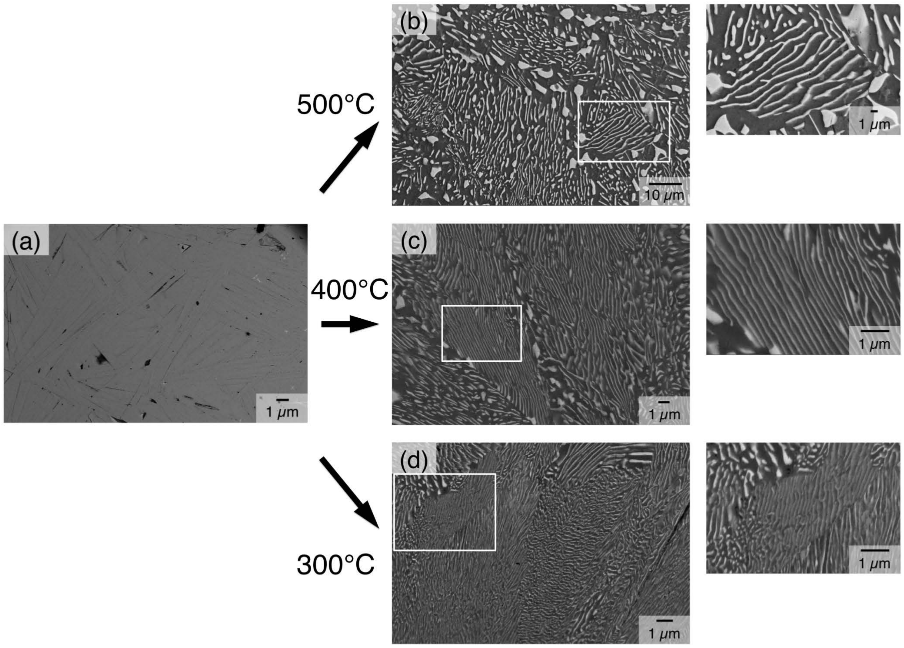

Figure 3.8: The trend of decreasing layer spacing with larger undercooling is observed in the case of the eutectoid reaction of (a) $Pb_2Sb_6Te_{11}$ to PbTe-Sb_2Te_3. The three examples annealed for equivalent time at (b) 500°C, (c) 400°C, and (d) 300°C validate the assertions of Eqn. 3.8.

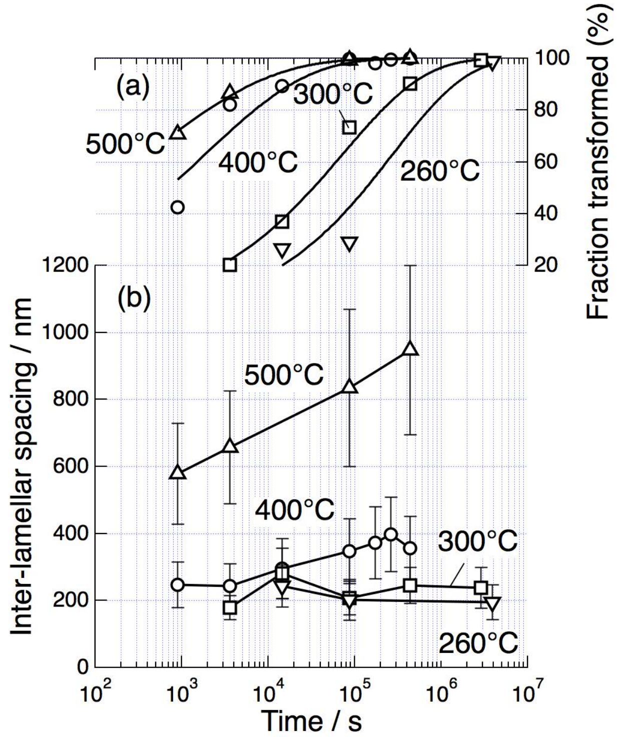

Figure 3.9: The (a) fraction transformed and (b) inter-lamellar spacing, λ, vs time for several samples of PbTe-Sb_2Te_3.[38] The discrepancy among the samples involved could potentially be remedied with the generation of a KJMA type equation (see text).

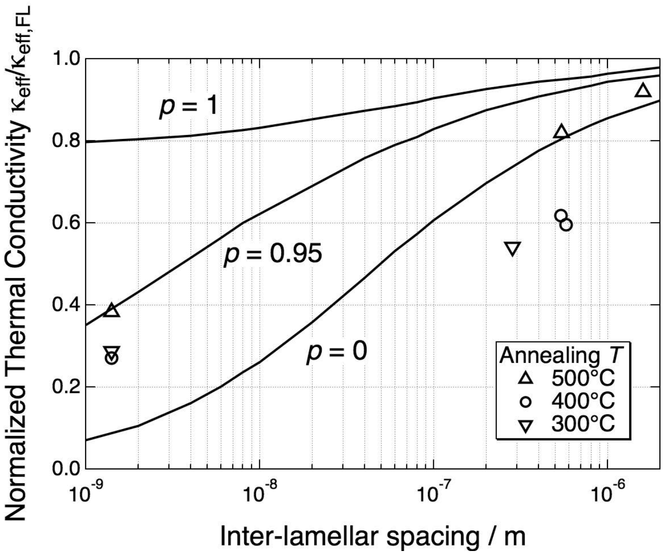

Figure 3.10: The dependence of thermal conductivity on the layer spacing in the PbTe-Sb_2Te_3 system shows a dramatic improvement when the layer spacing is minimized [99]. The values of p indicate the level of specularity with values near zero being diffuse. Figure adapted from [99].

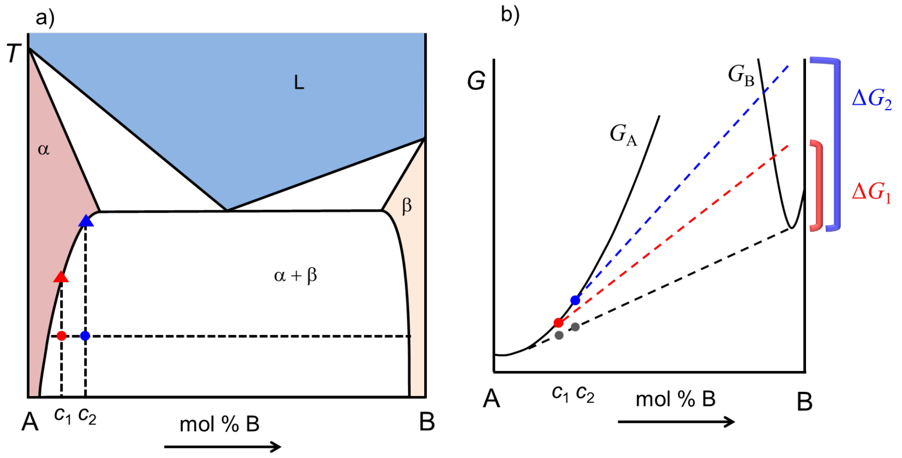

Figure 3.11: A schematic of (a) a typical binary eutectic phase diagram portraying the effects of altering the composition for a given temperature and (b) the resulting free energy curves and chemical driving force difference resulting from a change in supersaturation. A larger supersaturation will lead to a larger chemical driving force, and ultimately stronger nucleation, leading to finer microstructure formation. The red and blue triangles in (a) assist in the description of the effects seen in Fig. 3.13.

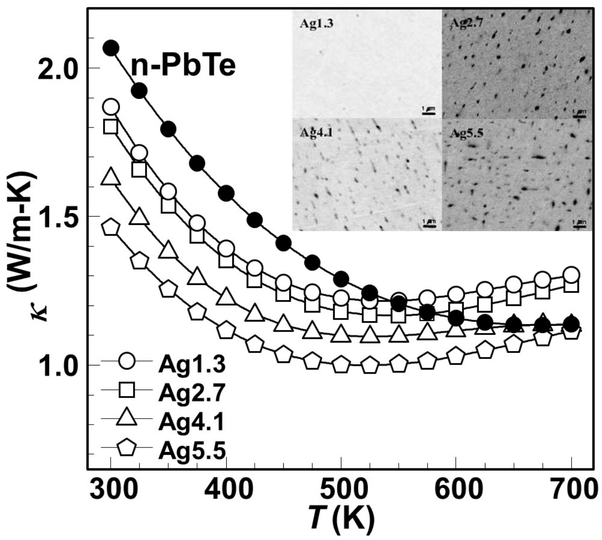

Figure 3.12: The increased supersaturation for a given temperature led to stronger nucleation, finer microstructure and eventually a lower κ in the case of PbTe-Ag_2Te. Figure adapted from [10].

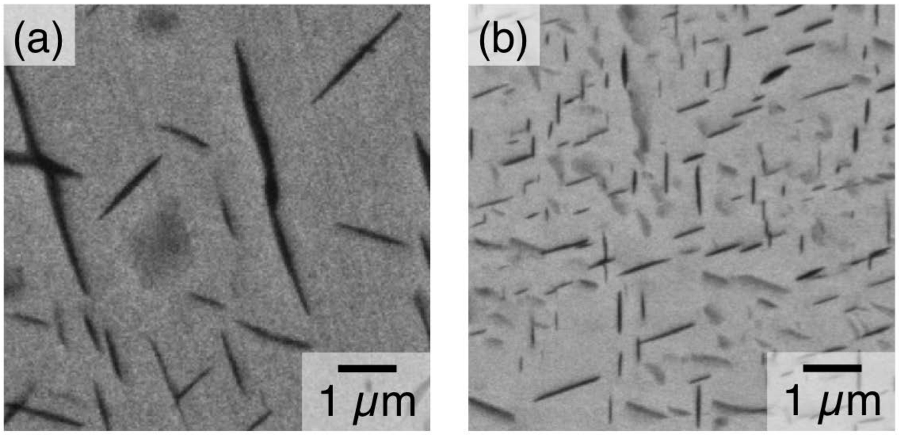

Figure 3.13: Resulting scanning electron microscope (SEM) images of two samples of PbTe-Sb_2Te_3 where (a) had a starting composition of 5.5 at.% Sb and (b) 4 at. % [11]. However, these samples were prepared by slow cooling as opposed to isothermal annealing, and the (a) 5.5 at. % sample was in the two phase region longer than the (b) 4 at. % sample (as depicted by the difference between the circles and triangles for c_1 and c_2 in Fig. 3.11a). The resulting microstructure suffered in (a) due to significant coarsening despite the higher supersaturation.

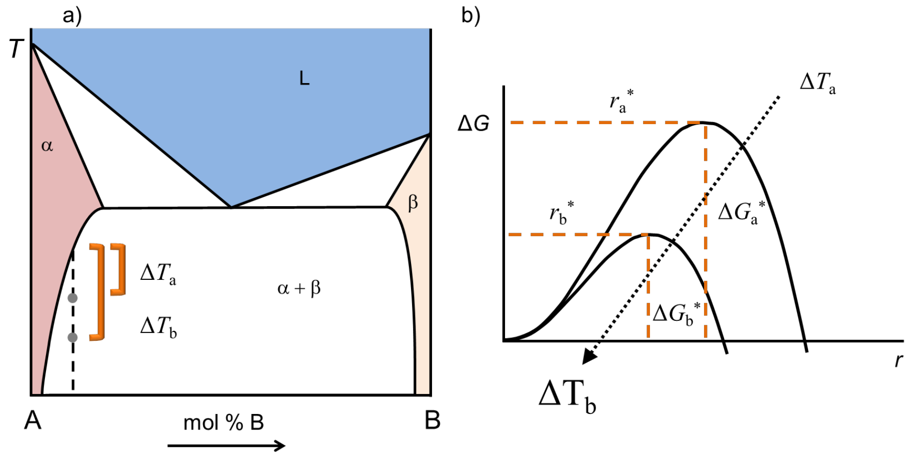

Figure 3.14: A schematic of (a) a typical binary eutectic phase diagram portraying the effects of altering the temperature for a given composition and (b) the resulting free energy vs. critical radius curves for the two examples. For a larger undercooling, there is a decreased critical nucleus size for continued nucleation, therefore an increase in nucleation events leads to finer microstructure.

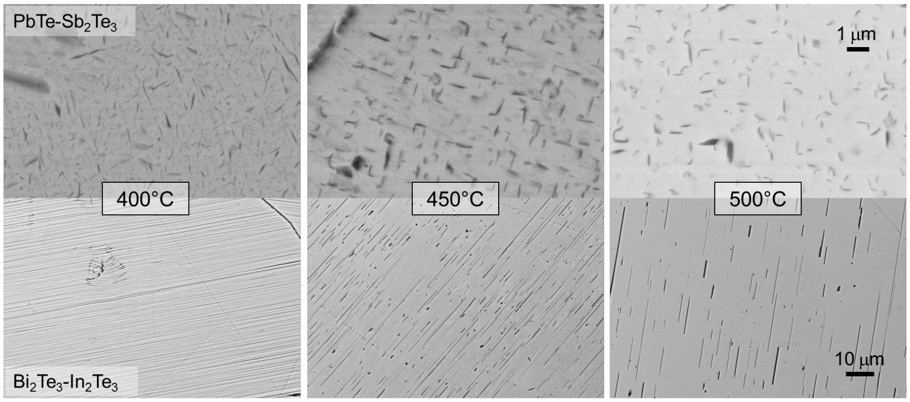

Figure 3.15: Resulting electron micrographs of the PbTe-Sb_2Te_3 [11] (top row) and Bi_2Te_3-In_2Te_3 [24] (bottom row) systems showcasing the effects of increased undercooling for a given composition. In both cases, the microstructure becomes finer for a larger undercooling.

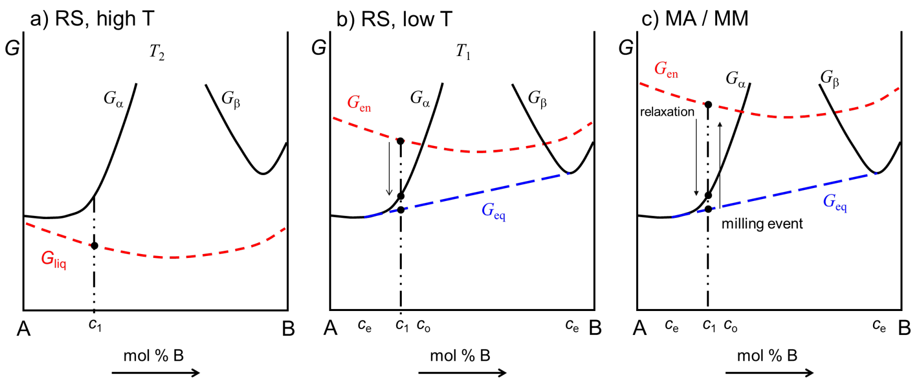

Figure 3.16: A schematic displaying two different non-equilibrium processing routes. In (a) rapid solidification (RS) the system is initially in the liquid state, but (b) immediately upon quenching at a rapid enough rate the system can be stabilized in a non-equilibrium position on the free energy curve. However, in (c) mechanical alloying or mechanical milling (MA/MM) the system is gradually brought up to this energized state, and is often an easier route on account of the lower processing temperature than in RS.

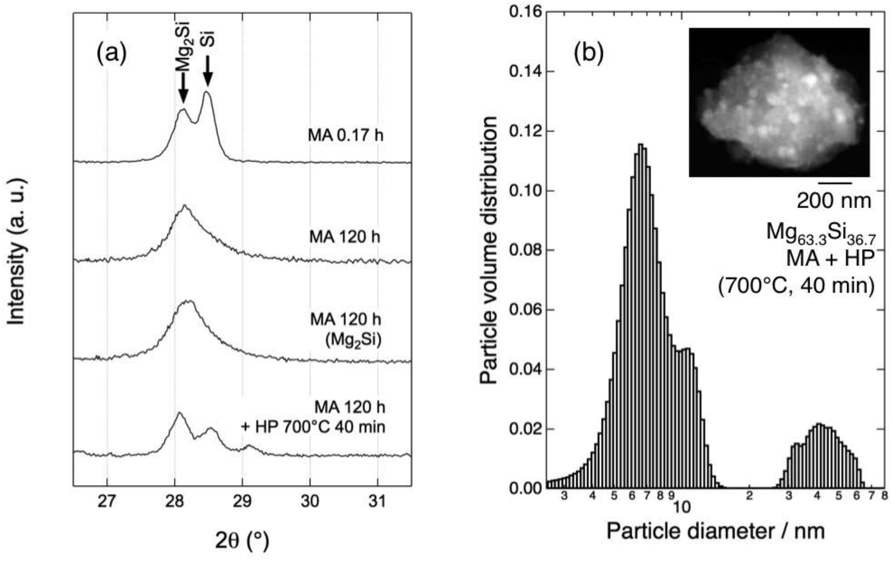

Figure 3.17: The results of (a) X-ray diffraction (XRD) and (b) small angle X-ray scattering (SAXS) measurements for $Mg_{63.3}Si_{36.7}$ prepared by non-equilibrium processing. Inset in (b) is a transmission electron microscope (TEM) image of the resulting Si microstructure. The XRD patterns indicate that the additional Si either dissolves in the Mg_2Si or becomes sufficiently small to broaden the two peaks into one. The resulting TEM and SAXS measurements quantitatively showcase the extremely fine scale in which the Si particles form during the consolidation step. Figure adapted from [112].

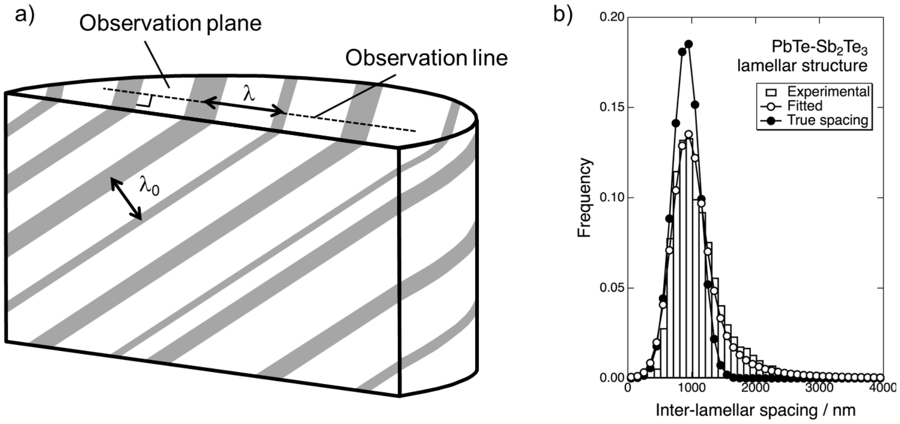

Figure 3.18: a) Schematic showing the difference in observed lamellar spacing and true lamellar spacing for a sample in which the observation plane is not perpendicular to the lamellae. b) A plot of the lamellar spacing distribution experimentally determined from SEM micrographs, fit by Eqns. 3.14-3.15, and calculated using a Gaussian distribution based on the parameters $\lambda_{0,\text{avg}}$ and σ. Figure adapted from [100].

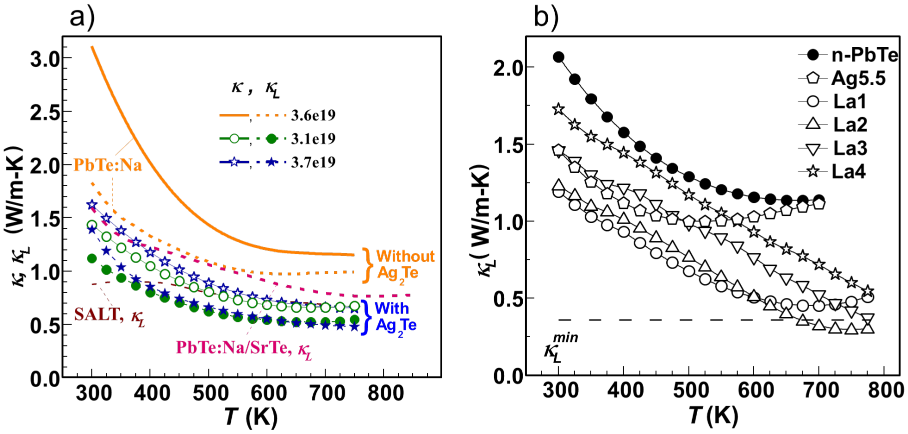

Figure 3.19: Thermal conductivity data comparing the benefits of the nanostructruing in PbTe composites of Ag_2Te for (a) Na [9] and (b) La [10] additions.

Chapter 4

Zone melting

4.1 Introduction

On account of the anisotropy in Bi_2Te_3 and its related compounds, it is necessary to synthesize the materials in such a way that the properties can be discerned based on crystallographic direction. Typically, the usual method to synthesize anisotropic materials is to grow single crystalline samples and determine the fundamental material properties in each unique crystallographic direction [13]. This is often done via bulk directional solidification like the Bridgmann method [20], in which the entire ingot is melted and then solidified (frozen) from one end to the other (Fig. 4.1a-b). This is a great way to understand the fundamental properties of pure materials, however, if one desires to extrinsically dope a material to further explore the electronic and thermal properties, as is necessary in functional thermoelectric material design, it is often difficult to grow homogeneous oriented crystals due to solute segregation.

However, there exists a technique called zone melting (ZM) that allows for the growth of single crystal or oriented material while controlling the solute content [21]. The difference between these techniques is that in zone melting, only a controlled portion of the material is molten at any given time, even at the outset (Fig. 4.1c). Zone melting has been used in the past to grow oriented and single crystalline Bi_2Te_3, however in later works it is often referred to as the traveling heater method (THM) [19].

4.2 Zone melting theory

Before discussing zone melting it is important to understand the process of bulk solidification or freezing. An important parameter in both growth processes (ZM vs bulk) is the equilibrium distribution coefficient (k_0). This is the ratio of the solid composition (C_s) to that of the liquid composition (C_l). As can be seen in Fig. 4.2, $k_0 < 1$ in systems in which the addition of solute decreases the melting temperature (such as in eutectic systems), and $k_0 > 1$ in systems where the addition in-

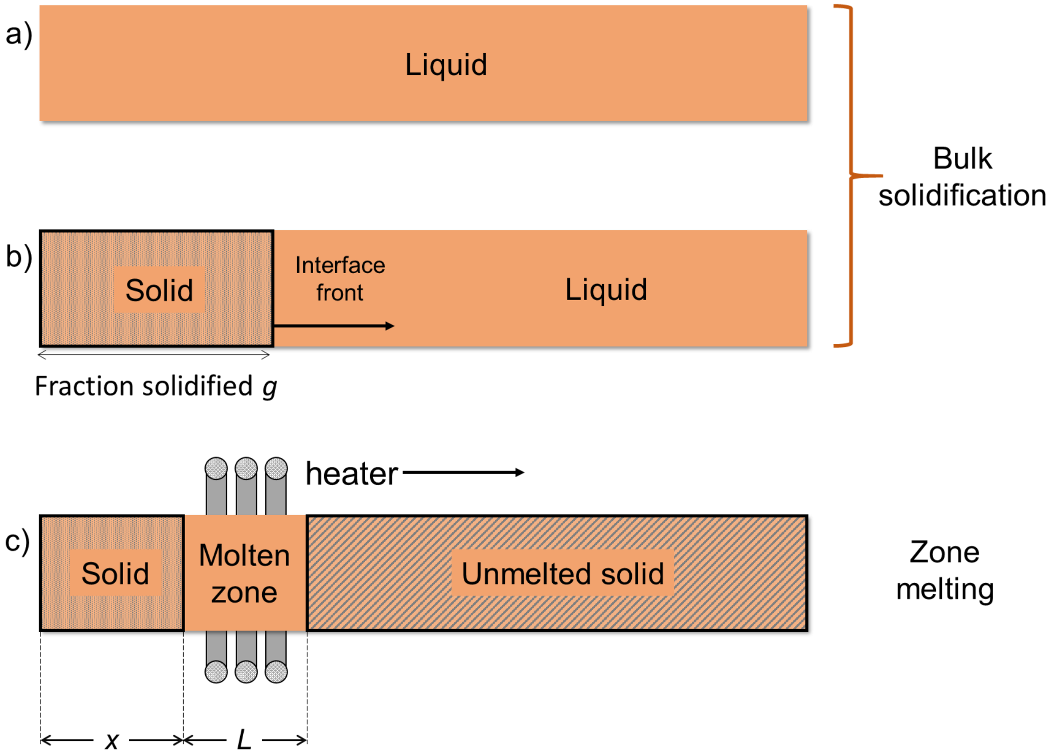

Figure 4.1: A schematic laying out the physical differences between bulk normal solidification and zone melting. In bulk solidification, (a) the entire material is initially in a molten state, while upon solidification of one end (b) the solid-liquid interface traverses the ingot until it is solidified. In zone melting (c) only a portion of the material is molten at any given time.

creases the melting temperature (peritectic systems). Often the equilibrium distribution coefficient is not the actual value found in practice, rather there is an effective distribution coefficient, however for the materials in this thesis the equilibrium distribution coefficient is a viable approximation for growth purposes.

For the sake of brevity, the rest of this discussion will be based on $k_0 < 1$. Solute distribution in bulk directional solidification depends on the rate of freezing, i.e. the solidification rate, and the degree of mixing in the liquid. The most extreme form of bulk solidification is often called equilibrium solidification, or freezing. This occurs in instances where the temperature and concentration gradients are negligibly small. This means that the solidification rate is extremely low in order to permit diffusion processes in the solid and liquid and also to eliminate concentration gradients. Under this circumstance, the concentration of solute is always k_0 times the liquid concentration. Therefore, because solidification rejects solute to the liquid, the concentrations travel along the solidus and liquidus continuously increasing the solute concentration in both, and the last bit of liquid freezes when it reaches the composition of C_l/k_0 (Fig. 4.2). It is important to note that after the last of the liquid has frozen, the entire solidified material will be at composition C_l due to the allowed freezing, and there will be no segregation in the solid because of the complete diffusion in the solid. This

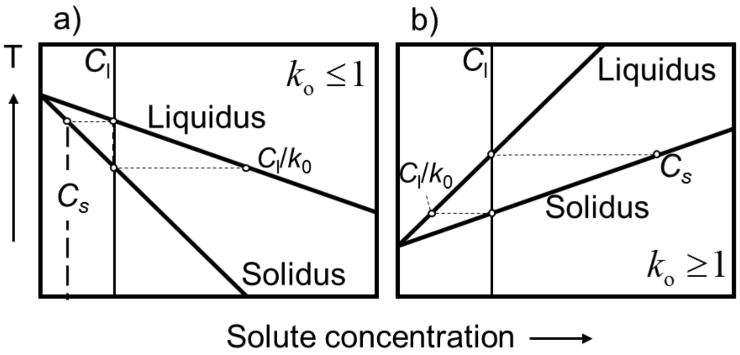

Figure 4.2: The implications of a material system in which (a) $k_0 < 1$ (eutectic) and (b) $k_0 > 1$ (peritectic).

type of solidification is rarely found in practice due to the diffusion rates in the solid being too low to eliminate concentration gradients.

A more realistic form of bulk solidification, referred to as normal solidification or freezing, is where there is either no diffusion in the solid, a uniform concentration in the liquid, or both. Maximum segregation during bulk solidification occurs when both of these cases exist simultaneously. Typically there is little control of the diffusion in the solid during solidification, however the concentration of the liquid can be controlled by forced mixing in the liquid by either mechanical or inductive means.

The degree of segregation during normal solidification can be described analytically by:

$$C = k_0 C_0 \left(1 - g\right)^{k_0 - 1}, \tag{4.1}$$

where C is the concentration in the solid at a given point, C_0 in this case is the original liquid composition (C_l), k_0 is the distribution coefficient, and g is the fraction of the material that has been solidified. This is derived very simply in Appendix A. If C_l is taken to be unity, different degrees of segregation can be plotted with varying values of k_0. Also, since segregation causes the composition to change, often the value of k_0 is not constant, but is still a good approximation.

Fig. 4.3a is a plot of concentration vs fraction solidified for values of k_0 ranging from 0.1-5.0 for bulk solidification. As can be seen, there is a significant amount of segregation throughout the entirety of an ingot prepared by normal solidification. In fact, at only one point in any of the curves presented is the solidified composition equal to that of the starting liquid composition. If the desire is to functionally grade or purify a material, this is a route to do so, especially if $|(1 - k_0)| \geq 5$. However, if a homogeneous concentration profile is desired, this is not the optimal synthesis route to achieve that goal.

Zone melting can also be used to purify materials, and in fact is the accepted reason the technique was invented [129]; under these conditions it's referred to as zone refining. However, the technique was originally discovered by the same researcher much earlier in his career as a means to evenly

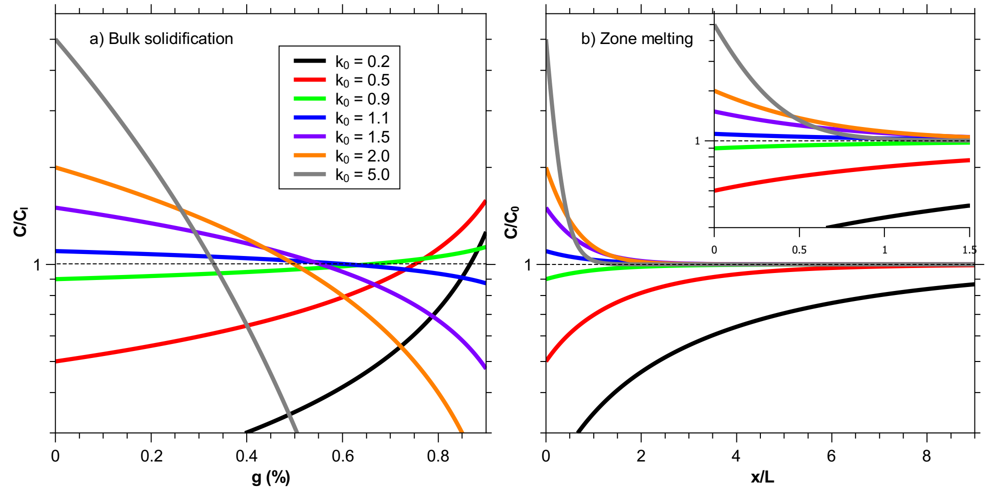

Figure 4.3: The resulting solute concentration differences between (a) bulk normal solidification and (b) zone melting. There is a significant difference between homogeneity in (a) bulk normal solidification than that of (b) zone melting. For all values of the equilibrium distribution coefficient shown in (a), there is only one point throughout the entire ingot that the solute concentration reverts back to C_0. However, it is much more apparent that a homogeneous solute distribution is possible in zone melting, especially for systems in which $k_0 > 5$. In fact, as can be seen in the inset of (b) $k_0 > 1$ results in $C/C_0 \sim 1$ within 1 - 2 zone lengths.

distribute solute throughout a solidified ingot [129]. It is the later technique called zone leveling which is of interest to synthesize homogeneously doped samples of Bi_2Te_3.

This branch of zone melting can be understood in a similar fashion to that of bulk normal solidification. As follows from Fig. 4.1c, one end of the material of length L is initially melted and then that molten zone travels from one end of the material to the other. The first solid to freeze at $x = 0$ has the concentration $k_0 C_l$ (C_s) (Fig. 4.2a). The solid phase rejects solute to the liquid while the molten zone travels through the ingot, continuously increasing the solute content in the molten zone until the molten concentration reaches C_l/k_0, at which point the molten zone saturates with solute. Once saturated, the concentration of solids entering and leaving the zone are the same which results in no change in the solute concentration. Once the molten zone reaches the opposite end of the sample, normal bulk solidification will dictate the concentration profile in the last zone length of the material, similar to Fig. 4.5a.

Analagous to Eqn. 4.1, there is a similar expression to describe the distribution of solute in a single pass of a molten zone throughout a material:

$$C/C_0 = 1 - (1 - k_0)\, e^{-k_0 x/L}, \tag{4.2}$$

where C and k_0 are the same as in Eqn. 4.1, while C_0 x and L are the original solute concentration, the distance from the point of first solidification and the length of the molten zone (Fig. 4.1c).

Using Eqn. 4.2 it is possible to plot the concentration vs. distance along the material as solidified, discretized by the zone length. As can be seen in Fig. 4.3, there is a marked difference for the single pass zone leveled materials than in the ones grown via normal solidification. Here, it can be seen that not only is it possible to obtain the mean concentration of solute, but for values of $k_0 > 0.5$ it is possible to obtain a significant amount of homogeneous material, provided that the ingot is sufficiently long.

4.2.1 Zone leveling techniques

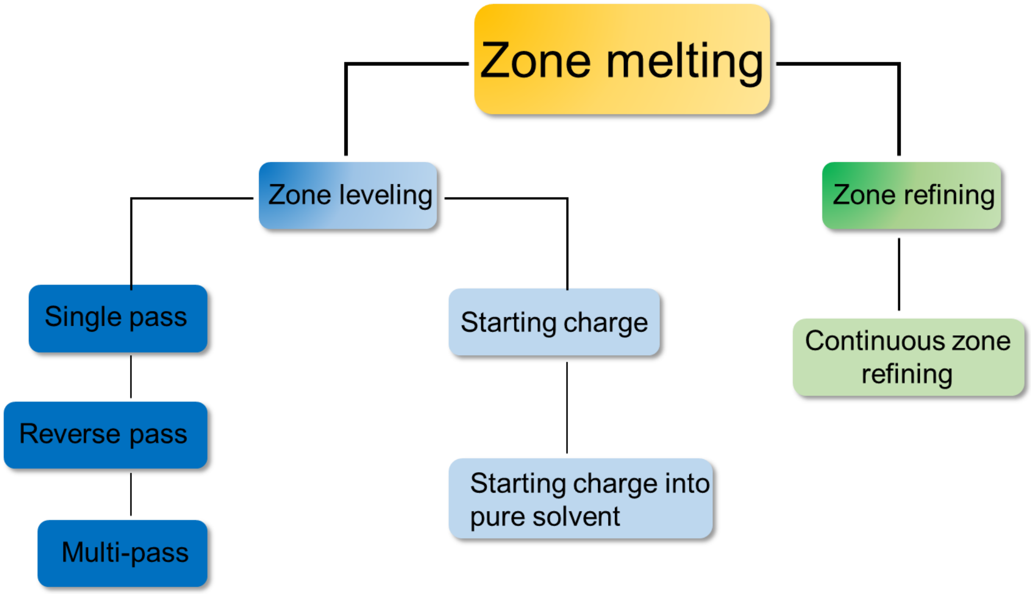

Figure 4.4: The hierarchy of techniques often invoked in discussing zone melting. The right tree is comprised of zone refining techniques, where the goal is to remove solute. Since increasing the number of passes is vital to increasing sample purity, continuous zone refining is often used which incorporates additional heating sources so the material has multiple molten zones at a given time [130]. The left tree lists the techniques pertinent to solute distribution. The first order parameter to decide which zone leveling technique to use is often k_0, however second order parameters such as material length, and growth time also impact which technique is used.

Previously the discussion of zone melting was limited to zone melting of a single pass, often called single pass zone leveling. Yet, there are still ways to improve the solute homogeneity in zone melted samples. Fig. 4.4 is a hierarchical chart of several of the different methods that can be used to either distribute (zone leveling) or remove solute (zone refining) in materials.

Depending on the value of k_0, a single pass (Fig. 4.5a) may prove insufficient to grow enough material in a desired period of time. Another rather simple way to improve homogeneity is by reversing the direction of the molten zone at the end of the first leveling. This is referred to as reverse pass zone leveling and effectively doubles the ingot length. For example, if the initial ingot is

5 zones long, then including a reverse pass would make it 10 zones long. As can be seen in Fig. 4.3a and 4.5b this vastly improves the homogeneity throughout the sample, except in the final molten zone. One can continue to reverse the direction of the molten zone for any number of passes until the necessary length to achieve homogeneity. Zone leveling of this method is a form of multi-pass zone leveling.

Multi-pass zone leveling, while effective, often involves long growth times to achieve homogeneity due to the often necessary slow growth rates (1-3 mm/hr in Bi_2Te_3 and its alloys). This can be improved by changing the concentration of the initial zone, which is known as starting charge zone leveling. If the material is synthesized in such a way that the starting zone is the composition of the liquidus related to the *desired* solidus, while every zone afterward maintains the desired solidus composition, the delay to reach the desired composition is significantly decreased (Fig. 4.5c), except for the first and last molten zones.

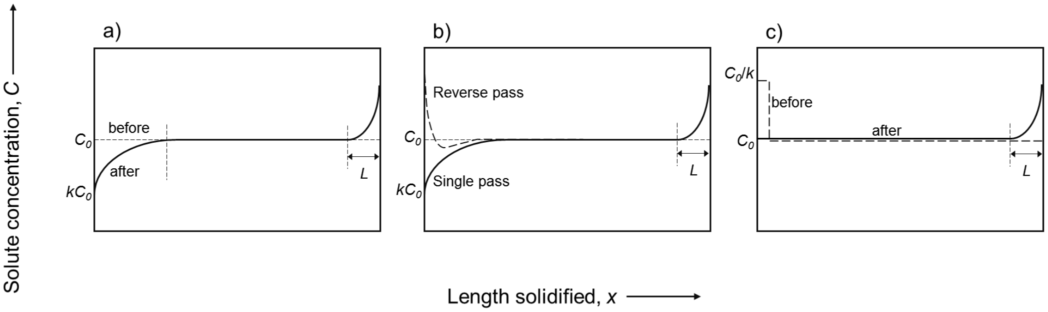

Figure 4.5: Schematics of solute concentration profiles for (a) single pass, (b) repeated pass and (c) starting charge zone melting.

This technique can be applied to compositions in which the distribution coefficient is extremely small ($k_0 \leq 0.1$) as well. However, in situations in which k_0 is this low, the initial zone should contain the solute, while the rest of the material should be void of any solute. For values of $k_0 \leq 0.01$ this technique maintains the solute concentration within 10 % of the desired concentration in ten zone lengths [21].

As mentioned previously, zone melting is not limited to controlling the solute distribution such that it is homogeneous either. Zone melting can be used to remove unwanted solute that acts as an impurity, which is often referred to as zone refining (right side of Fig. 4.4). The classic example of this is the zone refining of silicon and germanium to make transistors [129].

4.3 Zone melting of pertinent materials

Values of k_0 for materials of interest in this work range from less than one (eutectic In_2Te_3-Bi_2Te_3 system) to greater than one (solid solution Bi_2Te_3-Bi_2Se_3 system). For the indium alloyed and

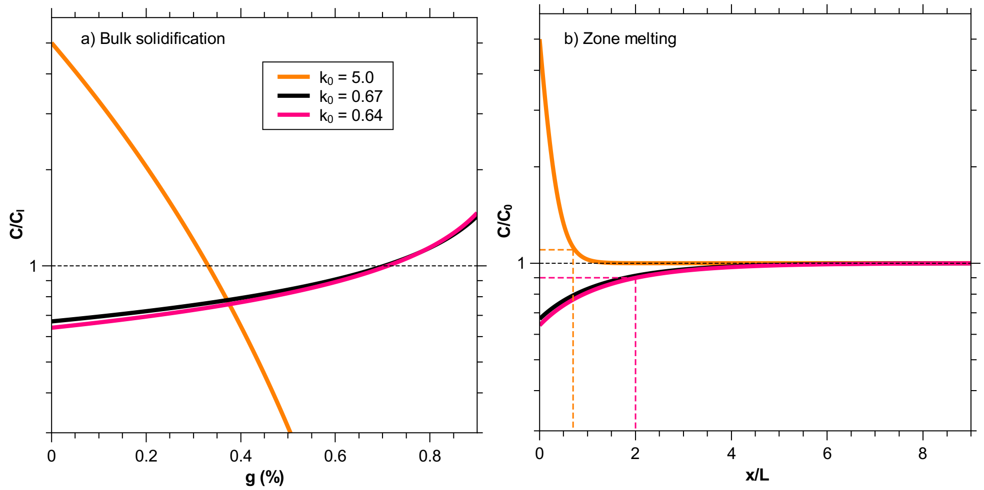

Figure 4.6: Similar to Fig. 4.3, however this explicitly portrays the solute concentration profiles in (a) bulk solidified and (b) zone melted materials for values of k for the indium (4 at. % and 7 at. %) and selenium (5 at. %) alloys of Bi_2Te_3. The distribution coefficients for the strictly iodine doped samples is very nearly unity and does not vary significantly from C_l. However, it is apparent that for the materials measured in this thesis, a minimum of two zone lengths is necessary to be within 10% of the initial solute concentration (dashed lines).

composite samples, the distribution coefficient ranges between 0.64-0.67, and based on Fig. 4.6 it is apparent that zone melting is a more appropriate synthesis procedure with regard to sample homogeneity than normal solidification. However, single pass zone leveling is insufficient to create homogeneous samples of In alloyed Bi_2Te_3 due to the solute equilibration occurring after 4-5 zone lengths.

The values of k_0 for the indium samples was low enough to warrant the use of the starting charge zone leveling method. In this instance, the initial charge was synthesized such that it was the equilibrium liquidus concentration in accordance with the necessary solidus composition that would result in the desired microstructure formation (based on Fig. 5.1). The indium based samples were grown with a zone length of ∼15 mm and the ingots were typically ∼4.5 zones long, which is sufficient for solute equilibration. Due to the fact that the iodine content is so low, it was assumed to have a negligible effect on the growth of the materials.

The strictly iodine doped Bi_2Te_3 samples are much simpler to think about from a zone melting perspective. Due to the very small quantities of iodine used to dope the materials ($\leq$0.2 at.%), the change in concentration is near zero, which leaves the distribution coefficient to be very nearly unity, and equilibration occurs in or very close to the first zone (Fig. 4.3b).

4.3.1 Constitutional supercooling in zone melting

At the solidification front, there is a very important phenomenon that can significantly limit the rate at which crystals may be grown via zone melting. During crystal growth (either ZM or freezing) as the solid phase rejects solute to the liquid, it does not do so in an infinitesimally small volume, and in this finite volume a concentration gradient exists. In the case of a $k < 1$ material system, the rejection of the solute will lower the liquid temperature in the vicinity of the solid liquid interface. This results in a lowering of the temperature of the liquid at the interface than the liquidus temperature of the rest of the molten zone (or remaining liquid in bulk solidification), and this is known as constitutional supercooling [54, 56].

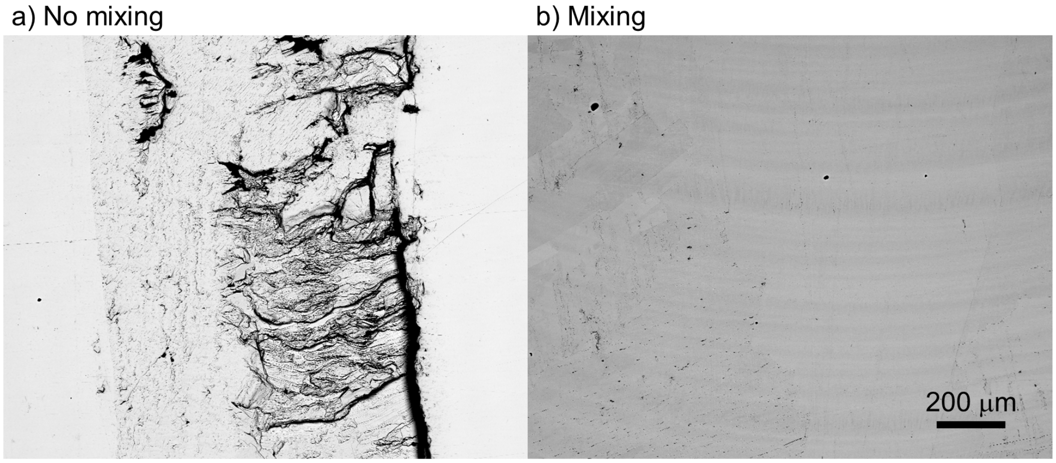

Figure 4.7: A backscattered electron image (BEI) of indium alloyed Bi_2Te_3 (7 at. % In) zone melted with (a) no mixing and (b) mixing of the liquid in the molten zone. In both cases, the growth rate (1 mm/hr) and the heating method (induction) were the same, however the mixing was suppressed in (a) by the use of a nickel susceptor.

This type of undercooling can lead to variations in microstructure, and in the specific case of indium alloyed Bi_2Te_3, it results in significant void formation at the center of the grown ingot. As can be seen in Fig. 4.7, 7 at. % In Bi_2Te_3 was zone melted with and without the use of a susceptor to block the induction furnace's magnetic field. From Fig. 4.6a it is possible to see the results of constitutional supercooling on the resulting shielded sample. Due to the active cooling on the outside of the ampoule during zone melting, the outside edge (nearest the ampoule wall) solidifies first, which dictates that the outside portion of the solidifying front rejects solute first. This indicates that the material will concentrically solidify from the outside in, and upon contracting due to the solidification, will leave an empty volume at the center of the material, which is the last to solidify.

In the case of a zone melting furnace that does not allow for mixing of the molten zone, constitutional supercooling can be avoided by adhering to equation 3.2. However, the growth rate can be increased significantly if mixing in the liquid state is possible, thus eliminating the concentration gradients. As can be seen in Fig. 4.6b, the same composition and growth rate results in completely dense material that can be utilized confidently.

Chapter 5

Microstructure formation and control in bismuth telluride

Reproduced with permission from *Acta Materialia* **60**, 4461-4467 (2012).

5.1 Introduction

To make efficient thermoelectric materials, it is necessary to optimize the dimensionless figure of merit (zT) [131]. However, when optimizing the transport properties that make up zT, including the Seebeck coefficient, S, electrical conductivity, σ, and both the electrical and lattice components of the thermal conductivity, κ_e and κ_l ($zT = \frac{S^2\sigma}{\kappa_e+\kappa_l}T$), often this proves to be quite difficult due to the coupling of these transport properties [131, 132]. While it is clear that electrons affect every aspect of zT, there has been a recent effort to reduce the lattice thermal conductivity in the field via bulk nanostructuring using a number of methods [78, 30, 79]. The reduction is believed to occur due to the boundary scattering at the interfaces of the two materials, where orientation and surface roughness play very important roles [76]. Also, it is important to reduce the heat transport due to phonons, while not severely affecting the mobility of electrons in the material. Therefore, a sensical design is to start with a material system that already has an appealing power factor ($S^2\sigma$), but also a thermal conductivity that is above the expected minimum [133]. In this case, we focus on the classic room temperature thermoelectric material Bi_2Te_3, typically used in solid state refrigeration, but also in low temperature waste heat recovery.

In past works, it was thought that the only significant κ_l reductions were due to structures that were on the order of a few nanometers [79, 8, 134, 135] in thickness and spacing. However, recently there has been evidence that one can achieve reductions in κ_l for structures that are significantly larger (∼100-1000 nm) [76, 10, 99, 9, 77, 136]. This is believed to be due to the frequency dependence of the parameters that make up the lattice thermal conductivity, specifically in this case the phonon mean free path. Therefore, rather than gauge the ability to reduce κ_l by a single structure size scale, it is probable that having distributions in both thickness and spacing corresponding to the spectrum of mean free paths has the potential to enhance zT through significant reductions to κ_l via increased boundary scattering.

To reduce κ_l in this study, we employ a thermodynamically driven nucleation and growth end member precipitation method where we exploit the solubility dependence on temperature (Fig 5.1) to reduce the phonon mean free paths for thermoelectric applications. Studies of nanocomposite structure formation via phase transformations are limited [137] and prior work in this material system has focused mainly on the maximum solubility of In in Bi_2Te_3 [138, 139]. However there has been little work examining the solubility below the eutectic temperature, specifically in establishing the solvus line. In an attempt to ultimately control the microstructure for thermoelectric applications, this study investigates the phase diagram below the eutectic temperature as well as establishes a synthesis regime for equilibrium composite formation intended for thermoelectric applications.

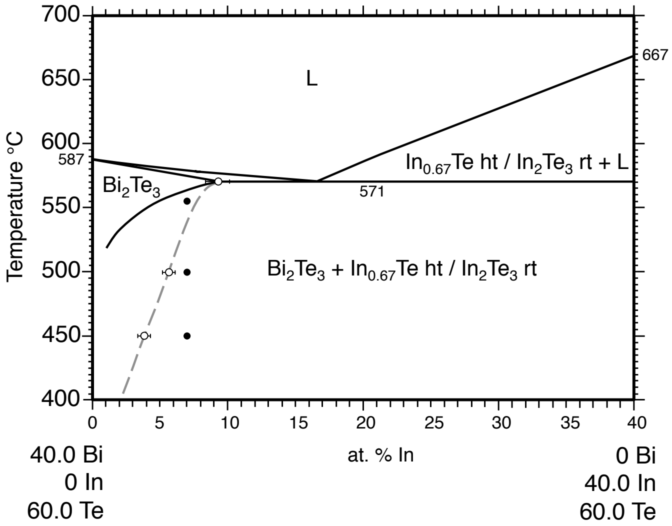

Figure 5.1: The pseudo-binary phase diagram of the Bi_2Te_3-In_2Te_3 system [138]. Displayed are the compositions and temperatures for the isothermal annealing stages (filled circle) for homogenization and precipitation. Also shown is the expected solvus line (dashed) and solubilities (open circle) based on experimental results.

5.2 Experimental

Stoichiometric amounts of Bi, Te, and In were weighed out in order to attain a composition of $(Bi_{1-x}In_x)_2Te_3$ with $x = 0.175$ (7 at% In). The starting elements were then placed in amorphous silica ampoules and vacuum sealed to a pressure of $\sim 10^{-5}$ Torr. The samples were then placed in a vertical tube furnace and melted well above the melting temperature of both Bi_2Te_3 and In_2Te_3, in this case 800°C (Fig. 5.1a) and water quenched. The resulting ingot was then annealed in the solid solution region at 555°C for 96 hours and water quenched again. Finally, the ingot was annealed in the lower temperature two phase region at either 500°C or 450°C for 72 hours in order to exploit the decrease in solubility of In_2Te_3 with temperature.

Upon completing the synthesis, the ingots were cut longitudinally for microscopic examination. The resulting face was polished with SiC paper ranging in grit ratings from #240-#800, then polished with 3 μm, 1 μm, and 0.3 μm Al_2O_3 particles, and a final polishing with colloidal silica (0.05 μm) particles was used for nanostructure observations. A field emission scanning electron microscope (Zeiss LEO 1550 VP) with a backscattered electron and secondary electron detector with an accelerating voltage of 20 kV was used to make the observations. Image analysis was done using image processing software (Imagej) to first convert to binary images and collect thickness and spacing data.

The crystal orientation relationships were established via electron backscatter diffraction (EBSD; HKL Technology, Inc.), again, with an operating voltage of 20 kV. The sample was tilted 70° with respect to the horizontal axis in the microscope in order to properly collect EBSD data. Backscatter patterns were collected and analyzed using the software package provided by Channel5^{TM} (HKL Technology, Inc.). In doing the analysis, crystallographic information for both tetradymite structured Bi_2Te_3 (rhombohedral crystal with space group $R\overline{3}m$) [14] and cubic ZnS structured In_2Te_3 (cubic crystal with space group $F\overline{4}3m$) [140] were used. Chemical analysis was done using energy dispersive x-ray spectroscopy (EDS) and the INCA software package was used for spectra collection and data analysis. Also, it should be noted that when EDS was done on precipitates in this study, the spatial resolution is ~1 μm, so only precipitates that were a minimum of 1 μm in thickness were used for these measurements.

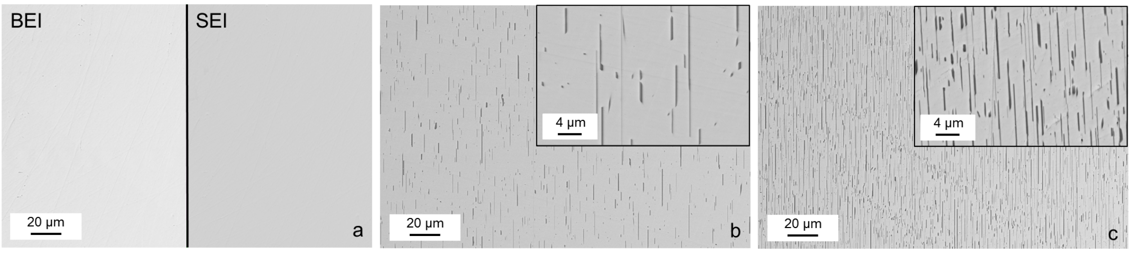

Figure 5.2: Scanning electron microscopy (SEM) images of synthesis route and resulting composite consisting of the Bi_2Te_3 matrix with embedded In_2Te_3 precipitates (7 at. % In) when annealed at 555°C for 96 hours and water quenched (a), annealed at 500°C for 72 hours (b), annealed for 450°C for 72 hours (c), both with inset high magnification image of structures formed during annealing.

5.3 Results and Discussion

SEM images were taken of each sample after the homogenization and precipitation steps in order to quantify the extent to which homogenization and precipitation of the samples had occurred (Fig. 5.2). After each step, both a backscattered electron image (BEI) and a secondary electron image (SEI) were taken in order to see the contrast from the differing Z values with the backscattered detector and then to prove that the contrast seen in the backscattered images were not surface artifacts, i.e., cracks or holes.

Fig. 5.2a contains both a split BEI and SEI displaying the homogeneous solid solution of 7 at. % In in Bi_2Te_3. According to the reported phase diagram [138] (Fig. 5.1a), however, this composition and temperature is not in the single-phase solid-solution region. Moreover, there is no phase diagram information below ~520°C in the literature. Overlaid is a more probable solvus line based on isothermal annealing experiments done in this study. As can be seen in Fig. 5.2b-5.2c, precipitation occurs when the temperature of the ingot is decreased to either 500°C or 450°C due to the decrease in solubility of In with decreasing temperature. Crystals were grown via directional solidification using the Bridgman method in order to determine the maximum solubility, and isothermal annealing techniques were used to determine the solubility at 500°C and 450°C.

In order to determine the degree to which nucleation is complete, it is necessary to know the diffusion length, $\sqrt{Dt}$, where D is the diffusion coefficient and t is the time scale involved. Due to the soft impingement effect [67], it is expected that when the precipitate spacing is less than $\sqrt{Dt}$, nucleation, from a number density standpoint, is expected to be complete. Unfortunately there is no diffusion information for either In or In_2Te_3 in Bi_2Te_3. However, as can be seen in Table 5.1, there exists diffusion coefficient information, both parallel and perpendicular to the basal planes, for several transition metals in Bi_2Te_3.

Based on this information, it is expected that 72 hours is adequate time to reach complete nucleation as the largest spacing between precipitates is ~20 μm and the characteristic diffusion lengths for the transition metals, as seen in Table 5.1, considered are all considerably larger than this spacing. The compositions of the homogeneous, precipitated, and Bridgman grown samples can be seen in Table 5.3. The composition of the homogeneous sample (555°C) was nominal with respect to the calculated value and the high (~9 at. %) solubility of In in Bi_2Te_3 was verified.

Ideally the matrix and precipitate compositions would be corroborated using the equilibrium phase diagram, Fig. 5.1a, however, that is not possible in this case because the phase diagram has never been examined at temperatures below 520°C. In order to prove that the precipitation occurs due to the decrease in the solubility with decreasing temperature, the solvus line was investigated. The same criterion for the diffusion length can also be used to determine when the equilibrium composition has been reached, and in the case of a 72 hour annealed sample, it would seem the

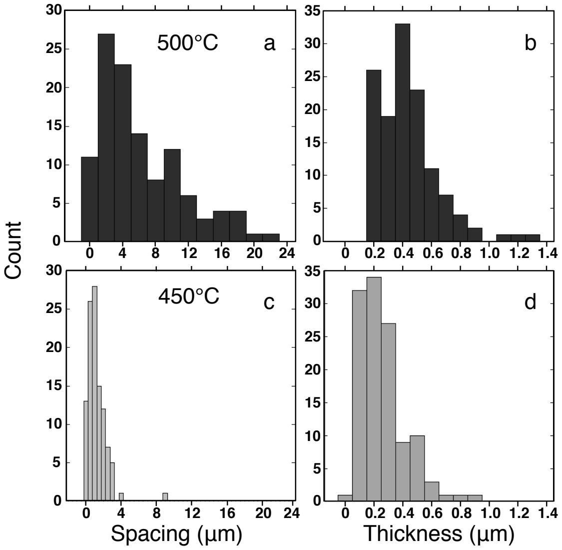

Figure 5.3: The resulting histogram data for both the 500°C sample (a) and (b) and 450°C sample (c) and (d) precipitate spacings and thicknesses after annealing for 72 hours.

Table 5.1: Diffusion coefficients of transition metals in Bi_2Te_3 at $T = 450°C$ for $t = 72$ hr from the literature. For the cases of Ag and Au, the extremities of the expressions for $D_\parallel$ and $D_\perp$ were calculated, and the average of those values was taken and used in the comparison. Diffusion coefficients for the 500°C samples are larger, and therefore are not displayed here.

Metal	Ref	$\sqrt{D_\parallel t}$ (cm)	$\sqrt{D_\perp t}$ (cm)
Cu	[141]	5.59	0.22
Ag	[142]	1.05	0.023
Au	[143]	3.61	0.36

equilibrium composition had been attained for both samples.

However, the samples were annealed at their respective isotherms for an additional 72 hours, the composition was examined, and the resulting composition did not change. This gives qualitative insight into the location of the solvus line shown on the phase diagram generated in Fig. 5.1a. The resulting matrix composition of In is ∼4 at. % at 450°C and increases with increasing temperature up to ∼9 at. % at the eutectic temperature, as was determined by the Bridgman method (Table 5.3). From a compositional stability standpoint, it would appear that precipitation is complete within the time scale of 72 hours.

There still exists the issue of coarsening with regard to prolonged annealing. Since the compositional stability seems stable after an additional 72 hours at both 500°C and 450°C, it is expected to be minimal. Also, the application temperature for this material is significantly lower (maximum ∼250°C) than both precipitation isotherms, so it is unlikely that once the composite is formed would it see an environment well above room temperature.

Table 5.2: Volume fraction data for 7 at. % In Bi_2Te_3 samples at both 500°C and 450°C, as calculated by applying the lever rule to the EDS measurements and from the average thickness and spacing data $\left(X_{vol} = \frac{thickness}{spacing}\right)$.

Method	500°C (%)	450°C (%)
Lever Rule	4.1 ± 3.6	9.6 ± 3.2
X_{vol}	6.8 ± 1.5	17.7 ± 7.4

The three dimensional morphology has not yet been determined, but based on the 2D SEM images taken, it appears as if the precipitates form long and straight plate-like or possibly ribbon-like structures [68]. As can be seen in Fig. 5.2b-5.2c and Fig. 5.3, the observed thickness of the In_2Te_3 precipitates in both samples ranges an order of magnitude from ~100-1000 nm. Even though the distribution of thicknesses spans a similar length scale, the peak thickness value for the 450°C sample is ~50% less (200 nm) than that of the 500°C sample (400 nm). The spacing of precipitates however, is significantly different in each sample as the 500°C sample ranges from ~1-20 μm, while the 450°C sample ranges from 0.1-5 μm.

The decrease in thickness and spacing with decreasing temperature can be qualitatively described from classic nucleation theory of diffusive phase transformations [67]. The critical free energy barrier, ΔF^*, to permit nucleation for spherical nuclei is expressed by:

$$\Delta F^* = \frac{16}{3}\frac{\pi\sigma^3}{\left(\Delta F_c + \Delta F_E\right)^2}, \tag{5.1}$$

where σ is the interfacial energy, ΔF_c is the chemical driving force, and ΔF_E is the strain energy. The critical free energy dictates the rate, I, of nuclei formation represented by:

$$I = NA^*\nu \exp\left(-\frac{\Delta F_A + \Delta F^*}{k_B T}\right), \tag{5.2}$$

where N is the number of atomic sites per volume, A^* is the number of sites on the surface of the critical nucleus, ν is the atomic vibration frequency, and ΔF_A is the activation energy of atomic jumps across the interface. The lower annealing temperature acts to increase the supercooling and supersaturation, ultimately increasing the chemical driving force for nucleation. The large chemical driving force decreases the critical energy for nucleation (Eqn. 5.1) which increases the nucleation rate (Eqn. 5.2) and tends to result in a larger number density of precipitates. The higher supersaturation is indicated by an increased volume fraction with decreasing temperature, as seen in Table 5.2.

The volume fraction of In_2Te_3 for the 7 at. % In Bi_2Te_3 samples at both 500°C and 450°C can be calculated by applying the lever rule to the EDS measurements and the average thicknesses and spacings $\left(X_{vol} = \frac{thickness}{spacing}\right)$ from Figure 5.3. The large uncertainties in the lever rule calculations stem from the error in chemical compositions by EDS (Table 5.3). The error in thickness and spacing due to the SEM parameters when imaging, and also due to the image analysis of the resulting micrographs are difficult to quantify, but an estimated error of ±20% on the average thickness and spacing for each temperature was used.

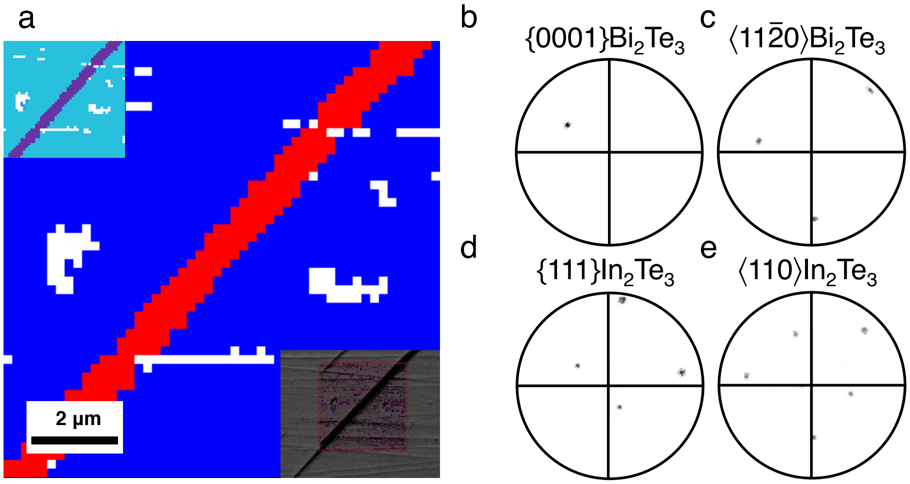

Figure 5.4: Electron backscatter diffraction (EBSD) results for the Bi_2Te_3-In_2Te_3 composite. Inset to the top left of (a) is the resulting map based on the Euler angle of the incident diffraction, indicating the precipitate is a single grain. Also inset in (a) is an SEM image of the actual scan, and the main image is of the resulting diffraction based on composition with the blue being Bi_2Te_3 and the red being In_2Te_3 (Color version available online). The pole figures can also be seen (b-e) indicating that the resulting diffraction is indeed $\{0001\}Bi_2Te_3 \parallel \{111\}In_2Te_3$ and consequently $\langle 11\bar{2}0\rangle$ Bi_2Te_3 $\parallel$ $\langle 110\rangle$ In_2Te_3, thus aligning both the close-packed planes and directions.

It should be noted that these are not the true thicknesses and spacings, as the observation plane is most likely inclined relative to the direction normal to the precipitates (Fig. 5.4).These size scales make sense from a solid state reaction point of view, as the slow diffusion in the solid, compared to the diffusion in the liquid state, should allow at least one dimension of the precipitates to be small. Adding to this is the fact that the in plane and cross plane diffusion coefficients are widely different (Table 5.1). Also, the energies at the edge and broad interfaces should be different due to the difference in coherency and or atomic species involved in bonding [144]. It is due to these dependencies that a high aspect ratio should be expected in these precipitates.

In any particular grain, the structures have a mono variant orientation. As can be seen in Fig. 5.2b-5.2c, every in-grain precipitate is aligned in the same orientation, in this case the primary growth direction being vertical. This type of orientation generally stems from the minimization of strain and interfacial energies upon structure formation, which will usually have a specific set of preferred crystallographic orientations [67]. For example, in the PbTe-Ag_2Te system the precipitates align along the {100} planes in PbTe to maintain the Te sub lattice between the two crystals [73], and in PbTe-Sb_2Te_3 the crystals take on a standard FCC-HCP orientation of {111} PbTe $\parallel$ {0001}

Table 5.3: Energy dispersive x-ray spectroscopy (EDS) data for samples of interest homogenized at 555°C for 96 hours, annealed at 500°C and 450°C for 72 hours (Fig. 5.2), and also the Bridgman grown crystal. All precipitates measured in the precipitated sample had a minimum thickness of ~1 μm for accurate measurements. Likewise, matrix areas where the largest precipitate spacing occurred were utilized for the same purpose.

Sample	In (at%)	Bi (at%)	Te (at%)
Bridgman	9.0 ± 1.0	30.5 ± 0.5	60.3 ± 0.6
555°C	7.6 ± 1.0	32.7 ± 0.4	59.8 ± 0.8
500°C Mat.	5.9 ± 1.4	32.0 ± 2.0	63.0 ± 2.0
450°C Mat.	4.4 ± 1.2	35.3 ± 1.4	60.2 ± 1.0
500°C Precip.	35.0 ± 6.0	4.0 ± 6.0	61.0 ± 1.0
450°C Precip.	32.0 ± 2.0	4.0 ± 0.9	59.7 ± 0.8

Sb_2Te_3, aligning the close-packed planes [12].

Similarly, in the PbTe-$PbBi_2Te_4$ system the orientation relationship is {111} PbTe ∥ {0001} $PbBi_2Te_4$ [41]. Because of the similarities in the PbTe-Sb_2Te_3 and PbTe-$PbBi_2Te_4$ systems to Bi_2Te_3-In_2Te_3, it is reasonable to expect a comparable orientation relationship, and as can be seen in Fig. 5.4, the relationship is indeed {0001} Bi_2Te_3 ∥ {111} In_2Te_3 with the habit plane of the precipitates along {0001} Bi_2Te_3. Also like the PbTe-Sb_2Te_3 [12] and PbTe-$PbBi_2Te_4$ systems [41], the close packed $\langle 11\bar{2}0\rangle$ Bi_2Te_3 ∥ $\langle 110\rangle$ In_2Te_3 directions are aligned in this study as well.

It should be noted that the exact crystal structure of In_2Te_3 at the temperatures used in this study can be one of several different forms [145, 146, 147, 148, 149, 16, 140]. In the literature, the crystal structure of In_2Te_3 is complicated, however, the one aspect past authors have been able to agree on is that the crystal structure has a Te sub-lattice for compositions in the range of 57-61% Te [145]. This Te sub-lattice takes on an FCC structure and the ordering or disordering of In and its vacancies has not been fully examined. Due to this complex metal/vacancy distribution for the possible phases of In_2Te_3, and also the residual Bi content dissolved in the material affecting the lattice parameter, EBSD results were sometimes difficult to analyze. However, due to the fact that the differing crystallographic results often stem from In ordering/disordering, it is not believed that this should affect the orientation relationship.

Since it has been established that large nanoscale structures can be formed in Bi_2Te_3, the next step would be to determine the extent to which the composite formation can affect the transport properties. If the most generic kinetic expression for thermal conductivity is used, $\kappa_l = \frac{1}{3}Cvl$ where C is the specific heat, v is the phonon velocity, and l is the mean free path, the parameter with the highest probability of reduction from the nanocomposite formation will be the mean free path. Altering C and v involves altering the phonon dispersion, which would require some type of bond strength alteration [76, 150]. Also, due to the inherent anisotropy in the crystal structure of Bi_2Te_3 it will also be necessary to determine which direction will give the best materials efficiency, zT.

As far as thermal conductivity is concerned, it will be a matter of in-plane (along the major growth direction of the precipitates) or cross plane (perpendicular to the major growth direction) conductivity to consider. Due to the fact that in most high figure of merit versions of Bi_2Te_3 [151, 152, 153], the transport properties are best optimized perpendicular to the $\langle 0001 \rangle$ direction, therefore, it would be expected that the in-plane conductivity to be the parameter that will be considered. In thinking about the in-plane conductivity, calculations approximate materials as superlattices [135, 99], and in the case of the Bi_2Te_3-In_2Te_3 system this should be an adequate approximation. In these calculations, there are two main parameters which affect the resulting decrease in thermal conductivity, namely interfacial roughness, and structure periodicity.

As important as reducing κ_l is to maintain a large zT, it is just as important to disrupt the electrical material properties as little as possible. This is where having coherent matrix-precipitate interfaces with few interfacial dislocations can prove beneficial. The dislocations act as carrier scattering centers for the electrons, which decrease the electronic carrier mobility. Yet, the coherency strain can enhance the phonon scattering, which can further reduce κ_l [154].

An indication that nanostructuring Bi_2Te_3 with In_2Te_3 will maintain its high electron mobility [16, 19, 151, 152] is the fact that due to the strict orientation of the precipitates in the matrix, the interfaces are expected to be either coherent or semi-coherent. The main coherency indicator is the low lattice mismatch. Dislocation density behaves proportionally to lattice mismatch [155, 71], so the smaller the mismatch the lower the dislocation density and more coherent the interface. In the case of Bi_2Te_3-In_2Te_3 the lattice mismatch as calculated by $\epsilon = \left[\frac{a_h\sqrt{2}}{a_c} - 1\right]$ where ϵ is the mismatch percent and $a_h = 4.395Å$ [14] and $a_c = 6.158Å$ [145] are the lattice parameters of the hexagonal and cubic crystals, is only $\sim$1%.

From data according to the literature, In is not expected to be a strong dopant in Bi_2Te_3 [156, 157, 158]. Despite the fact that at high concentrations ($\sim$4 at. %) the conductivity type changes from p-type to n-type, the Hall coefficient remains less than unity for concentrations up to the solubility limit of $\sim$10 at. % [157], so it would be expected that this composite could be doped either n-type or p-type using traditional dopants (such as Sb and Se). However, due to the anisotropy in the crystal structure, it would be necessary to at least obtain an oriented polycrystalline sample, or better yet, single crystals of the composite to truly understand the fundamentals behind the change in transport properties. Moreover, strict understanding of the pseudobinary phase diagram will be necessary before single crystal growth techniques can be utilized. Likewise, through this understanding of the equilibrium phase diagram it will be possible to finely tune the nanostructures to better suit thermoelectric applications. Studies controlling the volume fraction and number density of precipitates and also the solubilities of In for different temperatures and concentrations will need to be carried out.

5.3.1 Further examination of microstructure

The phase diagram was further explored to determine the potential control over microstructure size and spacing, while also attempting to minimize the amount of residual indium in the matrix. The results of further compositions explored and undercooling values used can be seen in Fig. 5.5. The composition was varied between 3-7 at. % indium while the precipitation temperature was varied between 400-500° C.

However, as can be seen in Fig. 5.5 it was only the 7 at. % indium composition that resulted in microstructure formation. This is most likely not a kinetic result, as the 7 at. % samples indicate that the time scale for precipitation is adequate. However, the slope of the solvus line could be steeper than is represented in Fig. 5.1. If this were the case, as the indium content is decreased the lever rule would indicate that a lower volume fraction of In_2Te_3 would form. This is expecially true in the sample with the lowest indium content.

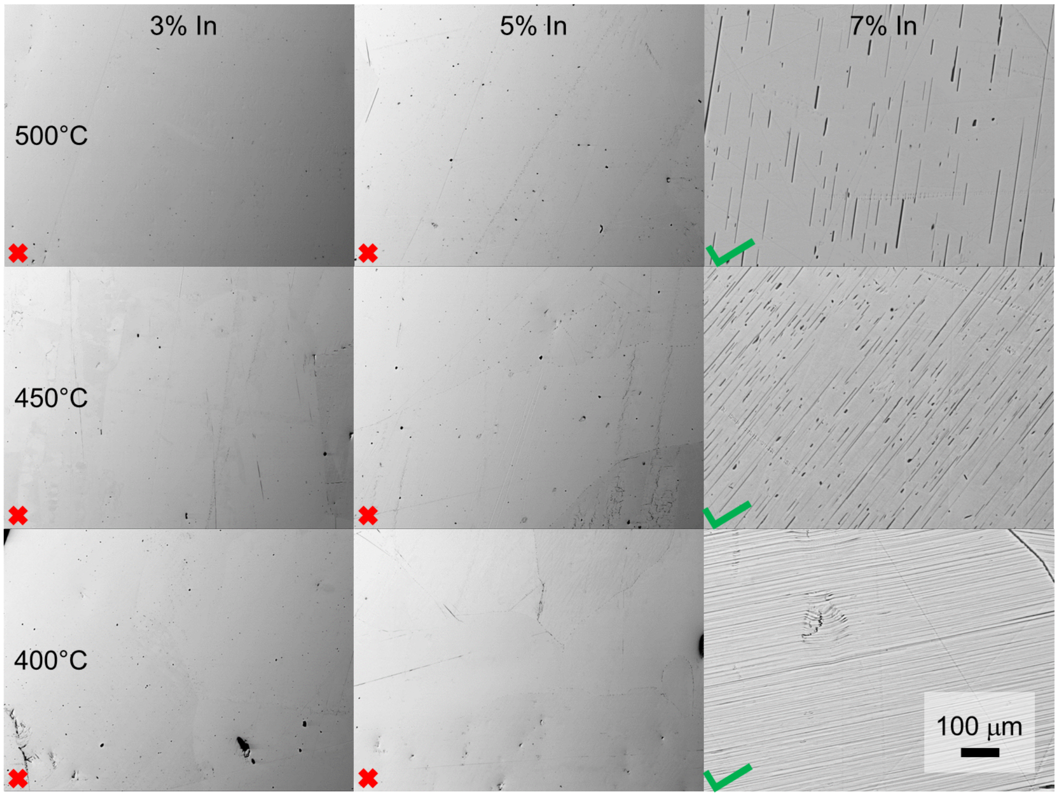

Figure 5.5: The SEM results of further examination of the phase diagram for microstructure control. The slope of the solvus line significantly limits the supersaturation based control.

With the control parameters relative to the permitted microstructure formation well understood, it was necessary to attempt to orient the material for transport measurements. Fig. 5.6 is a concatenation of several backscatter SEM images spanning the full width of a 6 mm ingot. As can be seen, there is a significant amount of orientation with respect to the grains. The crystallographic orientation can be confirmed by EBSD, as it shows that the grains throughout the ingot are oriented with the z direction perpendicular to desired direction for measurements.

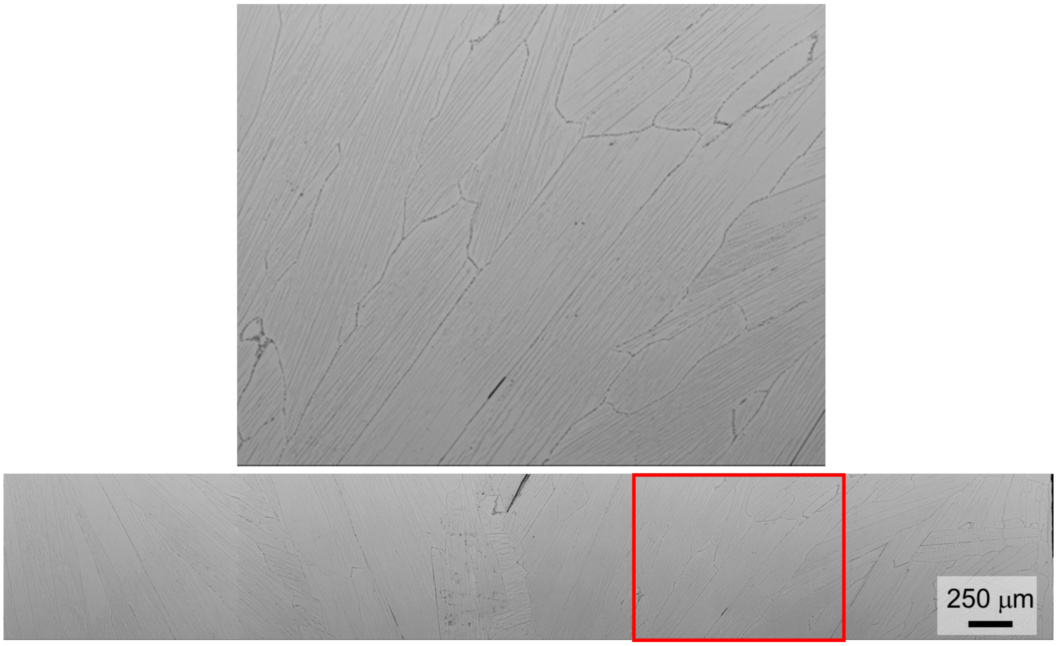

Figure 5.6: The zone leveling and annealing at 450° C showing the resulting microstructure alignment.

5.4 Conclusion

A successful synthesis regime was determined to grow highly oriented plate-like In_2Te_3 nanostructures inside bulk thermoelectric Bi_2Te_3 using a thermodynamically driven nucleation and growth technique. This technique utilized the decreasing solubility of In with decreasing temperature in Bi_2Te_3. The maximum solubility of In in Bi_2Te_3 was verified by unidirectional solidification using the Bridgman technique [20]. An experimental solvus line was determined based on isothermal annealing experiments at two temperatures (500°C & 450°C) below the eutectic temperature. The average thickness and spacing is ideal for thermal conductivity reductions necessary for efficient thermoelectric materials [9]. The orientation relationship between the two crystals aligns the close packed planes, or $\{0001\}Bi_2Te_3 \parallel \{111\}In_2Te_3$, and also the close packed directions, or $\langle 11\bar{2}0\rangle$ Bi_2Te_3 $\parallel$ $\langle 110\rangle$ In_2Te_3 with the precipitates' habit plane along $\{0001\}$ Bi_2Te_3. This system is a promising nanostructuring candidate because of the low Hall coefficient for high levels of In [157], as the Bi_2Te_3-In_2Te_3 composite should behave like an intrinsic semiconductor, with the expectation that n-type or p-type conductivity should be attainable.

Chapter 6

Transport properties of indium-alloyed and indium telluride nanostructured bismuth telluride

6.1 Introduction

It was previously determined that nucleation and growth is a successful microstructure technique that can result in enhanced thermoelectric performance [10, 9]. This work consisted of introducing Ag_2Te structures into thermoelectric PbTe. The residual silver in the PbTe matrix was found to not significantly affect the transport properties of PbTe. It was also determined that even with κ reduction for all temperatures measured, that the peak zT was not increased. Instead, zT as a function of temperature shifted left toward increasing the average efficiency. It was because of this discovery in PbTe that Bi_2Te_3 was chosen next as a candidate for κ_l reduction via microstructure formation as the peak figure of merit occurs near 300 K.

6.2 Indium-alloyed bismuth telluride

6.2.1 Doping efficiency

It would be expected that the substitution of indium into the bismuth sub-lattice would not significantly alter the number of free carriers. However, as indium replaces bismuth there is an overall decrease of charge carriers (holes) and near 2 at. % indium the conductivity type changes from p-type to n-type [157]. As the indium content is further increased, there is a similar continuation of free carrier increase. A defect model supposes that as indium is taken into the bismuth sub-lattice that anti site defects of bismuth on tellurium sites (Bi_{Te}) are suppressed, which explains the decrease

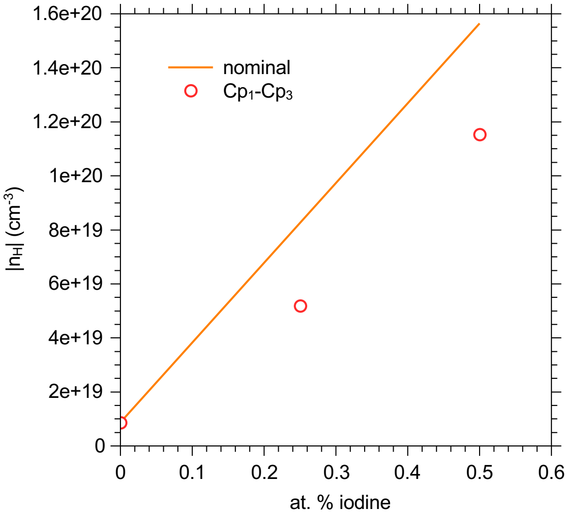

Figure 6.1: The doping efficiency of iodine in 4 at. % indium alloyed Bi_2Te_3. Based on valence charge counting, it appears that iodine is only ∼ 70 % efficient as an n-type dopant in indium alloyed Bi_2Te_3.

in carriers to a point [159, 160]. However, this would not explain why the majority carrier type not only switches, but increases with indium content. The model goes on to suggest that the indium substitution also leads to tellurium vacancies, which would add additional n-type carriers.

As mentioned previously, the addition of indium into the bismuth sub-lattice causes the conductivity to change from p-type to n-type. However, in this work the Halogen iodine was used to further control the number of carriers. As can be seen in Fig. 6.1, iodine is an effective n-type dopant in indium alloyed Bi_2Te_3. The nominal carrier concentration was determined based on valence charge counting from the undoped indium alloyed material (Cp_1). The concentration of indium in samples Cp_1 through Cp_3 matches that of the matrix of 4 at. % indium. Once the Hall carrier concentration was determined in the undoped material, a linear extrapolation based on the number of tellurium sites in the unit cell (per cm^{-3}) was utilized as the nominal doping content.

However, as can be seen in Fig. 6.1 for samples Cp_2 and Cp_3 the material is under doped based on the assumption that one iodine atom donates one electron. In fact, the doping efficiency of iodine in indium alloyed Bi_2Te_3 is ∼ 70 %. However, since the carrier concentration does not plateau between 0.25 and 0.5 at. % iodine, it is likely that the iodine substitution is not limited by its solubility but rather the location in the crystal structure.

6.2.2 Electron transport

Fig. 6.2a-d contains the Hall carrier concentration (n_H), Hall mobility (μ_H), resistivity (ρ), and Seebeck coefficient (α). The increase in $|n_H|$ at 300 K with additional iodine content is expected from 6.1. The decrease in Hall mobility is also expected with increasing carrier concentration. There

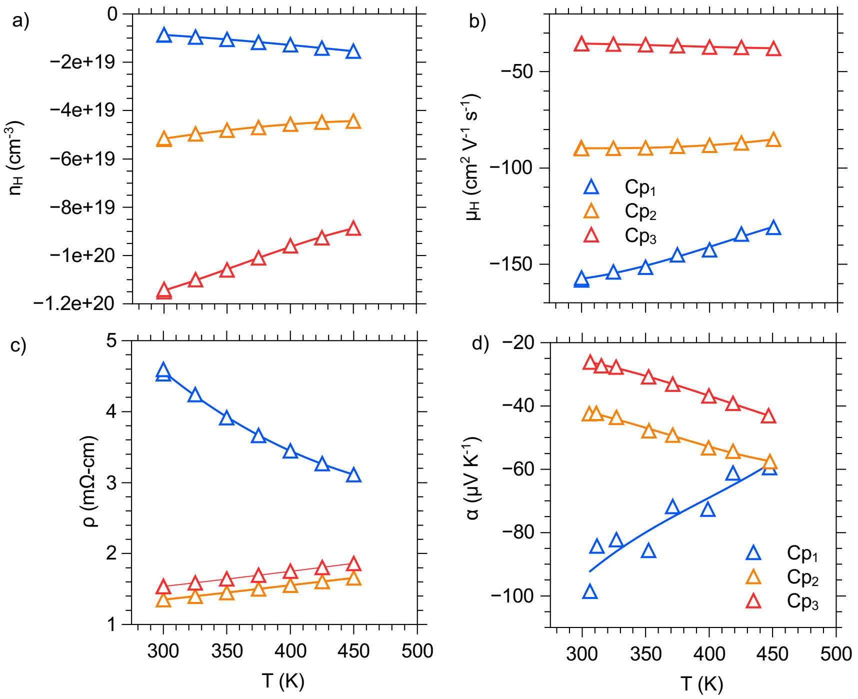

Figure 6.2: Electron transport data in 4 at. % indium alloyed Bi_2Te_3. The (a) Hall carrier concentration, n_H, (b) Hall mobility ,μ_H, (c) electrical resistivity, ρ, and (d) Seebeck coefficient, α, are all plotted vs. temperature.

is a strange temperature dependence of the transport properties that depend on the Hall coefficient R_H. In Fig. 6.2a the fact that the Hall carrier concentration decreases with temperature and the lack of temperature dependence for the Hall mobility (6.2b) is not typical among single band conducting systems. However, since the band offset in the minimum conduction band next lowest is 0.03 eV [16], the samples appear to be heavily doped enough to be influenced by two band conduction.

The change in resistivity (Fig. 6.2c) from decreasing with temperature (Cp_1) to increasing with temperature (Cp_2 and Cp_3) is due to the presence of bi-polar conduction in the former and the latter being very heavily doped.

Similar trends are found for the values of the Seebeck coefficient (Fig. 6.2d) as well. However, for the lowest carrier concentration sample (Cp_1) the maximum Seebeck value is found to be near $|\alpha| = 100\ \mu\text{V K}^{-1}$. This value is drastically reduced from what is expected from binary Bi_2Te_3 which is closer to 200 μV K^{-1} [13, 19]. The decrease in α can be explained by the change in band gap for indium alloyed Bi_2Te_3.

Optical absorption measurements were taken on undoped and indium alloyed (4 at. % indium) samples of Bi_2Te_3 to estimate the optical band gap. Fig. 6.3 is a plot of the Kubelka-Munk equation $(F(r))$ corrected for the free carrier absorption as a function of energy and fit to estimate the optical band gap of pure and 4 at. % indium alloyed (Cp_1) Bi_2Te_3. As can be seen the measured optical gap of pure Bi_2Te_3 is near 0.13 eV, while the measured optical gap of the indium alloyed sample is decreased by $\sim$ 60 % to a value of 0.08 eV.

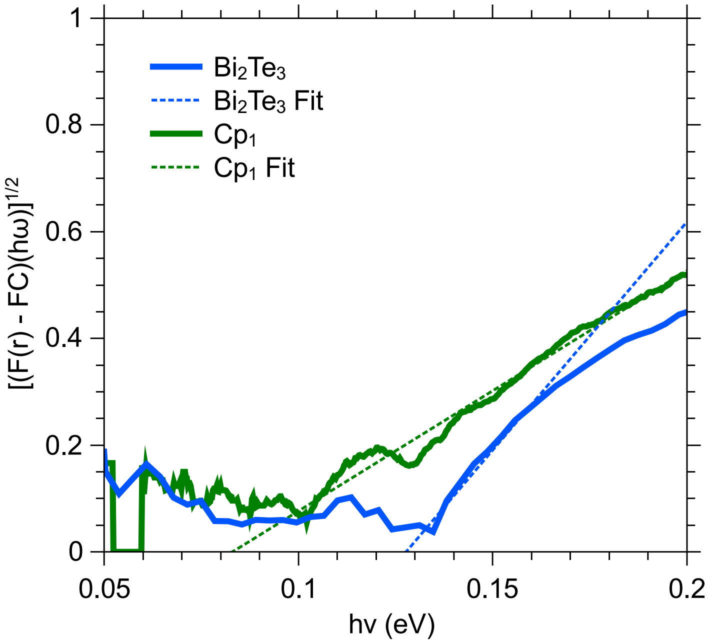

Figure 6.3: Optical absorption data in 4 at. % indium alloyed and undoped pure Bi_2Te_3. As can be seen there is a significant reduction to the optical band gap in the indium alloyed material (0.13 reduced to 0.08 eV).

Based on the results of the optical measurements, it can be concluded that the reduction in the maximum value of the Seebeck coefficient is due to the early onset of bi-polar conduction well below that of room temperature. The other two heavily doped samples have an increasing Seebeck value with temperature because of the heavy doping of iodine.

Even though it is expected that multi-band behavior is exhibited in the transport properties that depend on R_H, i.e., Hall carrier concentration and mobility (n_H, μ_H), the data was fit using a single parabolic band model. Fig. 6.4a-b is the result of the modeling, and for the heavily doped data the model predicts the α values more closely than the μ_H data. Since the Seebeck coefficient does not depend on the Hall coefficient and multi-band effects are not as sensitive as in Hall data, this is expected. The model breaks down significantly in modeling the Hall mobility, even at higher carrier concentrations (Fig. 6.4) where the effects of bi-polar conductivity are expected to lower.

6.2.3 Thermal transport

Fig. 6.5a-b are the calculated thermal conductivity from thermal diffusivity measurements, and the results of calculating the electronic portion of the thermal conductivity (κ_e) and subtracting it from the total thermal conductivity. The room temperature total thermal conductivity of the indium

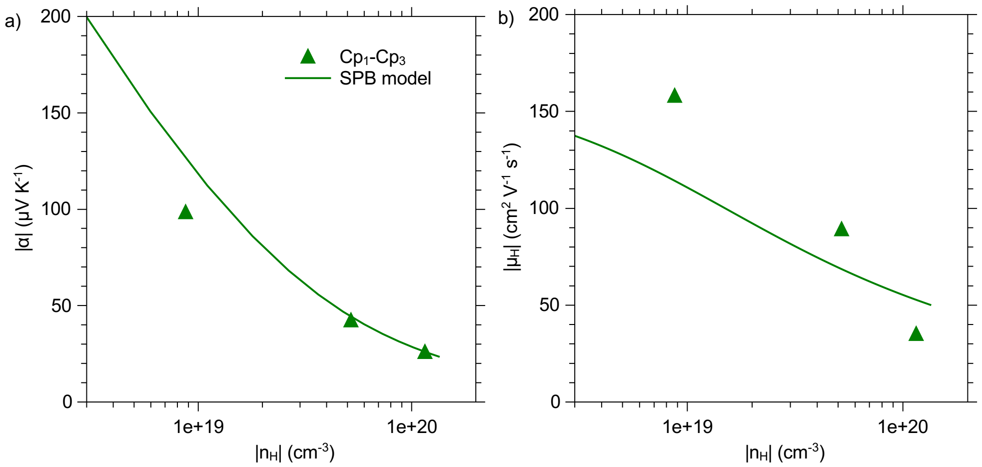

Figure 6.4: Single parabolic band modeling of the transport data in 4 at. % indium alloyed Bi_2Te_3. The absolute value of the (a) Seebeck coefficient (α) and (b) Hall mobility (μ_H) are plotted as a function of n_H. However, due to the expected multi-band effects and presence of minority carriers the single parabolic band breaks down significantly.

alloyed samples is lower than that of pure bismuth telluride, which is expected due to the additional point defect scattering.

The electronic portion of the thermal conductivity was subtracted, and the resulting values were plotted in Fig. 6.5b. Also plotted is the minimum expected lattice thermal conductivity according to Cahill's method [161]. However, the results from calculating the electronic thermal conductivity should be viewed with low confidence due to the supposed multi-band behavior of the Hall coefficient (R_H).

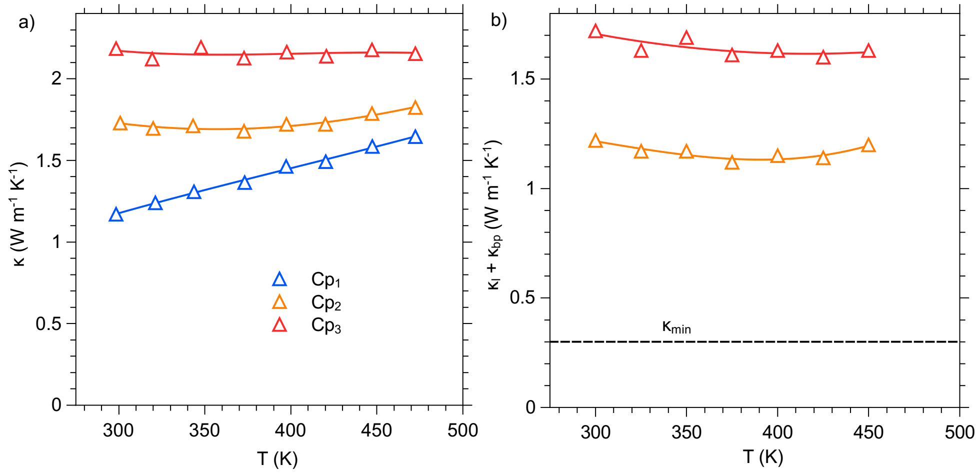

Figure 6.5: (a) Thermal transport (b) and $\kappa - \kappa_e$ calculated using the SPB model for 4 at. % indium alloyed Bi_2Te_3. Also plotted is the expected minimum lattice thermal conductivity as calculated by the Cahill method [161].

6.2.4 Figure of merit

The figure of merit of indium alloyed bismuth telluride as a function of temperature and Hall carrier concentration are plotted in Fig. 6.6a-b. It is straightforward to see the deleterious effects of indium alloying on the transport properties of Bi_2Te_3 due to the decreased band gap. The peak zT in this series of samples is 0.05, an order of magnitude smaller than typical room temperature values.

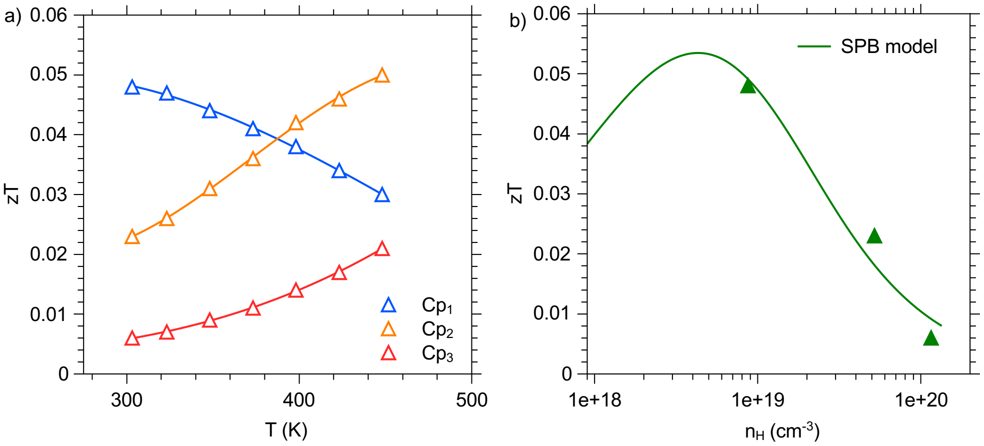

Figure 6.6: The figure of merit as a function of (a) temperature and (b) n_H as calculated by the SPB model for the 4 at. % indium alloyed Bi_2Te_3 samples.

6.3 Indium telluride structured bismuth telluride

6.3.1 Doping efficiency

The effectiveness of iodine substitution into the tellurium sub-lattices of the Bi_2Te_3-In_2Te_3 system is similar to that of indium alloyed bismuth telluride (section 6.2.1) with the nominal concentration calculated in the same fashion. Fig. 6.7 is a plot of the nominal iodine content assuming one iodine atom substitutes for one tellurium atom, donating one electron. Again, the doping efficiency of iodine is ~ 65 %.

6.3.2 Electron transport

Fig. 6.8a-d is a plot of the electron transport for the un-doped and doped composites of Bi_2Te_3-In_2Te_3. The behavior is similar to that of indium alloyed material, again showing similarly unusual behavior in the Hall dependent transport data.

The modeling done in this study is again done assuming single parabolic conduction, however, it is not expected to accurately predict the transport data due to alterations to the band structure as a result of indium substitution.

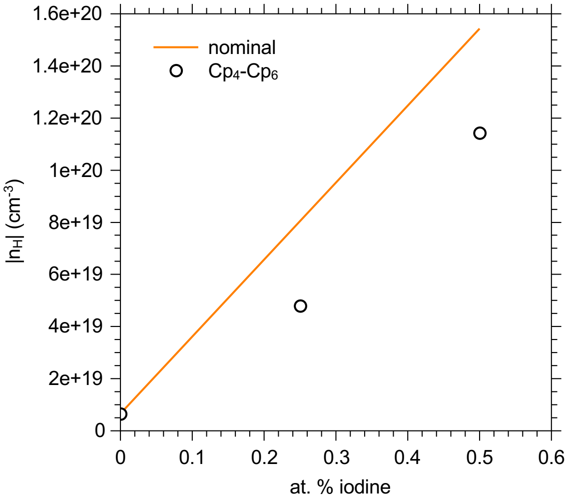

Figure 6.7: Doping efficiency of iodine in In_2Te_3 structured Bi_2Te_3. In a similar fashion to that of the alloyed samples, the doping efficiency is ~ 70 %.

6.3.3 Thermal transport

The total thermal conductivity of the Bi_2Te_3-In_2Te_3 composites is plotted in Fig. 6.10a-b. It is important to note the differences between the thermal transport data in Fig. 6.5a and here (6.10a), as the samples are similarly doped. Thus, any difference in the values would result from the presence of the deliberate microstructure. However, the room temperature values of the total thermal conductivity are the same for the alloy and composite material. However, at higher carrier concentrations the thermal conductivity in the nanostructured material has a lower thermal conductivity. While the results of the calculated values of $\kappa_l + \kappa_{bp}$ are only approximate due to the nature of the electron transport in this system, the general trend of an overall reduction in the expected lattice portion of the thermal conductivity is found.

6.3.4 Figure of merit

The resulting zT of the In_2Te_3-Bi_2Te_3 composites in this work can be seen in Fig. 6.11a-b. The maximum zT obtained is in the iodine doped sample Cp_5 at 475 K. However, the maximum room temperature peak zT belongs to the undoped sample (Cp_4). Unfortunately, these values are more than an order of magnitude less than would be expected from optimizing the carrier concentration in Bi_2Te_3.

6.4 Conclusion

This work was inspired by successful nanostructure formation of Ag_2Te inside thermoelectric PbTe [9, 10]. A similar nucleation and growth microstructure formation technique was instituted and suc-

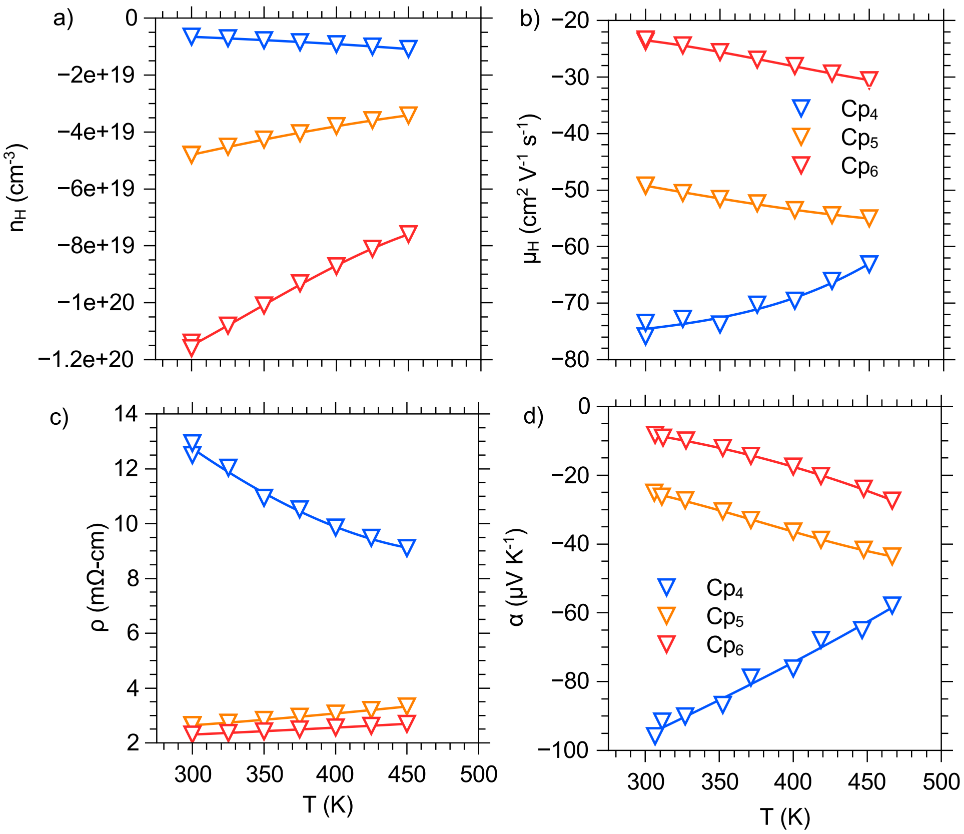

Figure 6.8: Electron transport data in In_2Te_3-Bi_2Te_3 composites. The (a) Hall carrier concentration, n_H, (b) Hall mobility ,μ_H, (c) electrical resistivity, ρ, and (d) Seebeck coefficient, α, are all plotted vs. temperature.

cessful In_2Te_3 structures were found in Bi_2Te_3, and thermal conductivity reduction was obtained. However, thermal conductivity reduction is not the complete story as carrier concentration optimization is necessary to prove the effectiveness of the thermal conductivity reduction.

Since nucleation and growth is dictated by the solvus line of the phase diagram, there will be some residual impurity atom dissolved into the matrix. In the case of nanostructured In_2Te_3-Bi_2Te_3 there was an overall residual indium content of 4 at. % in the matrix. Therefore, it was necessary to examine the transport properties of both 4 at. % indium alloyed Bi_2Te_3 and the nanostructured material.

Unfortunately, the residual indium content in the material proved to decrease the band gap, which ultimately decreased the temperature onset of bi-polar conduction, which is known to negatively effect transport for thermoelectricity. While this work rules out indium, or specifically In_2Te_3, as an effective second phase to reduce the lattice thermal conductivity, it does not rule out other candidates that would need to less significantly alter the band structure.

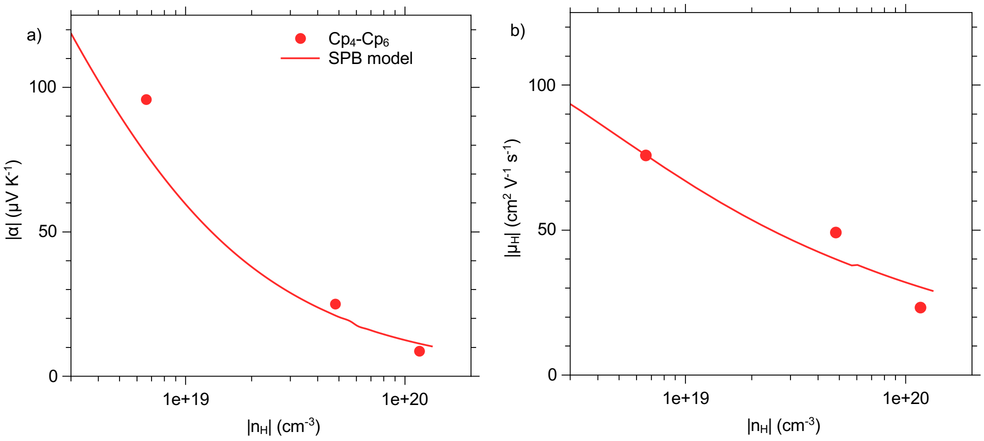

Figure 6.9: SPB modeling of the transport data in In_2Te_3-Bi_2Te_3 composites. The absolute value of the (a) Seebeck coefficient (α) and (b) Hall mobility (μ_H) are plotted as a function of n_H. However, due to the expected multi-band effects and presence of minority carriers the single parabolic band breaks down significantly.

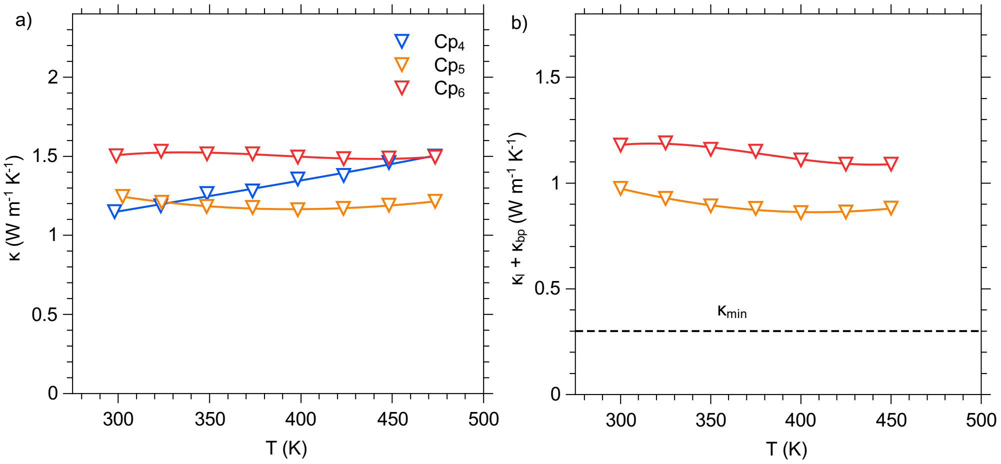

Figure 6.10: (a) Thermal transport (b) and $\kappa - \kappa_e$ calculated using the SPB model for In_2Te_3-Bi_2Te_3 composites. Also plotted is the expected minimum lattice thermal conductivity as calculated by the Cahill method [161].

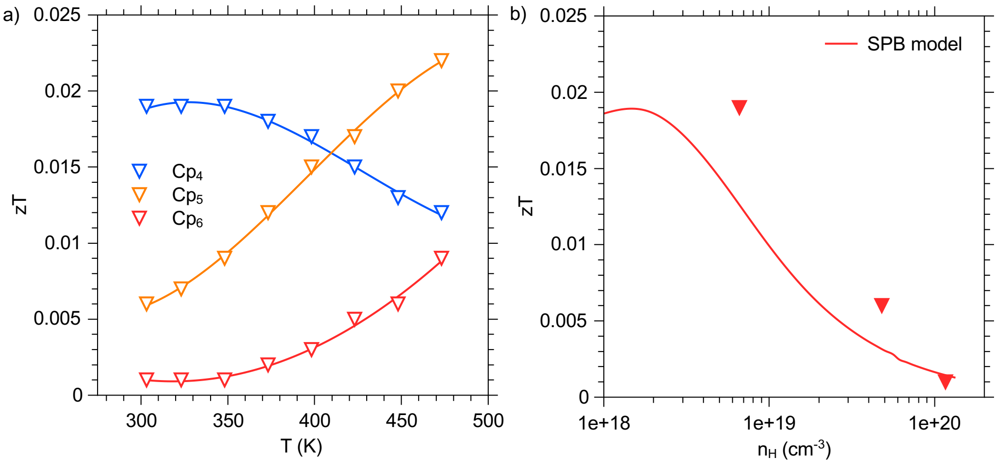

Figure 6.11: The figure of merit as a function of (a) temperature and (b) n_H as calculated by the SPB model for the In_2Te_3-Bi_2Te_3 composites.

Chapter 7

Transport properties of iodine-doped bismuth telluride

7.1 Introduction

Bismuth telluride crystallizes in a rhombohedral structure (space group R$\bar{3}$mh), however it is often depicted by the conventional hexagonal unit cell structure (Fig. 1.3) [14]. Undoped Bi_2Te_3 typically shows p-type conduction, but can be tuned to allow n-type conduction via Te excess or Halogen substitution.

The fact that most undoped bismuth telluride is at first p-type is due to anti-site defects of the bismuth cations occupying a tellurium site, specifically Te1 (Fig. 1.3). There have been several studies of the defect chemistry of pure Bi_2Te_3 due to interest in its properties as both a good thermoelectric material [162], but also due to the recent discovery for its potential as a topological insulator [18, 17]. While the desired results are drastically different between the two fields, the results from defect formation energy calculations agree that the Bi-rich conductivity is dictated by bismuth ions occupying the Te_1 site, and the Te-rich conductivity by tellurium ions occupying the Bi sites.

There are two main works that have studied the effects of Halogen [13] and self-doping [19, 163, 164] effects in bismuth telluride, but as is most often the case, new techniques and new understandings often warrant re-evaluations of what is considered established information.

7.2 Orientation and doping

Before the necessary transport measurements can be made, it is first necessary to crystallographically orient the material in order to properly understand the measurement results. Techniques often used in oriented material growth are the Bridgman method [20], traveling heater method [16], and zone melting (further described in Chapter 4) [21]. There is no distinction between the traveling heater method and zone melting, and the technique was originally coined zone melting, therefore this will be the nomenclature used to describe the technique.

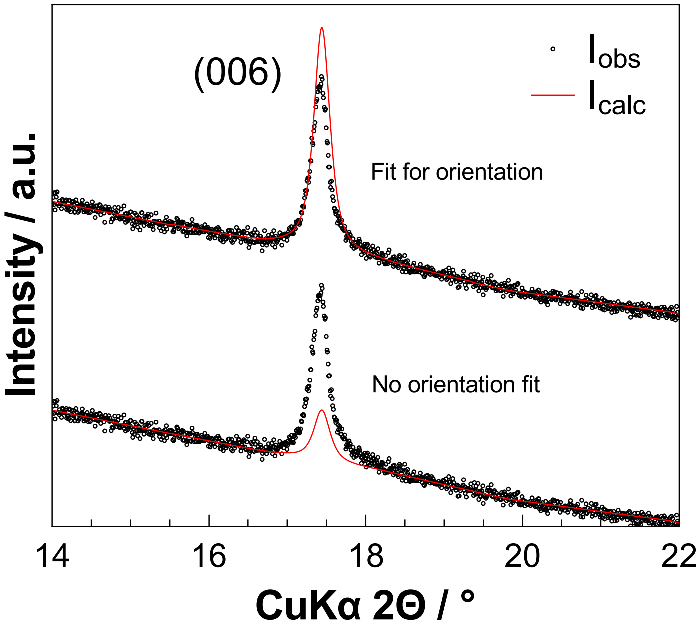

Figure 7.1: Typical x-ray diffraction results for the parallelpiped of oriented Bi_2Te_3 after zone melting. Rietveld refinements correcting for orientation fit the raw diffraction significantly better than without correcting. Moreover, the results show that there is significant orientation relative to the (00n) family of planes, indicating that the majority of incoming radiation is scattered off of the basal plane which is the desired orientation.

Due to the anisotropic nature of the crystal structure in Bi_2Te_3 there are preferred crystallographic directions with regard to solidification. Since close packed planes tend to be the lowest energy (most mobile), materials tend to prefer to grow along close packed planes (often in close packed directions). Therefore, it is not surprising that Bi_2Te_3 tends to solidify with the basal plane parallel to the growth direction [13]. This is important because the transport properties in this direction can be optimized to achieve the highest zT. However, unlike in the case of the In_2Te_3 structured samples (Chapter 6), there is no visual diagnostic to indicate orientation.

However, x-ray diffraction was conducted on samples of Bi_2Te_3 doped with iodine to ensure the crystallographic orientation was successful. As can be seen in Fig. 7.1, a typical XRD pattern is shown for an as grown parallelepiped sample used in n_H and ρ measurements. Using a modified Marchs function to accommodate for preferred orientation along the (00n) Miller indices leads to a fit more representative of the diffraction data. The refinement indicated a plate-like habit of the crystallites (grains) with near 90 % of the crystallites exhibiting the (001) hkl planes parallel to the surface of the sample.

The diffraction results also confirm that there are no major secondary phases present. Electron microscopy results (Fig. 7.2) reinforce this fact, as there are no obvious secondary phases in the

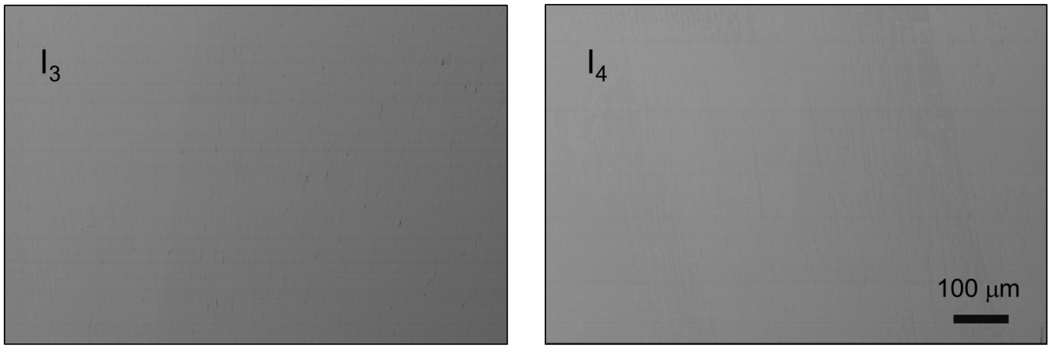

Figure 7.2: Scanning electron microscope images using the backscatter detector showcasing the lack of major secondary phases present in two typical iodine doped Bi_2Te_3 samples.

SEM images of the as grown zone melted material.

The doping efficiency of iodine in Bi_2Te_3 was established by first preparing the undoped material, measuring the Hall carrier concentration ($|n_H| = 1.7e19$), and then using simple charge valence counting (1 electron per iodine atom) comparing the measured Hall carrier concentration to that of the expected value. As can be seen in Fig. 7.3, the efficiency of iodine doping in Bi_2Te_3 is very near unity between 0.1 0.3 at. % iodine. The departure from the expected carrier concentration is most likely due to a decrease in solubility for 0.5 at. % iodine.

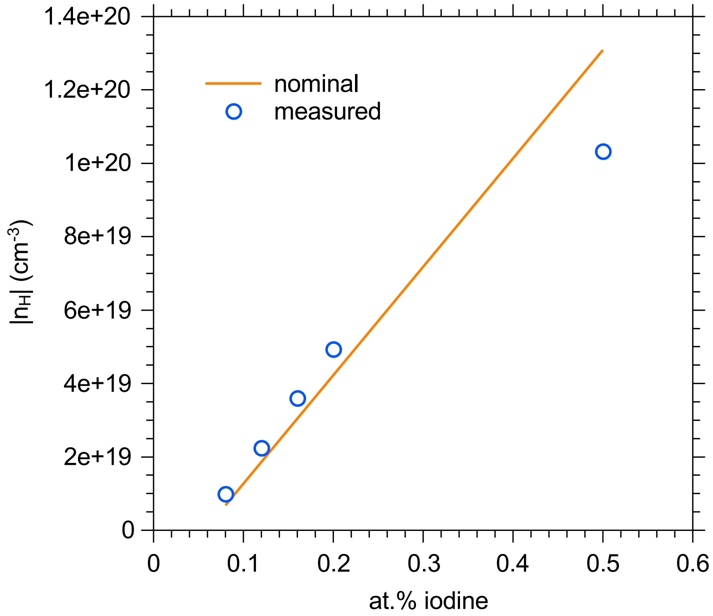

Figure 7.3: The doping efficiency of iodine in Bi_2Te_3. As can be seen, the measured Hall carrier concentration in the reason of interest is nearly that of the nominal concentration indicating a highly efficient electron donor in iodine.

7.3 Electron transport

Fig. 7.4 contains the data for the Hall carrier concentration (n_H), Hall mobility (μ_H), resistivity (ρ) and Seebeck coefficient (α) for a series of iodine doped Bi_2Te_3 samples. Fig. 7.4a corroborates the doping efficiency of iodine in Bi_2Te_3, as there is a steady increase in n_H with increasing iodine content at 300 K for all samples. However, there is an increase in n_H as a function of temperature due to thermal activation of carriers.

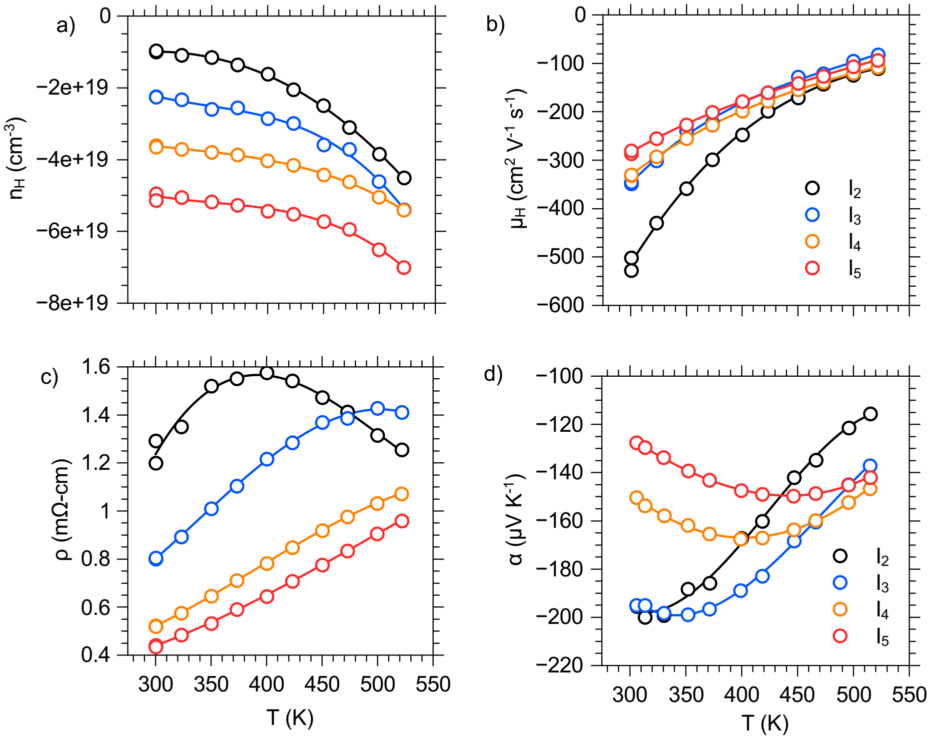

Figure 7.4: Here is the temperature dependent electron transport of iodine doped Bi_2Te_3. The (a) Hall carrier concentration (n_H) (b) Hall mobility (μ_H) (c) resistivity (ρ) and (d) Seebeck coefficient (α) are plotted for several samples.

Fig. 7.4b shows a decreasing Hall mobility (μ_H) as a function of both temperature and carrier concentration. The decrease in mobility as a function of temperature exists due to increased phonon scattering, but also due to bipolar conduction that arises from an increase in minority carriers. The decrease in mobility as a function of carrier concentration is due to an increased scattering from the increased impurity atom (iodine).

The room temperature resistivity values decrease with increasing carrier concentration due to the increase in n_H, knowing that $\rho = 1/ne\mu$ (Fig. 7.4c). For the heavier doped samples, the resistivity increases with increasing carrier concentration, which is typical for single carrier systems. The decrease in resistivity near 400 K of the lowest doped sample (I_2) is due to the presence of minority carriers.

The Seebeck coefficient data can be seen in Fig. 7.4d. The room temperature data for iodine doped data behaves as would be expected in a single band type system. The Seebeck value decreases with increasing carrier concentration as the Fermi level moves further into the band. The temperature dependent roll over seen in all the samples is due to the effects of bi-polar conduction, as is the cause of samples I_2 and I_3 to have a similar room temperature values.

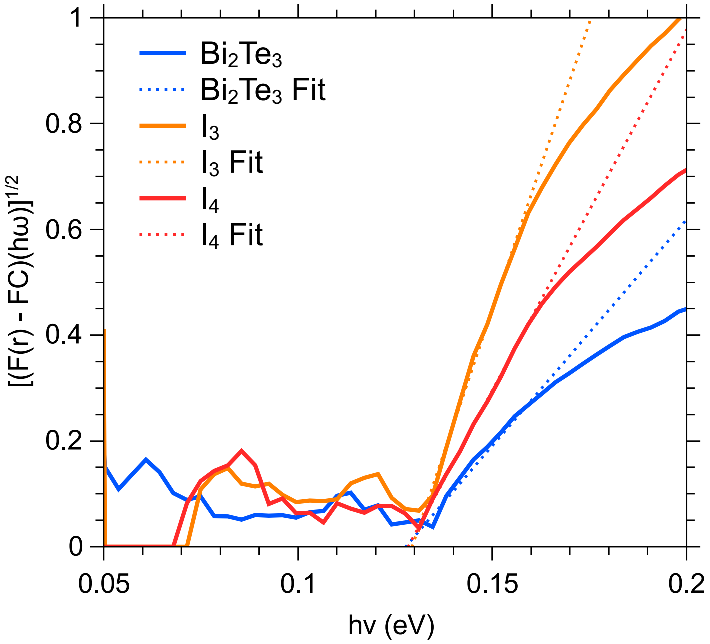

Figure 7.5: The Kubelka-Munk equation is plotted with the free carrier absorption subtracted for an indirect gap semiconductor. The spectra are fit at the onset of absorption and extrapolated to zero abosorption to determine the band gap E_g. In the case of undoped and doped Bi_2Te_3 the results indicate a band gap of 0.13 eV.

The significant effects of the bi-polar conduction are obvious when analyzing the electron transport data in n-type Bi_2Te_3. Several works have estimated the band gap of Bi_2Te_3 to be somewhere in the range of 0.1-0.2 eV [13]. Optical absorption measurements were taken on undoped and iodine doped samples of Bi_2Te_3 to estimate the optical band gap. Fig 7.5 is a plot of the Kubelka-Munk equation ($F(r)$) corrected for the free carrier absorption as a function of energy and fit to estimate the optical band gap of each sample. As can be seen, the data for all three spectra converge near the ~ 0.13 eV range for the measured optical gap.

7.4 Thermal transport

The resulting thermal conductivity and lattice + bipolar thermal conductivity can be seen in Fig. 7.6a-b. In a similar fashion to the electron transport data, the thermal conductivity is significantly affected by minority carrier transport. The room temperature thermal conductivity increases with iodine content, as would be expected as the carrier concentration increases. Since the thermal conductivity is made up of an electronic and lattice portion ($\kappa_e + \kappa_l$) with $\kappa_e = LT/\rho$, where L is the Lorenz number, and since it was previously discussed that ρ decreases as a function of carrier density, the increase in $kappa$ at room temperature is consistent.

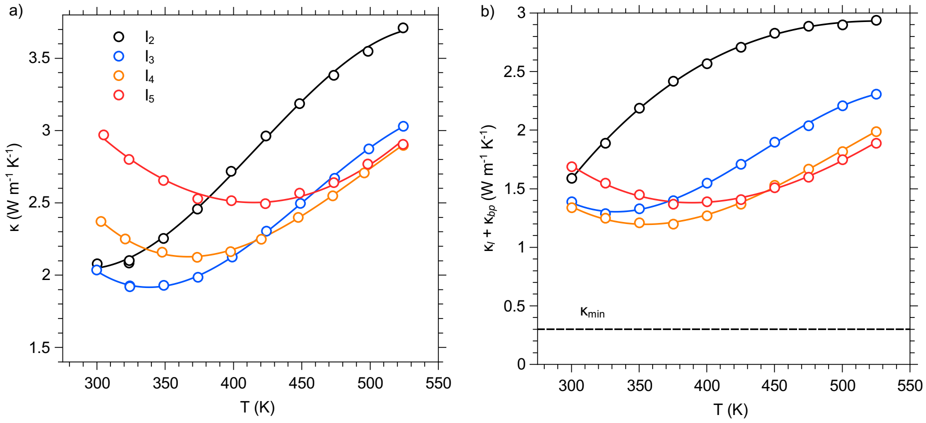

Figure 7.6: The temperature dependent (a) thermal conductivity (κ) and (b) lattice plus bi-polar thermal conductivity ($\kappa + \kappa_{bp}$) for iodine doped Bi_2Te_3. Also plotted in (b) is the minimum expected thermal conductivity based on the method of Cahill [161].

The $\kappa_l + \kappa_{bp}$ portion of the thermal conductivity at room temperature all share similar values. This is expected from the fact that the substitution of iodine into the lattice is not expected to alter the phonon dispersion significantly. However, since the electronic portion of the thermal conductivity is calculated and then subtracted from the total thermal conductivity, the increase in $\kappa_l + \kappa_{bp}$ is due to the bipolar term. The dominant scattering mechanism is believed to be umklapp scattering, as the temperature dependence of $\kappa_l + \kappa_{bp}$ for the heavier doped samples (less likely to be affected by minority carriers) behaves as $1/T$. Also plotted in Fig. 7.6b is the minimum lattice thermal conductivity as calculated by Cahill's method [161]. As the lattice thermal conductivity at room temperature is $\sim$ 1.5 W/mK, it is clear that Bi_2Te_3 is a good candidate for thermal conductivity reduction in one of the many available forms [165].

It should be mentioned as well that even though the Debye temperature in bismuth telluride is quite high ($\sim$ 160 K), the Dulong Petit limit for heat capacity is an acceptable choice as determined by inelastic neutron scattering [27].

7.5 Single parabolic band modeling

The dependence of the Seebeck coefficient and Hall mobility are well described in terms of a single parabolic band model. This model assumes a rigid band of constant effective mass and that the dominant scattering mechanism is by acoustic phonons (umklapp scattering). Fig. 7.7a-b are the theoretical curves for a single parabolic band at 300 K with $m* = 1.0m_e$, $\kappa_l = 1.7$ W/mK and $|\mu| = 410$ cm^2/Vs for both the Seebeck coefficient (α) and the Hall mobility (μ_H) as a function of n_H. As can be seen, the data fall in line well with the predicted values based on the model.

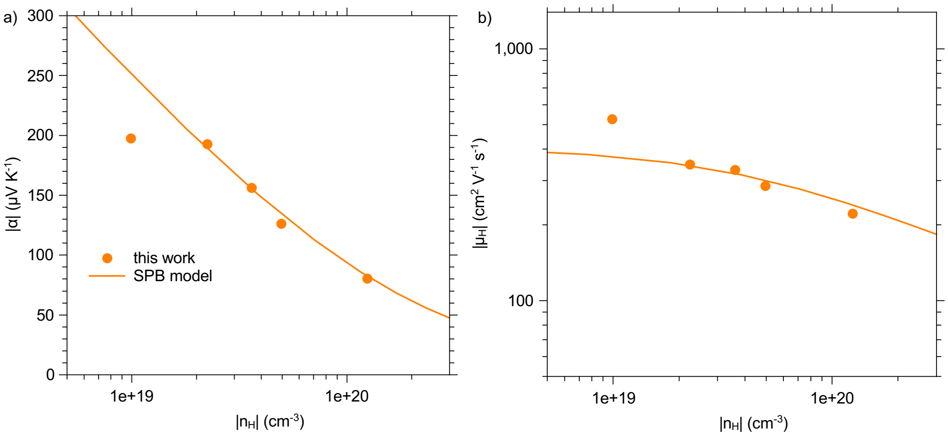

Figure 7.7: A single parabolic band modeling scheme [19] was used to model (a) the Seebeck coefficient (α) and (b) Hall mobility (μ_H) as a function of Hall carrier concentration (n_H). As can be seen there is good agreement between the model and the data for a single effective mass. A significant departure from the model and the data can be seen at lower carrier concentrations due to the thermal activation of carriers.

The higher concentration mobility data (Fig. 7.7b) does appear to slightly depart from the model, which is potentially due to the non-parabolicity of the conduction band [166] away from the band edge. The data at the lowest carrier concentration do not fit within the parameters of the model due to the effects of the minority carrier scattering. It is not known why the mobility is increased in the bipolar region, however it is difficult to acquire consistent Hall data in this region due to the presence of the minority carriers, so the data in the bipolar region should be evaluated with less confidence.

7.6 Figure of merit

The figure of merit (zT) for n-type Bi_2Te_3 is shown in Fig. 7.8a. These curves are generated from polynomial fits of each individual material property (as a function of T) necessary in computing zT. The peak value of $zT = 0.7$ in iodine doped Bi_2Te_3 occurs near 375 K for $|n_H| = 3.60e19$ cm^{-3}. However, the sample I_3 with $|n_H| = 2.24e19$ cm^{-3} has a peak value that is just under 0.7 at 300 K, with both values falling within the expected 20 % uncertainty, effectively being the same.

Typical optimization of zT for a single band system without the presence of minority carriers would dictate that the peak zT value at the optimal n_H would be the highest. Therefore, it is important to note the effects of the minority carrier presence in n-type Bi_2Te_3, as the single parabolic band model predicts that the optimal zT is near 0.7 at $n_H \sim 2.0e19$ cm^{-3} (Fig. 7.8b). The data presented based on the measurements in this study, however, indicate that the optimal carrier concentration lies somewhere between 2.2-3.6e19 cm^{-3}.

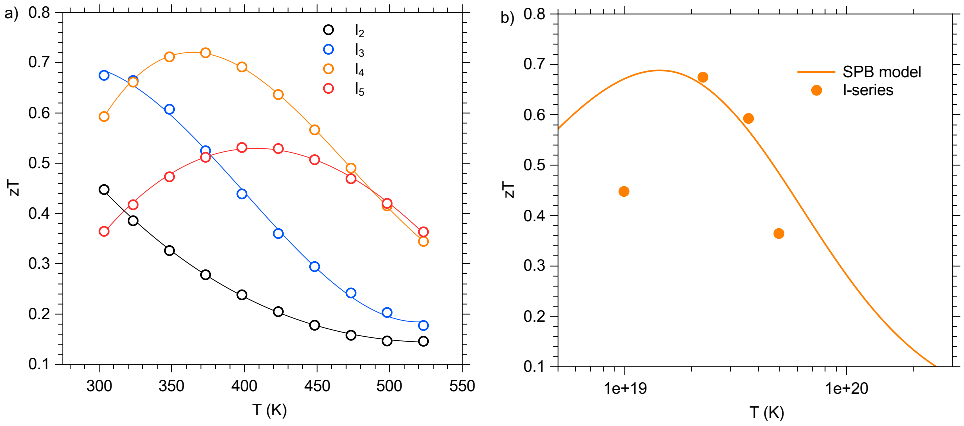

Figure 7.8: zT is plotted as a function of both (a) temperature and (b) Hall carrier concentration (n_H) for the iodine doped samples in this work. A peak zT of 0.7 is achieved between 300-375 K for samples I_3 and I_4. As can be seen in (b) the data fits the model well at carrier concentrations that are not negatively affected by the presence of minority carriers. The model over predicts the sample at high carrier concentration, indicating that a higher thermal conductivity is predicted for single band conduction, nonparabolicity in the conduction band or both.

7.7 Comparison to literature

The story of n-type Bi_2Te_3 becomes more complex when comparing the data in this work to that of the literature. Of the two hallmark works investigating n-type Bi_2Te_3 there are significant distinctions to be made in both. In the work of Goldsmid [13] the materials were doped with either iodine or chlorine, with no distinction in the data based on comparable transport results. The author states that there is little difference in the scattering cross section of an iodine vs. chlorine ion in the tellurium lattices of Bi_2Te_3. Another distinction made is that there is little difference between single crystal halogen doped Bi_2Te_3 and oriented polycrystalline data.

With this knowledge in hand, it is not surprising to find that when both the Seebeck coefficient and thermal conductivity are plotted against resistivity (i.e., gauging zT) that the results agree. Displayed in Fig. 7.9a-b are both the Seebeck coefficient (α) and thermal conductivity (κ) plotted as a function of resistivity (ρ) at 300 K. There is a strong matching of the Goldsmid data to that of the current iodine doped data presented here. The only departure exists for the higher resistivity (lower n_H) samples in which the effects of bipolar conduction are more clearly present in recent data. It is not clear why the presence of minority carriers is stronger in the recent iodine doped samples as opposed to the Goldsmid data. However, the result peak zT calculated from the data at 300 K is near 0.7, as it is for the data presented in this work.

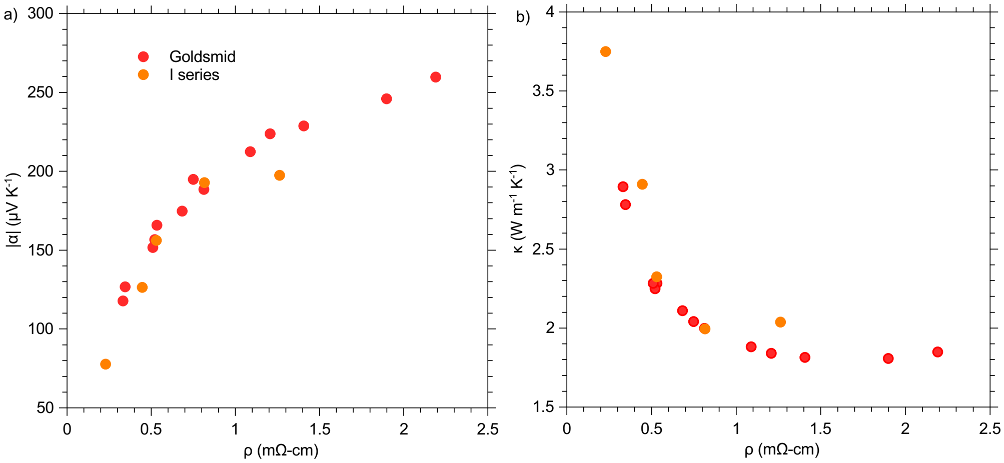

Figure 7.9: The Seebeck coefficient and thermal conductivity data plotted against resistivity from the iodine doped Bi_2Te_3 samples from this work and that of Goldsmid [13]. The data from both series match well except at higher resistivity (lower carrier concentration). It is unclear why the effects of bi-polar conduction are less severe in the Goldsmid work.

The other major work in n-type Bi_2Te_3 was conducted by Fleurial et al. [163, 164], in which they investigated the effects of self-doping. Samples were synthesized using zone melting (referred to as the traveling heater method in their work) and then through knowledge of the phase diagram, they utilized the saturation annealing technique to vary the Te content. In this technique the sample (after zone melting) is placed in an ampoule with a powder of Bi_2Te_3 with the desired composition to control the carrier concentration. The material was then annealed at a temperature such that the solid, liquid and vapor transport during the annealing resulted in appropriately doped material. Another distinction to be made is that all of the results in this work are reported from measurements done on single crystals of Bi_2Te_3, in which the values are reported parallel and perpendicular to the z axis.

The reported values of the Seebeck coefficient and Hall mobility were fit using a single parabolic band model, and then plotted in comparison with the data collected in this work (Fig. 7.10a-b). The resulting model parameters used to best fit the data were $m* = 1.6 m_e$, $\kappa_l = 1.6$ W/mK, and $\mu_0 = 240$ cm^2/Vs. This is a 60 % increase in effective mass compared to iodine doped Bi_2Te_3 which results in a 60 % decrease in mobility. This should result in an overall lower peak zT value than iodine doped Bi_2Te_3 [167], however the reported value at 300 K is ~ 0.85.

In order to understand how this is possible, it is important to examine the individual material properties that make up the figure of merit. The reported values of κ and ρ are similar to iodine doped Bi_2Te_3, so the Seebeck coefficient is examined. As can be seen in Fig. 7.10a the Seebeck value at the lowest carrier concentration is affected by the minority carrier presence, which indicates a similar band gap for the two systems. However, for the data at higher carrier concentrations, there is a region that is not described by a single effective mass. In the range of $3e19 - 1e20$ cm^{-3} the effective mass appears to decrease (lower α) to near the value that is predicted from iodine doping. Then at the highest carrier concentration in the tellurium doped system, the effective mass increases (higher α) back to predicted value.

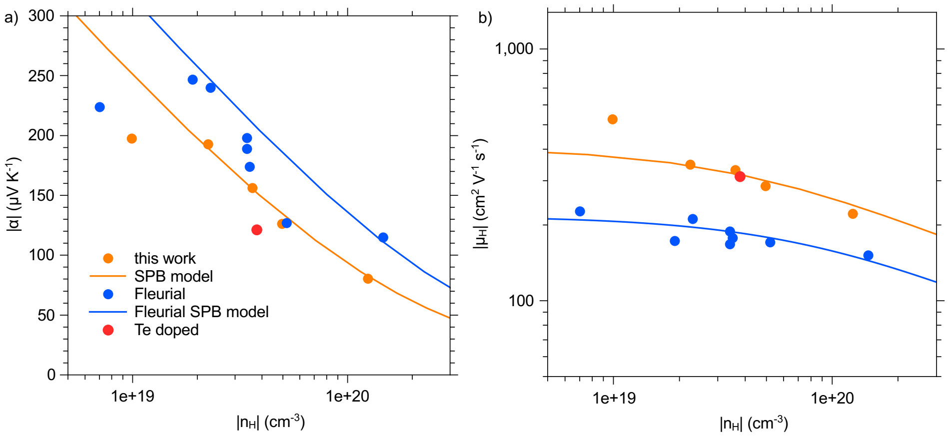

Figure 7.10: The (a) Seebeck coefficient ($|\alpha|$) and (b) Hall mobility ($|\mu_H|$) as a function of Hall carrier concentration ($|n_H|$) for iodine and tellurium doped samples prepared in this work to that of Fleurial et al. [163, 164]. Also plotted are the expected values based on a single parabolic band model.

Another concern with the reported Seebeck values is that at $\sim 3e19$ cm^{-3} there are three data points that have a varying Seebeck coefficient ($\sim 174 - 198\mu$V/K). Unless there were significant changes to the band structure for the different samples at this carrier concentration, the Seebeck coefficient should not vary other than from the measurement uncertainty. In fact, one self doped sample was created in this work to see the difference between purely zone melted and tellurium doped Bi_2Te_3 to that made by the saturation annealing technique. As can be seen (red dot Fig 7.10a-b), the Te doped Bi_2Te_3 falls in line more with the iodine doped data than it does the literature values.

The variation is believed to be due to measurement technique differences. The technique involved in measuring the Seebeck coefficient in the work of Fleurial et al. can be described as a 2-point geometry with the thermocouples embedded in nickel plated discs of copper soldered to the sample [168]. However, the samples measured in this work were done using a 4-point uniaxial technique with the thermocouples in direct contact with the material surface. It is known that surface contact probes provide the most consistent and accurate results [169], while embedding can lead to offsets in temperature and voltage [26].

7.8 Conclusion

An investigation into Bi_2Te_3 revealed that iodine is a successful n-type dopant, and it substitutes at near 100 % efficiency. X-ray diffraction revealed that zone melting is an effective method to grow oriented polycrystalline samples that have transport properties similar to similarly doped single crystals. The transport properties resemble that of a typical n-type semiconductor. However, due to the small band gap, it is an effective thermoelectric material near room temperature.

It was also determined that at 300 K the data presented here corroborate work done by Goldsmid [13] and significantly depart from that of Fleurial et al. [163, 164]. It is believed that rather than a changing effective mass in tellurium doped Bi_2Te_3, that it is in the Seebeck metrology used at that time. Since it is known today that surface contact is vital to Seebeck measurements the contemporary metrology is expected to yield more accurate results.

Appendix A

Derivation of concentration profiles in direct normal solidification and zone melting

A.1 Solute concentration profile for direct normal solidification

In this derivation (largely taken from [21, 130]) the assumptions made are that there is (1) no diffusion in the solid and (2) complete diffusion in the liquid during bulk normal solidification. This type of solidification is often referred to as solidification of the Bridgman type [20]. In practice, this technique involves the complete melting of a material (overall concentration C_L) and then solidifying that material from one end to the other by moving the ingot into a region where the temperature is lower than the melting point.

Below are the variables that will be used in the derivation of the solute concentration (C) as a function of fraction solidified (g).

$g \equiv$ Fraction of original volume which has solidified
$s \equiv$ Amount of solute remaining in the liquid
$s_0 \equiv$ Total amount of solute
$C \equiv$ Solute concentration in the solid at the solid-liquid interface
$C_l \equiv$ Solute concentration in the liquid

By definition of the equilibrium distribution coefficient it is known that $C = k_0 C_l$. Since $C_l = s/1-g$, it can be equated that

$$C = \frac{k_0 s}{1-g}. \tag{A.1}$$

After a fraction g has solidified, the next amount to freeze will be dg, and this newly solidified layer will have the concentration:

$$C = -\frac{ds}{dg}. \tag{A.2}$$

Since Eqn A.1 is also a closed form of C, we can set these two expressions equal and integrate:

$$\int_{s_0}^{s} \frac{ds}{s} = \int_{0}^{g} \frac{-k_0}{1-g} dg, \tag{A.3}$$

which solves to $s = s_0(1-g)^k_0$. Since $C = \frac{-ds}{dg} = k_0 s_0 (1-g)^{k-1}$ and the original volume was unity, $s_0 = C_0$, where C_0 was the original solute concentration. This allows the final form to be

$$C = k_0 C_0 (1-g)^{k_0 - 1}, \tag{A.4}$$

which is the concentration profile for normal bulk solidification as a function of fraction solidified g.

A.2 Solute concentration profile for zone melting

This section derives the solute concentration profile for an ingot that undergoes zone melting. This applies equally to any single pass zone melting technique, whether zone refining or zone leveling, however it is only sufficient to describe a single pass.

As before, the k_0 is the equilibrium distribution coefficient, however C in this instance is the concentration of the solid at any point x. Below are the variables used to determine the concentration profile as a function of distance (x/L) in terms of zone lengths.

$C_0 \equiv$ Mean concentration of solute in charge
$C_l \equiv$ Solute concentration in the molten zone
$s \equiv$ Quantity of solute in zone at any x
$s_0 \equiv$ Quantity of solute in zone at $x = 0$
$L \equiv$ The zone length
$x \equiv$ Distance along ingot at any point

Assume a molten zone has advanced a distance dx. As an incremental volume of solid will form dx, an equal volume will melt. The quantity of solute frozen out is:

$$k_0 C_l dx, \tag{A.5}$$

and $C_l = s/l$ assuming unit cross-sectional area. The quantity entering the molten zone is $C_0 dx$, so the net change in s is therefore given by:

$$ds = (C_0 - \frac{k_0 s}{L})dx, \tag{A.6}$$

which gives the differential equation

$$\frac{ds}{dx} + \frac{k_0}{L}s = C_0. \tag{A.7}$$

Solutions to equations of this type take the form

$$se^{k_0 x/L} - s_0 = C_0 \int_0^x e^{k_0 x/L} dx = \frac{C_0 L}{k_0}(e^{k_0 x/L} - 1), \tag{A.8}$$

and since $s_0 = C_0 L$, then this can be reduced to

$$s = C_0 L \frac{k_0 - 1}{k_0} e^{-k_0 x/L} + \frac{C_0 L}{k_0}. \tag{A.9}$$

Since $C = k_0 s/L$ the final form

$$C/C_0 = 1 - (1 - k_0)e^{-k_0 x/L} \tag{A.10}$$

can be fully expressed.

Appendix B

Material evaluation for transport measurements: use of the Seebeck coefficient

B.1 Introduction

The Seebeck coefficient was used as an effective method to quickly evaluate doping homogeneity of the materials measured in this thesis. Since α is quite sensitive to the doping level, i.e., η [19] each sample synthesized underwent a minimum of two Seebeck measurements. Each measurement was done from a cross section at each end of the sample that was used in the Hall measurements.

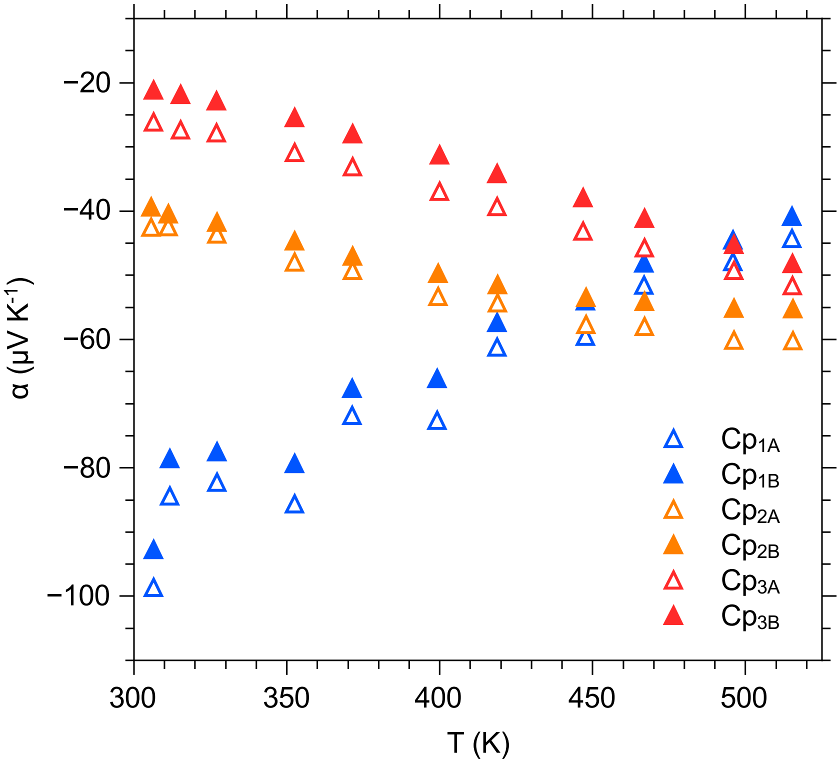

Figure B.1: Here is the consistency in the Seebeck coefficients for samples Cp_1-Cp_3. Each sample grown was checked at both ends of the ingot that was used in measuring the resistivity and Hall values in order to establish homogeneity.

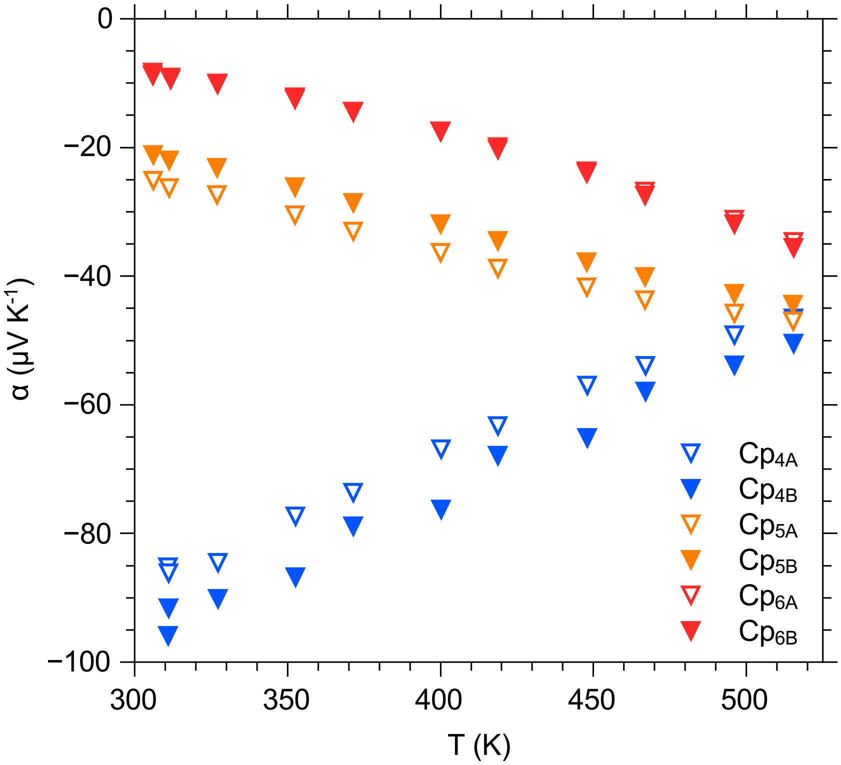

Figure B.2: Here is the consistency in the Seebeck coefficients for samples Cp$_4$-Cp$_6$. Each sample grown was checked at both ends of the ingot that was used in measuring the resistivity and Hall values in order to establish homogeneity.

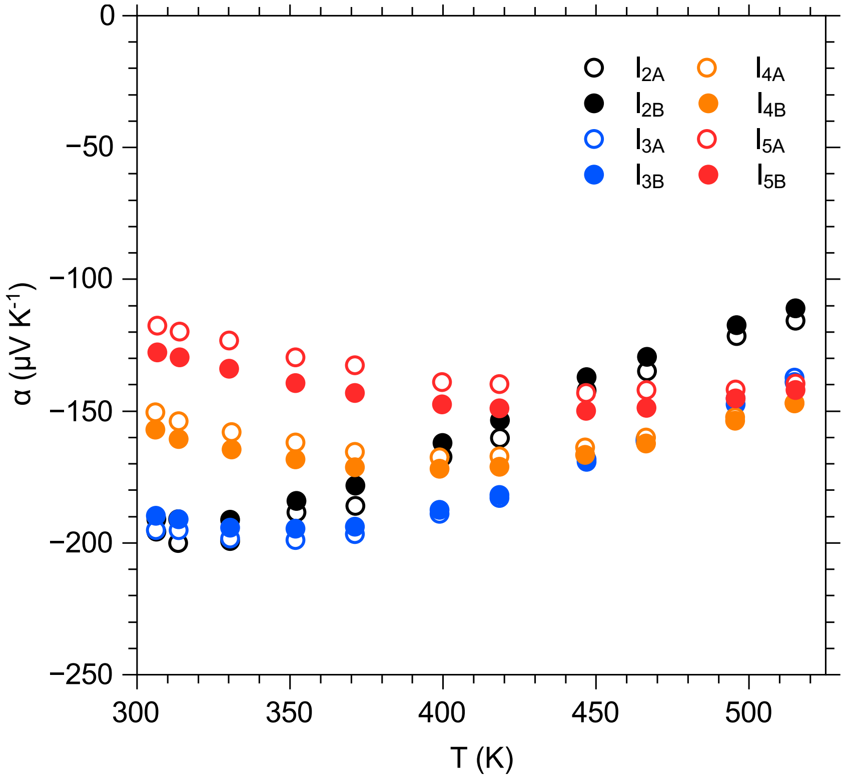

Figure B.3: Here is the consistency in the Seebeck coefficients for samples I_2-I_5. Each sample grown was checked at both ends of the ingot that was used in measuring the resistivity and Hall values in order to establish homogeneity.

Appendix C

Hot pressing and nanostructuring of $Bi_{90}Sb_{10}$ alloys to concurrently improve mechanical and thermoelectric properties

Reproduced with permission from *Physica status solidi A-applications and materials science* **209**, 2565-2569 (2012).

C.1 Introduction

The presence of nanosized precipitates has been shown to decrease the lattice thermal conductivity in some thermoelectric materials by scattering phonons at structure interfaces, while maintaining a desirable power factor [131, 79]. While studies of Bi-Sb based alloys have been done in the past that attempt to exploit a decreasing grain size to achieve this result [170, 171, 172, 173, 174, 175, 176], the aim of this work is to use a metallurgical approach [10, 9, 11] to improve the mechanical and thermoelectric properties of $Bi_{90}Sb_{10}$. Using bulk processing and consolidation techniques we plan to synthesize nanosized Ag and As rich precipitates within grains large enough to limit charge carrier scattering at the grain boundaries.

Traditionally, studies done involving these alloys consist of single crystal measurements both in and perpendicular to the trigonal direction [177], however, this work will focus on a side not as often studied, the properties of polycrystalline samples. Some argue that the possibility of a reduced grain size could decrease the thermal conductivity due to additional phonon scattering at grain boundary interfaces [175, 176], but this has proven to be ineffective in Bi-Sb alloys as it severely limits electron mobility [173, 178]. However, if one were able to attain a large grain size, while maintaining a reduced thermal conductivity, this would eliminate charge carrier scattering, and ideally improve the figure of merit. One possible route to obtain such a configuration would be to first make an isoelectronic composite of the desired Bi-Sb alloy and a non-parasitic secondary phase, and upon consolidation, achieve the desired grain growth to minimize grain boundary scattering.

Historically there have been two types of consolidation procedures for making polycrystalline Bi-Sb alloys, namely cold pressing and either isothermal annealing (sintering) or hot extrusion [170, 171, 172, 173, 174, 175, 176]. Reports indicate that sintering leaves a randomized grain structure with no preferential texturing [171, 175], however hot extruding leads to some form of texturing along the extrusion direction [170, 175]. The literature suggests that there is better consolidation in the extruded samples than the cold pressed and sintered as well. Some authors went as far as to do the sintering in a temperature range where the solid and liquid are in equilibrium. This method was described to allow the melted material to fill the voids around the solid portions that do not melt. In our method we concurrently press and sinter in a rapid induction-heated press to allow for adequate grain growth while maintaining a maximal density. This should act to maintain the desired electronic properties, while the composite structure should decrease the thermal conductivity.

C.2 Methods

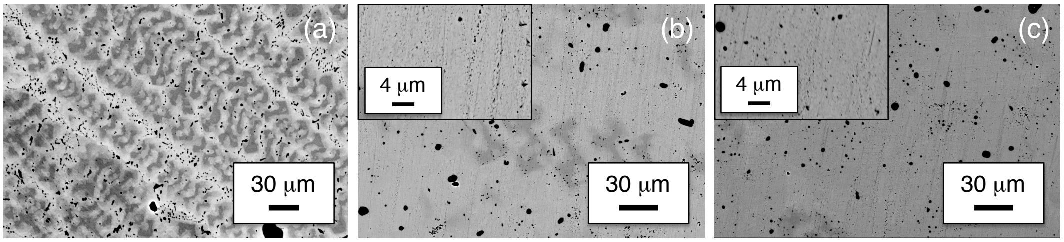

Figure C.1: Resulting backscattered electron images (BEI) of the microstructure for the 2 at. % Ag samples (a) quenched from the melt, and annealed at 250 °C for (b) 3 days and (c) 7 days. The additional annealing has little effect on the microstructure of the alloy composite as can be seen in the inset images.

Stoichiometric amounts of the pure elements were weighed out (99.999 % purity or better) to make pure $Bi_{90}Sb_{10}$, samples with 2 at. % Ag and As, and also 4 at. % As. The elements were sealed in fused quartz ampoules to a pressure of $\sim 10^{-5}$ Torr. The samples were then placed in a furnace and heated to a temperature of 800 °C at 6 °C/min. The samples were held at temperature for 18 hours and then immediately water quenched. The resulting ingots were cut for continued annealing and initial microstructure evaluation.

Samples that were annealed further were re-sealed in quartz ampoules and isothermally annealed in a range of 200-250 °C for either 3 or 7 days. These samples were imaged in a field emission scanning electron microscope (Zeiss LEO 1550 VP) utilizing both the backscatter and also secondary electron detectors. Imaged ingots were cut longitudinally, mounted in conductive epoxy and polished using a spectrum of SiC grit tapes ranging from #240−#800. Samples were then polished using 3 μm, 1 µm, and 0.3 µm suspended Al_2O_3 particles and finally polished with a 0.05 µm colloidal silica solution. Chemical analysis was done using energy dispersive x-ray spectroscopy (EDS) and the INCA software package. X-ray diffraction was also conducted for phase identification, but due to the low concentration of secondary phases in the samples (1.5 wt. % or less), none were detected.

The resulting samples of $Bi_{90}Sb_{10}$ with and without 4 at. % As were hand ground into powder in an agate mortar and pestle inside an Ar atmosphere. The powder was loaded in a graphite dye and sintered under 40 MPa at 230 °C for 20 minutes. The resulting samples (98% theoretical density or better) were cut, and polished for measurements of the electrical resistivity, Seebeck coefficient, and thermal conductivity. Depending on the direction measured, sample geometry was either a 12 mm diameter cylinder 1 mm thick, or a parallelpiped approximately $4\times11\times1$ mm^3. A similar treatment was done for the hot pressed samples imaged in the SEM.

Resistivity measurements were conducted using the Van der Pauw method under a 2T reversible magnetic field. Seebeck measurements were measured using the slope of the thermopower and temperature gradient from thermocouples of Chromel and Nb. Thermal diffusivity, D_T, was measured using a laser flash method (Netsch LFA 457). Using the density, d, from geometric measurements and mass of the sample, the Dulong-Petit value of the heat capacity and D_T, the thermal conductivity was calculated via $\kappa = dC_pD_T$.

C.3 Results and discussion

C.3.1 Silver samples

The microstructure of $Bi_{90}Sb_{10}$ with 2 at. % Ag as quenched, annealed at 250 °C for 3 days, and annealed at 250 °C for 7 days is compared in Fig. C.1a-c. EDS measurements reveal that the $Bi_{90}Sb_{10}$ matrix contained no detectable amount of Ag after annealing. This suggests that Ag is highly insoluble in $Bi_{90}Sb_{10}$.

The resulting Ag based composites annealed at 250 °C had precipitates (dark phase, Fig. C.1b-c) ranging from microns in size down to hundreds of nanometers. EDS conducted on the larger precipitates confirms they are Ag rich, most similar to the reported $Ag_{3.15}Sb_{0.85}$ phase [179], and it is likely that the smaller structures are as well. The excitation diameter in EDS is on the order of 1 µm, therefore the sub-micron precipitates could not be individually examined.

Room temperature Seebeck measurements were done on the annealed samples of $Bi_{90}Sb_{10}$ with 2 at. % Ag. The results were found to be similar to those of alloyed $Bi_{90}Sb_{10}$ as all composite thermopower values were -80 ± 6 µV/K, while single crystal data is near -95 µV/K [180]. This suggests that Ag is not a strong dopant in Bi-Sb at room temperature.

With such a limited range in solubility it is difficult to finely control the nucleation and growth of the Ag precipitates. The possibility of extending the solid solubility of Ag in Bi-Sb could be made possible, however, through mechanical alloying, as this has been an effective route in other alloy systems [109].

C.3.2 Arsenic samples

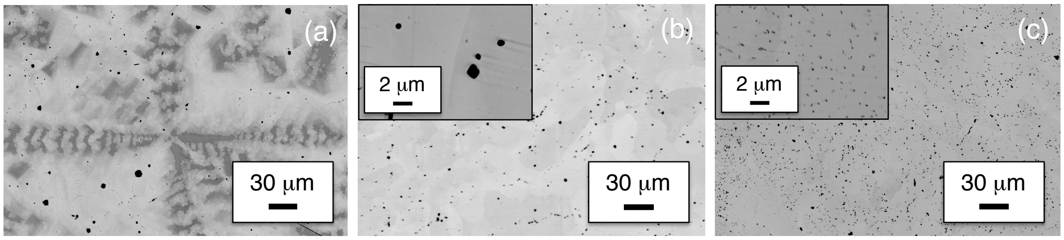

Figure C.2: Backscatter electron images (BEI) of the (a) melt microstructure of the 2 at. % As sample and (b) after annealing for 3 days at 250 °C. When the As content is increased to (c) 4 at. % and annealed at 250 °C for 3 days there is a significant difference in structure size and spacing. The inset of (c) shows the size and spacing of the 4 at. % As sample being of interest for thermoelectric applications.

The solubility of As in $Bi_{90}Sb_{10}$ is noticeably larger than Ag based samples. EDS measurements of the melt microstructure (Fig. C.2a) confirm the solubility of As ranges from 1.4 to 4.8 at. %. Though there was difficulty making a solid solution of the three elements, the fact that there is any As solubility after melting suggests that it may be possible to precipitate As rich particles by annealing at a temperature where there is a decreased solubility. This solubility limit is expected based on the binary phase diagrams of the constituent elements, as both Bi-Sb [69] and Sb-As [181] are completely miscible for a wide temperature range, but there exists no reported solubility between Bi and As [70].

When As substituted $Bi_{90}Sb_{10}$ is annealed at 250 °C for 3 days, micro to nanosized precipitates are observed, as shown in Fig. C.2b-c, in addition to the residual large precipitates from the melt. This evidence at least qualitatively shows that there exists a decreased solubility at 250 °C on account of the additional precipitation of the second, As-rich phase. The samples of $Bi_{90}Sb_{10}$ with 4 at. % As exhibited a larger number density and decreased precipitate size than those with only 2 at. %. This is most likely due to an increase in supercooling with increased As content. Also, the precipitates in the 4 at. % As samples increased in volume fraction and decreased in number density after additional annealing from 3 days to 7 days (not shown). This suggests that there was a transition in transformation mechanisms from a nucleation regime to a period of precipitate growth.

When similar samples were annealed at 200 °C, the lower temperature annealing resulted in little change from the melt microstructure (not shown). This is because the kinetics of diffusion limited the rate at which the system could approach the desired equilibrium state. There exist some precipitates in samples annealed at 200 °C, but in general the number of precipitates in samples were typically very few, even when annealed for 7 days.

C.3.3 Hot pressing

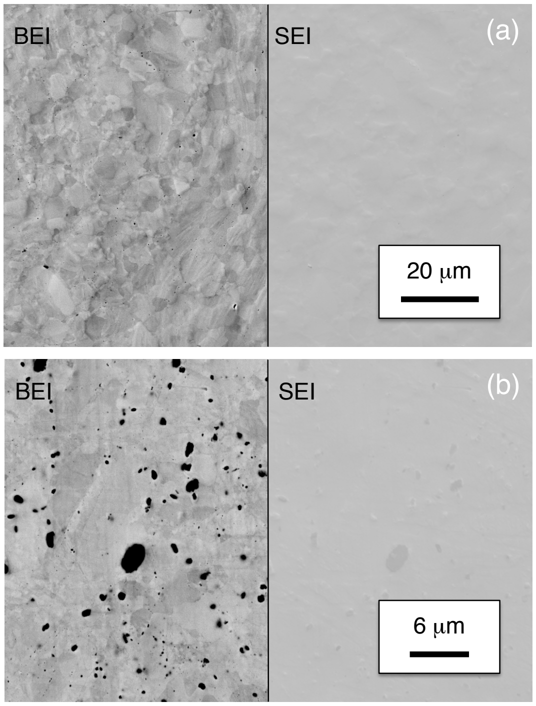

Figure C.3: Split backscatter electron images (BEI) and secondary electron images (SEI) after hot pressing for (a) pure $Bi_{90}Sb_{10}$ and (b) 4 at. % As annealed for 3 days at 250 °C, displaying the grain size and resulting structure size. The secondary electron images in (a) and (b) are to show the resulting images do not contain cracks or pores.

The aim in hot pressing is to improve the mechanical properties of the material by inhibiting cleavage of the basal planes typical in single crystals of Bi-Sb. Displayed in Fig. C.3a-b are two split-screen images of the resulting microstructure of both the pure $Bi_{90}Sb_{10}$ and the 4 at. % As samples. From these images it was determined that the grain size of the hot pressed samples ranges from less than 1 µm to over 10 µm for all samples measured. The lack of contrast in the SEI portions of each image also proves the effectiveness of this consolidation technique as pore formation typical of non-pressure-assisted sintering is not found.

As can be seen in Fig. C.3b, there has been a significant size increase in the As structures after hot pressing. This is not surprising, as the pressure assisted sintering can greatly influence the precipitation kinetics, and from simple isothermal annealing experiments, it was determined that somewhere between 3 and 7 days the As structures undergo significant growth.

It should also be mentioned that no orientation or texturing measurements were conducted in this study, however, Bi-Sb alloys have been known to texture when hot extruded [170, 175]. Therefore, the striation contrast that can be seen in Fig C.3a could potentially be due to texturing.

C.3.4 Transport properties in arsenic composites

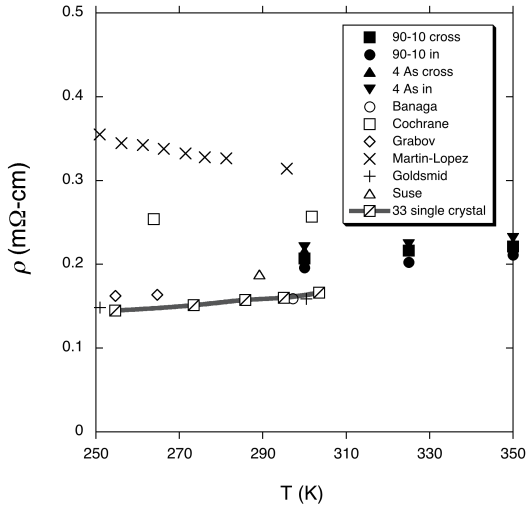

Figure C.4: Near room temperature resistivity data for polycrystalline $Bi_{90}Sb_{10}$ and 4 at. % As samples (both in the pressing direction and perpendicular to the pressing direction). Also shown is literature data for several other polycrystalline alloys [170, 171, 172, 174, 175, 176] and one single crystal sample of Bi-Sb [180] comparable to $Bi_{90}Sb_{10}$. The resistivity data for the hot pressed samples is slightly higher than the single crystal data, but lower than several of the other polycrystalline samples.

Bi, Sb, and As all share the same layered crystal structure (space group $R\bar{3}m$) [182, 183, 184], and past studies of single crystal data have proven that the most efficient crystallographic direction for TE purposes is along the trigonal axis, often referred to as the 33 direction [180]. For this reason, single crystal data reveal slight anisotropies in the thermopower and resistivity, but a significant difference in the thermal conductivity at room temperature [180]. It is because of this that transport property measurements were conducted in and perpendicular to the pressing direction.

Figs. C.4-C.6 compare the resistivity values, Seebeck coefficients, and thermal conductivities of the hot pressed polycrystalline Bi-Sb samples in this work to that of previous works involving polycrystalline alloys of Bi and Sb. All of the binary alloy literature data compared in these plots have compositions that range from 9-12 at. % Sb and similar cold pressing consolidation techniques [170, 171, 172, 173, 174, 175, 176]. Suse et al. differ slightly in that after cold pressing the samples were sintered above the solidus temperature [176]. Banaga et al. used a different technique in hot extruding samples after cold pressing, and in the case of the highest z sample, further annealed after extrusion [170].

The resistivity of all hot pressed samples created in this study have similar room temperature values (Fig. C.4). Compared to the single crystal data, there is approximately a 10% rise in resistivity due to hot pressing of $Bi_{90}Sb_{10}$ and an additional rise of 5% occurs in the As structured samples. The rise in resistivity in these cases is most likely due to the increased interfacial scattering

Table C.1: Room temperature Hall concentration (n_H) and mobility (μ_H) of the $Bi_{90}Sb_{10}$ and 4 As polycrystalline samples. Both types of sample geometries (in and perpendicular to the pressing direction) were used during the measurements and the results were always within 10% of the values reported here.

Sample	n_H (cm^{-3})	μ_H (cm^2/Vs)
90-10	1.0×10^{19}	-3300
4 As	1.1×10^{19}	-2600

at the grain boundaries. The additional rise in the As structured samples is expected to be due to the scattering at both grain boundaries and due to the As precipitates. This is supported by the decreased Hall mobility upon the addition of arsenic as seen in Table C.1.

The Seebeck values can be seen in Fig. C.5. The anisotropy in the Seebeck coefficient at room temperature is low [180] , so the samples were only measured in the pressing direction. The magnitude of the thermopower of the As added sample is lower than that of the alloyed Bi-Sb and both samples are comparable to the majority of other polycrystalline versions. Relative to the single crystal data there is similarly proportional behavior to the resistivity at room temperature, whereby the $Bi_{90}Sb_{10}$ and As structured samples decrease by 10% and 15% respectively.

Due to the change in Seebeck from the measured polycrystalline samples, it might be expected that there would be a change in carrier concentration. However, as can be seen in Table C.1, the Hall concentration is the same in both samples. Due to the complexity of the band structure, it is expected that a three band model [172] would be necessary to quantitatively describe this behavior.

It is in the thermal conductivity where the greatest room temperature change occurs. As seen in Fig. C.6, the thermal conductivity of the As based composite is lower than hot pressed $Bi_{90}Sb_{10}$ and both are significantly lower than the single crystal data. It is also interesting to note that the measurement direction seems to have little effect on the most anisotropic transport property of these alloys. It would be expected that if there were signs of texturing during the hot pressing stage it would be most obvious from the thermal conductivity data, but there is little resulting evidence of texturing based on these measurements.

The room temperature zT values for single crystal and polycrystalline $Bi_{90}Sb_{10}$ are the same at room temperature, both were ~0.30, while the As structured sample has a slightly smaller value of 0.24. While the overall zT is not highest in these samples, this is a promising result because the grain size, structure size, nor doping concentration were optimized for thermoelectric performance. If the grain size could be optimized in such a way that there was an even distribution of larger grains, while at the same time maintaining the fine microstructure observed in the non-hot pressed samples, the figure of merit may in fact be enhanced.

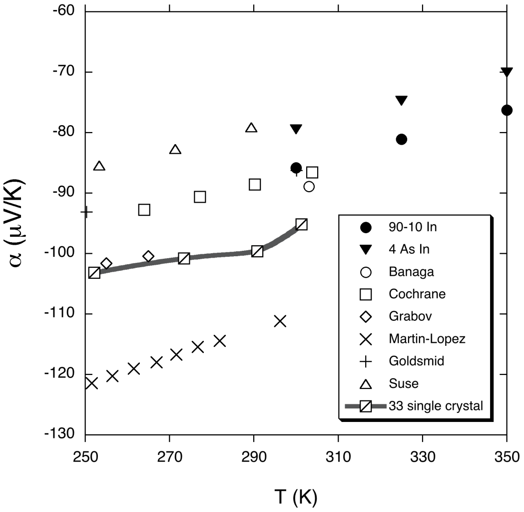

Figure C.5: Seebeck data for $Bi_{90}Sb_{10}$ and 4 at. % As samples. Due to the low level of anisotropy only the direction parallel to the pressing direction was measured. The hot pressed samples have comparable thermopowers to that of the referenced polycrystalline [170, 171, 172, 174, 175, 176] and single crystal [180].

C.4 Conclusion

We have found that the effects of nanostructuring and hot pressing $Bi_{90}Sb_{10}$ based materials is an effective route to improve the mechanical stability without diminishing the thermoelectric efficiency intrinsic in these alloys. The microstructure of $Bi_{90}Sb_{10}$ alloys with Ag and As was studied to synthesize micro to nanosized precipitates and room temperature transport measurements were made to assess the validity of this approach. Ag was determined to have relatively low solubility in $Bi_{90}Sb_{10}$ making it difficult to control the precipitate size. The most successful $Bi_{90}Sb_{10}$ samples were those containing As when annealed for a duration of 3 days at temperatures near 250 °C. The room temperature transport properties revealed that, even with unoptimized grain and structure sizes, the figure of merit of polycrystalline $Bi_{90}Sb_{10}$ is comparable to the reported single crystal value due to the reduction of κ. This indicates that if the structure size and spacing remains as in Fig. C.2c along with a large enough grain size, not only should the thermoelectric properties of polycrystalline Bi-Sb alloys approach the single crystal values, but potentially improve upon them as well, especially in the cryogenic temperature range where z is traditionally optimized.

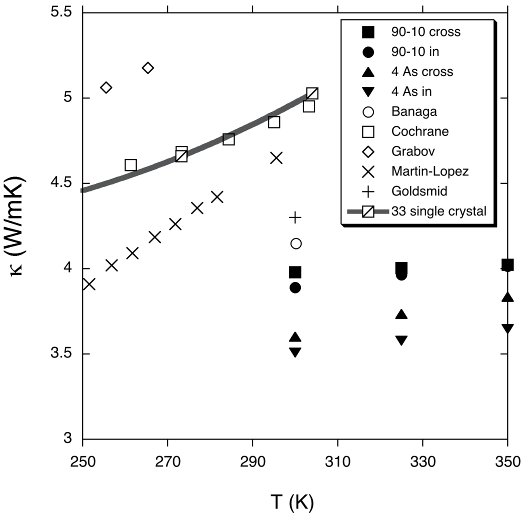

Figure C.6: Thermal conductivity data for $Bi_{90}Sb_{10}$ and 4 at. % As samples. There is a marked decrease in κ for all samples at room temperature when compared to polycrystalline [170, 171, 174, 175, 176, 178] and single crystal samples [180]. The lowest measured κ being in the As structured samples.

Appendix D

Interfacial disconnections at Sb_2Te_3 precipitates in PbTe: Mechanisms of strain accommodation and phase transformation at a tetradymite/rocksalt telluride interface

Reproduced with permission from *Acta materialia* **59**, 7724-7735 (2011).

D.1 Introduction

An emerging approach to tailoring the microstructure of thermoelectric materials is to embed high densities of internal interfaces within a bulk thermoelectric matrix through the control of phase transformations such as solid-state precipitation [185, 79, 30]. Such interfaces can improve thermoelectric performance by providing sites for phonon scattering, thereby reducing the thermal conductivity of the material. Rocksalt- and tetradymite-structured chalcogenides are of particular interest in this regard. Both types of structures have similar arrangements of close-packed metal and chalcogen layers, suggesting the possibility of forming well-ordered, coherent or semi-coherent interfaces that may avoid deleterious effects on the electronic transport properties while still providing an effective means to scatter phonons. These considerations have motivated interest in understanding the microstructural evolution and phase stability of two-phase rocksalt/tetradymite thermoelectric materials [36, 37, 12, 186, 187, 188, 189, 190, 72, 191, 192].

Fig. D.1 illustrates the crystal structures for the binary MX rocksalt ($Fm\overline{3}m$) and M_2X_3 tetradymite ($R\overline{3}m$) structures (where M and X refer to the metal and chalcogen atoms, respectively). Typically, tetradymite precipitates form in a plate-like morphology and are crystallographically aligned with the rocksalt matrix such that $\{111\}_{rocksalt}//(0001)_{tetradymite}$ and $\langle 10\bar{1}\rangle_{rocksalt}$ // $\langle \bar{2}110\rangle_{tetradymite}$; these plates are elongated parallel with the tetradymite basal planes [12, 72, 192]. For instance, Sb_2Te_3 precipitates in rocksalt-structured $AgSbTe_2$ were reported by Armstrong et al. [192], who found extensive networks of Sb_2Te_3 plates intersecting on {111} planes of the rocksalt matrix forming in a "Widmanstätten" -type microstructure. Ikeda et al. [12] reported similar microstructures for Sb_2Te_3 precipitates in PbTe.

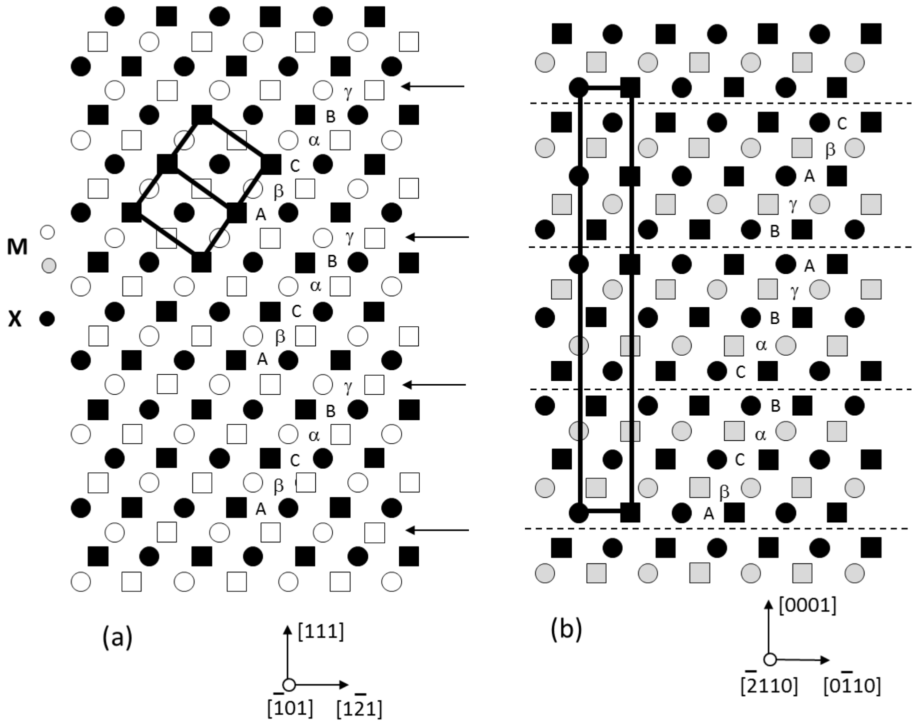

Figure D.1: (a) Schematics of the rocksalt and (b) tetradymite crystal structures. The stacking of the close-packed metal (M) and chalcogen (X) planes is indicated by Greek and Roman letters, respectively. Circles and squares indicate depth into the page.

Recent work has addressed the atomistic mechanism of the tetradymite precipitation. As illustrated in Fig. D.1, the close packed planes in both the rocksalt and tetradymite structures are stacked in similar, "...*ABC*..." type sequences. The two structures differ fundamentally, however, in their compositional ordering. In the rocksalt structure, the {111} planes alternate between metal and chalcogen layers, giving a total 6-plane repeat sequence along ⟨111⟩ directions. In contrast, in the tetradymite structure, two adjacent chalcogen layers arise every 5 basal planes, giving a 15-plane repeat sequence along the [001] direction. Based on electron microscopic observations of Sb_2Te_3 precipitates in rocksalt-structured $AgSbTe_2$, Medlin and Sugar [72] have proposed how growth of tetradymite plates could be accomplished through the motion of interfacial disconnections (line defects possessing both step and dislocation content [193]). Since the growth of tetradymite precipitates would require the motion of multiple interfacial disconnections, it is interesting to ask what controls the arrangement and interaction of such defects and how they might form.

In this paper, we investigate these questions in detail. We focus on precipitates of Sb_2Te_3 ($a_{hex} = 0.4264$ nm and $c_{hex} = 3.0458$ nm[194]) in PbTe ($a_{cub} = 0.6462$ nm [195, 196]). Previously, Ikeda et al. [197] demonstrated a strong suppression of lattice thermal conductivity with increased interface density in PbTe/Sb_2Te_3 nanocomposites, motivating interest in determining the atomic and mesoscale structures of interfaces in this system. Moreover, the PbTe/Sb_2Te_3 system is interesting from a structural standpoint because of its large lattice misfit across the $\{111\}_{PbTe}/(0001)_{Sb_2Te_3}$ interface of 6.7%, a misfit that is an order of magnitude larger than that of the $AgSbTe_2/Sb_2Te_3$ system studied previously by Medlin and Sugar [72]. Thus one anticipates that the interplay between the dislocation content of the interfacial defects and the interfacial coherency strain may play a key role in controlling the defect arrangements.

The appendix is organized as follows. First, we outline the crystallographic specification of interfacial defects at rocksalt/tetradymite interfaces. Next, we present electron microscopic observations of interfaces at Sb_2Te_3 precipitates in PbTe. Using high-resolution transmission electron microscopy (HRTEM), we analyze several interfacial disconnections and their spatial arrangement at interfaces vicinal to $\{111\}_{PbTe}/(0001)_{Sb_2Te_3}$. We then discuss how the step and dislocation content of the observed interfacial defects are related to the misfit accommodation and interface inclination in evolving precipitates in this system. Finally, we propose how such defects could arise from the dissociation of crystal lattice dislocations that accommodate the misfit on initially flat segments of the interface.

D.2 Defect crystallography at rocksalt/tetradymite interfaces

In this section we discuss the crystallography of line defects at rocksalt/tetradymite interfaces, laying out a framework for interpreting the experimental observations presented later in the paper. We follow the general topological theory of interfacial defects as developed by Pond [198], applying this approach to the specific case of rocksalt/tetradymite interfaces vicinal to $\{111\}_{rocksalt}$ and $(0001)_{tetradymite}$.

In general, the set of admissible defects at an interface between two crystals, λ and μ, is given from the set of lattice translation vectors in the two crystals [198]:

$$\mathbf{b}_{ij} = \mathbf{t}(\lambda)_j + \mathbf{P}t(\mu)_i. \tag{D.1}$$

Here, $\mathbf{t}(\lambda)$ and $\mathbf{t}(\mu)$ are lattice translation vectors in the two crystals, $\mathbf{P}$ is a matrix that transforms a vector from the crystal coordinates of μ to those of λ, and $\mathbf{b}_{ij}$ is the set of Burgers vectors obtained through different combinations of $\mathbf{t}(\lambda)_j$ and $\mathbf{t}(\mu)_i$. Throughout this appendix, we refer to the rocksalt phase (PbTe) as λ and the tetradymite phase (Sb_2Te_3) as μ, and we express $\mathbf{b}$ in rocksalt crystal coordinates.

We define the Burgers vectors with respect to a reference frame in which the crystals are aligned with $\{111\}_{rocksalt} \| (0001)_{tetradymite}$ and $\langle 10\bar{1}\rangle_{rocksalt} \parallel \langle \bar{2}110\rangle_{tetradymite}$ (as in Fig. D.1). Additionally, it is useful to define this reference frame so that the interatomic spacings within the $\{111\}_{rocksalt}$ and $(0001)_{tetradymite}$ planes are strained into coherency. An analogous approach has been discussed previously in the context of martensitic transformations [199] and strain accommodation at grain boundaries [200]. From these considerations, Medlin and Sugar [72] have constructed $\mathbf{P}$ for a coherently strained rocksalt(λ)/tetradymite (μ) system as:

$$\mathbf{P} = \begin{pmatrix} \frac{1}{2} & -\frac{1}{2} & \frac{c_{hex}}{a_{cub}\sqrt{3}} \\ 0 & \frac{1}{2} & \frac{c_{hex}}{a_{cub}\sqrt{3}} \\ -\frac{1}{2} & 0 & \frac{c_{hex}}{a_{cub}\sqrt{3}} \end{pmatrix}. \tag{D.2}$$

The above orientation relationship aligns in both crystals the threefold inversion axes $\bar{3}$ (along $[111]_{rocksalt}$ and $[0001]_{tetradymite}$) and the three mirror planes parallel with these axes (of type $\{110\}_{rocksalt}$ and $\{2\bar{1}\bar{1}0\}_{tetradymite}$). The interfacial structure, including the sets of interfacial defects, should be related through the symmetry elements shared between the two crystals and would ideally be expected to exhibit $\bar{3}m$ point symmetry.

Based on Eq. D.1, we considered several possible defect configurations for interfaces vicinal to $\{111\}_{rocksalt}$ and $(0001)_{tetradymite}$. A larger set of defects than presented here can be envisaged; however, we limit our discussion to a narrow set, with step heights in the tetradymite crystal of 0, $\frac{1}{3}c_{hex}$, and $\frac{2}{3}c_{hex}$, since these defects are of specific relevance to the experimental observations we consider next.

The simplest case to consider results from combinations of $\mathbf{t}(\lambda) = \frac{1}{2}\langle 110\rangle$ and $\mathbf{t}(\mu) = \frac{1}{3}\langle 2\bar{1}\bar{1}0\rangle$ translation vectors lying parallel with the $\{111\}_{rocksalt}/(0001)_{tetradymite}$ terrace plane. In this case, the defects with smallest Burgers vector are of type $\frac{1}{2}\langle 110\rangle$ (in μ). Because no step is associated with these $\frac{1}{2}\langle 110\rangle$ defects, one could anticipate these defects accommodating the misfit strain along flat sections of $\{111\}_{rocksalt}$ and $(0001)_{tetradymite}$ interface.

More complex configurations arise for steps. Fig. D.2 shows schematics for four defects resulting from different combinations of $\mathbf{t}(\lambda) = \langle 111\rangle$ and $\mathbf{t}(\mu) = \frac{1}{3}\langle 10\bar{1}1\rangle$, all of which possess steps that are six close-packed planes high in the rocksalt phase (λ) and five close-packed planes high in the tetradymite phase (μ). The geometric properties of these defects are summarized in Table D.1a. In a similar fashion, we also considered disconnections consisting of steps 10 planes high in each phase, which can be generated from combinations of $\mathbf{t}(\lambda) = \frac{1}{2}\langle 334\rangle$ and $\mathbf{t}(\mu) = \frac{2}{3}\langle 0\bar{1}11\rangle$ or $\mathbf{t}(\mu) = \frac{1}{3}\langle 01\bar{1}2\rangle$. These are illustrated schematically in Fig. D.3, and their geometric properties are tabulated in Table D.1a. For simplicity in the subsequent discussion, we denote these defects in terms of the number of planes constituting the steps in the rocksalt (λ) and tetradymite (μ) crystals and the sense, positive or negative, of the step, with the upper crystal listed first and the lower crystal second. For instance, the defect in Fig. D.2a is denoted +6/+5, whereas that in Fig. D.2c is denoted -5/-6.

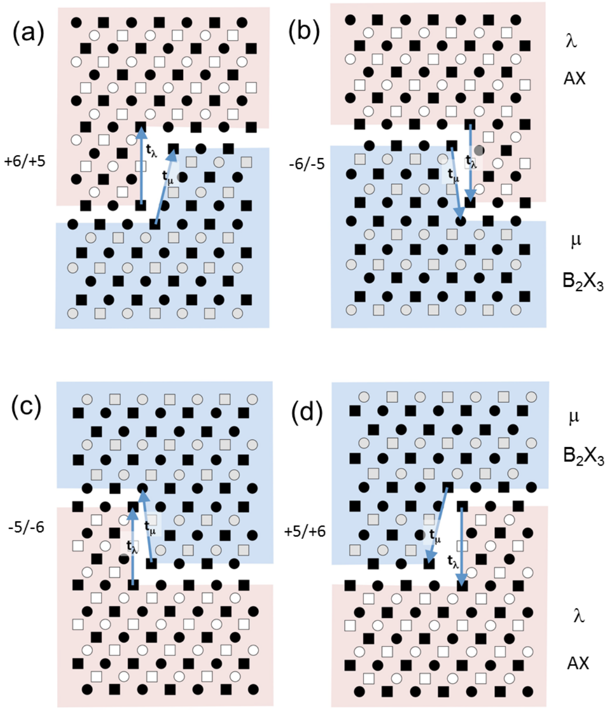

Figure D.2: Schematics of the set of 6/5-type disconnections obtained for different combinations of $\mathbf{t}(\lambda) = \langle 111 \rangle$ and $\mathbf{t}(/mu) = \frac{1}{3}\left\langle 10\bar{1}1 \right\rangle$. Each defect corresponds to a step of ±6 close-packed planes in the rocksalt phase (λ) and ±5 close-packed planes in the tetradymite phase (μ). The geometric specifications for these defects are shown in Table D.1a.

The defects in Figs. D.2 and D.3 are drawn in a relaxed, unstrained condition to make clear the difference in step heights in the rocksalt and tetradymite crystals. This incompatibility in step height gives a finite component of the Burgers vector normal to the terrace planes for both types of disconnection. This component, b_z, is $\pm\left(\sqrt{3}a_{cub} - \frac{c_{hex}}{3}\right)$ for the 6/5 disconnections and $\pm\left(\frac{5a_{cub}}{sqrt3} - \frac{2c_{hex}}{3}\right)$ for the 10/10 disconnections.

It is also instructive to compare the dislocation components lying parallel with the terrace plane ($\mathbf{b}_{||}$). For the 6/5 disconnections, $\mathbf{b}_{||}$ is of type $\frac{1}{6}\langle 121 \rangle$, which is analogous to a Shockley partial dislocation. In contrast, for the 10/10 disconnections, $\mathbf{b}_{||}$ is of type $\frac{1}{2}\langle 110 \rangle$, which is the same as a crystal lattice dislocation in the rocksalt phase. The orientation of $\mathbf{b}_{||}$ also can be distinguished. Taking the defect line direction to lie normal to the page (i.e. along $[\bar{1}01]//[\bar{2}110]$), we see that for the +6/+5 and +5/+6 disconnections, $\mathbf{b}_{||}$ is oriented at 90° with respect to the line direction (i.e. $b_x = 0$), whereas for the -6/-5 and -5/-6 disconnections, it is oriented at ±30° (i.e. $b_x = \pm a_{cub}/2\sqrt{2}$). In contrast, $\mathbf{b}_{||}$ is oriented at ±60° with respect to the line direction (i.e. $b_x = \pm a_{cub}\sqrt{2}/4$) for all of the 10/10 disconnections considered. These distinctions will be useful later in our discussion of

Table D.1: Summary of defect parameters.

Type	$\mathbf{t}_\lambda$	$\mathbf{t}_\mu$	$\mathbf{b}_\parallel$ (λ, a_{cub})	b_x ($a_{cub}/2\sqrt{2}$)	b_y $\left(a_{cub}/\sqrt{6}\right)$	b_z ($\sqrt{3}a_{cub} - \frac{a_{hex}}{3}$)
(a) $\lambda = 6/\mu = 5$						
λ/μ +6/+5	$[111]$	$\frac{1}{3}[\bar{1}\bar{2}1](\frac{1}{3}[0\bar{1}11])$	$\frac{1}{6}[\bar{1}21]$	0	$-1(-0.264$ nm$)$	$+1(+0.104$ nm$)$
λ/μ -6/-5	$[\bar{1}\bar{1}\bar{1}]$	$\frac{1}{3}[1\bar{1}\bar{1}](\frac{1}{3}[1\bar{1}01])$	$\frac{1}{6}[\bar{2}11]$	$+1(+0.228$ nm$)$	$-1/2(-0.132$ nm$)$	$-1(-0.104$ nm$)$
		$\frac{1}{3}[\bar{2}\bar{1}\bar{1}](\frac{1}{3}[\bar{1}01\bar{1}])$	$\frac{1}{6}[11\bar{2}]$	$-1(-0.228$ nm$)$	$-1/2(-0.132$ nm$)$	
μ/λ -5/-6	$[111]$	$\frac{1}{3}[\bar{1}11](\frac{1}{3}[\bar{1}101])$	$\frac{1}{6}[2\bar{1}\bar{1}]$	$-1(-0.228$ nm$)$	$+1/2(+0.132$ nm$)$	$+1(+0.104$ nm$)$
		$\frac{1}{3}[211](\frac{1}{3}[10\bar{1}1])$	$\frac{1}{6}[\bar{1}\bar{1}2]$	$+1(+0.228$ nm$)$	$+1/2(+0.132$ nm$)$	
μ/λ +5/+6	$[\bar{1}\bar{1}\bar{1}]$	$\frac{1}{3}[12\bar{1}](\frac{1}{3}[01\bar{1}\bar{1}])$	$\frac{1}{6}[1\bar{2}1]$	0	$+1(+0.264$ nm$)$	$-1(-0.104$ nm$)$

Type	$\mathbf{t}_\lambda$	$\mathbf{t}_\mu$	$\mathbf{b}_\parallel$ (λ, a_{cub})	b_x $\left(a_{cub}/2\sqrt{2}\right)$	b_y $\left(a_{cub}/\sqrt{6}\right)$	b_z $\left(\frac{5a_{cub}}{\sqrt{3}} - \frac{2}{3}c_{hex}\right)$
(b) $\lambda = 10/\mu = 10$						
λ/μ +10/+10	$\frac{1}{2}[334]$	$\frac{2}{3}[\bar{1}\bar{2}1](\frac{2}{3}[0\bar{1}11])$	$\frac{1}{2}[\bar{1}10]$	$+1(+0.228$ nm$)$	$-3/2(-0.396$ nm$)$	$+1(-0.165$ nm$)$
	$\frac{1}{2}[443]$	$\frac{2}{3}[\bar{1}\bar{2}1](\frac{2}{3}[0\bar{1}11])$	$\frac{1}{2}[01\bar{1}]$	$-1(-0.228$ nm$)$	$-3/2(-0.396$ nm$)$	$+1(-0.165$ nm$)$
λ/μ -10/-10	$\frac{1}{2}[\bar{3}\bar{3}\bar{4}]$	$\frac{1}{3}[\bar{1}\bar{2}\bar{2}](\frac{1}{3}[0\bar{1}1\bar{2}])$	$\frac{1}{2}[01\bar{1}]$	$-1(-0.228$ nm$)$	$-3/2(-0.396$ nm$)$	$-1(+0.165$ nm$)$
	$\frac{1}{2}[\bar{4}\bar{3}\bar{3}]$	$\frac{1}{3}[\bar{1}\bar{2}\bar{2}](\frac{1}{3}[0\bar{1}1\bar{2}])$	$\frac{1}{2}[\bar{1}10]$	$+1(+0.228$ nm$)$	$-3/2(-0.396$ nm$)$	$-1(+0.165$ nm$)$
μ/λ -10/-10	$\frac{1}{2}[334]$	$\frac{1}{3}[122](\frac{1}{3}[01\bar{1}2])$	$\frac{1}{2}[0\bar{1}1]$	$+1(+0.228$ nm$)$	$+3/2(+0.396$ nm$)$	$+1(-0.165$ nm$)$
	$\frac{1}{2}[433]$	$\frac{1}{3}[122](\frac{1}{3}[01\bar{1}2])$	$\frac{1}{2}[1\bar{1}0]$	$-1(-0.228$ nm$)$	$+3/2(+0.396$ nm$)$	$+1(-0.165$ nm$)$
μ/λ +10/+10	$\frac{1}{2}[\bar{3}\bar{3}\bar{4}]$	$\frac{1}{2}[12\bar{1}](\frac{1}{2}[01\bar{1}\bar{1}])$	$\frac{1}{2}[1\bar{1}0]$	$-1(-0.228$ nm$)$	$+3/2(+0.396$ nm$)$	$-1(-0.165$ nm$)$
	$\frac{1}{2}[\bar{3}\bar{3}\bar{4}]$	$\frac{2}{3}[12\bar{1}](\frac{2}{3}[01\bar{1}\bar{1}])$	$\frac{1}{2}[0\bar{1}1]$	$+1(+0.228$ nm$)$	$+3/2(+0.396$ nm$)$	$-1(-0.165$ nm$)$

the roles these defects play in the phase transformation and accommodation of interface coherency strain.

The 6/5 type disconnections are of particular interest because of their proposed role in the rocksalt/tetradymite phase transformation [72]. The tetradymite structure can be generated from the rocksalt phase by removing every sixth metal plane (marked by arrows in Fig. D.1) and appropriately shearing the crystal to restore the ABC-type stacking sequence of the adjacent close-packed planes [201]. As illustrated in Fig. D.4, lateral motion of a 6/5 defect can accomplish these actions as follows: climb of the perpendicular dislocation component of the defect removes a metal plane, forming a double tellurium layer, while glide of the parallel dislocation component, which is of type $\frac{1}{6}\langle 121\rangle$, restores the crystal stacking across the interface [72]. In this mechanism, then, the tellurium sublattice remains intact, but chemical exchange must occur on the metal sublattice to maintain the correct stoichiometry.

D.3 Experimental methods

The material for this study was prepared by annealing a Pb-Sb-Te alloy to form a distribution of Sb_2Te_3 precipitates within a matrix of PbTe. Based on the phase diagram for the pseudo-binary $(PbTe)_{1-x}(Sb_2Te_3)_x$ system [12], we chose a composition of x = 0.060 (i.e. 5.5 at. % Sb) to allow the formation of Sb_2Te_3 precipitates by annealing in the two-phase $PbTeSb_2Te_3$ field following a suitable homogenization solution anneal at higher temperatures in the single-phase rocksalt PbTe field. Appropriate amounts of Pb, Sb, and Te elemental starting materials were loaded into a fused silica ampoule, which was then vacuum-sealed, and backfilled to a pressure of 3.4×10^4 Pa with Ar. The ampoule was placed in a resistive furnace at 1000°C for 10 min to melt the material and then cooled in air to room temperature. The sample was solution annealed at 570°C for 7 days to

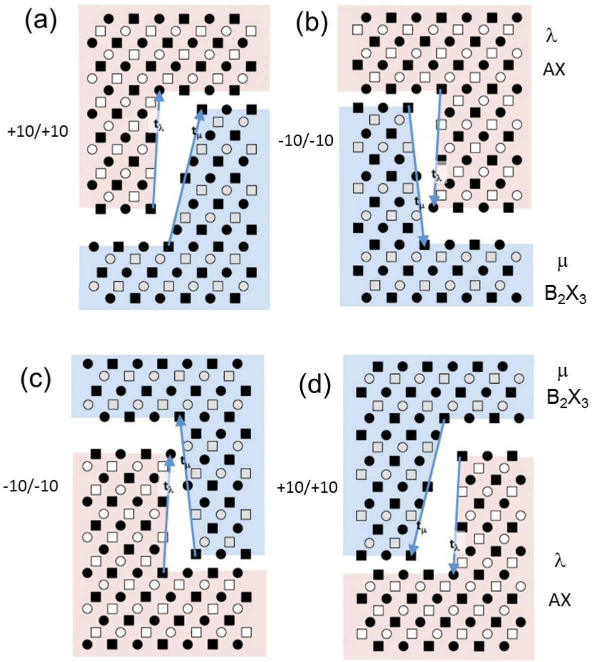

Figure D.3: Schematics of the set of 10/10-type disconnections obtained from combinations of $\mathbf{t}(\lambda) = \frac{1}{2}\langle 334\rangle$ and $\mathbf{t}(\mu) = \frac{2}{3}\langle 0\bar{1}11\rangle$ or $\frac{1}{3}\langle 01\bar{1}2\rangle$. Each defect corresponds to a step of ±10 close-packed planes in the rocksalt (λ) and tetradymite (μ) phases. The geometric specifications for these defects are shown in Table D.1b.

homogenize the sample and then annealed at 450°C for 1 h to form the Sb_2Te_3 precipitates. Both the homogenization anneal and the precipitation anneal were terminated by water quenching.

Specimens were prepared for TEM analysis by mechanical polishing and dimpling, followed by argon ion milling (Fischione 1010 ion mill) to achieve final electron transparency. To reduce the possibility of beam damage during this process, the stage of the ion mill was cooled to below -100°C using liquid nitrogen. All HRTEM imaging and diffraction measurements were conducted on a JEOL 4000EX microscope operated at 400 kV.

D.4 Experimental obsevations

D.4.1 Orientation and morphology

The TEM observations showed the presence of nanometer scale Sb_2Te_3 precipitates, crystallographically aligned with the PbTe matrix. An example of the microstructure is shown in Fig. D.5. The precipitates exhibit an elongated, plate-like morphology. Analysis of selected-area electron diffraction patterns (Fig. D.6) confirms that the precipitates are aligned with $\{111\}_{\mathrm{PbTe}} \parallel (0001)_{\mathrm{Sb2Te3}}$ and $\langle\bar{1}01\rangle_{\mathrm{PbTe}} \parallel \langle\bar{2}110\rangle_{\mathrm{Sb2Te3}}$, and that the precipitates are elongated parallel to the (0001)Sb_2Te_3 planes. Since there are four sets of {111} planes in a cubic structure, the precipitates can form

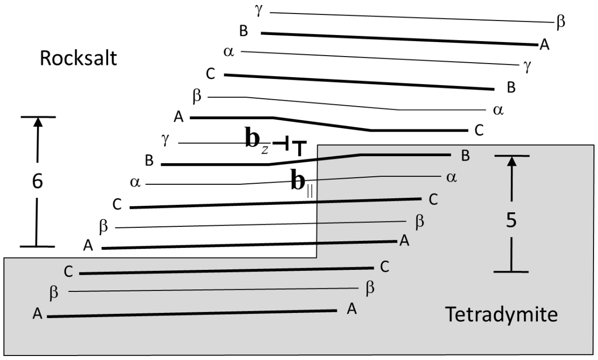

Figure D.4: Growth of tetradymite plates can occur by the motion of interfacial disconnections. In this schematic, motion of the +6/+5 disconnection to the left thickens the tetradymite plate by one 5-plane thick unit. Here, $\mathbf{b}_z$ removes a metal plane (labeled c), while $\mathbf{b}_{||}$ shears the resulting double chalcogenide layer (labeled B, C) into the correct stacking. Adapted from Ref. [72].

in four crystallographically equivalent orientation variants and habit plane alignments. In a TEM specimen with the matrix oriented along a $\langle 110 \rangle$-type direction (as in Figs. D.5 and D.6), two of the Sb_2Te_3 variants are oriented edge-on, while the remaining two are inclined with respect to the imaging direction. These results confirm previous analyses of the crystallographic orientations of Sb_2Te_3 plates in PbTe deduced from electron backscattered diffraction (EBSD) measurements of this system [186]. The tips of a number of the precipitates show a marked offset away from the mid-plane of the precipitate, and in some cases, such as the left precipitate in Fig. D.6a, this morphology is inverted across the two ends of the precipitate, as would be expected.

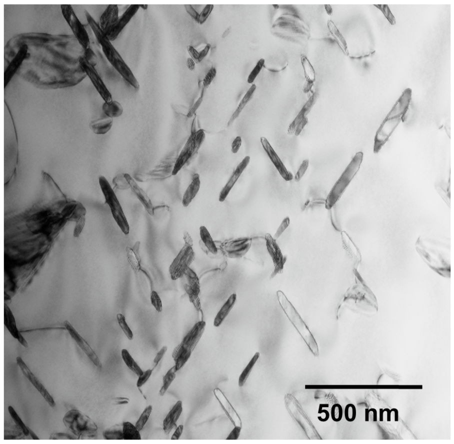

Figure D.5: Bright-field TEM micrograph showing Sb_2Te_3 precipitates in the PbTe matrix.

Through HRTEM observations we identified numerous defects at the PbTe/Sb_2Te_3 interfaces. Near the middle of the precipitates, where the inclination is close to $\{111\}_{PbTe}\|(0001)_{Sb2Te3}$, we observed both dislocations (with no steps), as well as some interfacial steps or disconnections. An example is shown in Fig. D.7. The density of interfacial steps is higher near the ends of the precipitates, where there is a more significant departure from the general $\{111\}_{PbTe}\|(0001)_{Sb2Te3}$ interfacial inclination (Fig. D.8). In the subsequent analysis, we concentrate on the regions of interface indicated by the white line on the upper (a) and lower (b) sides of the precipitate in Fig. D.8. Enlargements of these regions, showing arrays of closely spaced $\{111\}_{PbTe}\|(0001)_{Sb2Te3}$ terraces, are shown in Fig. D.9a and b.

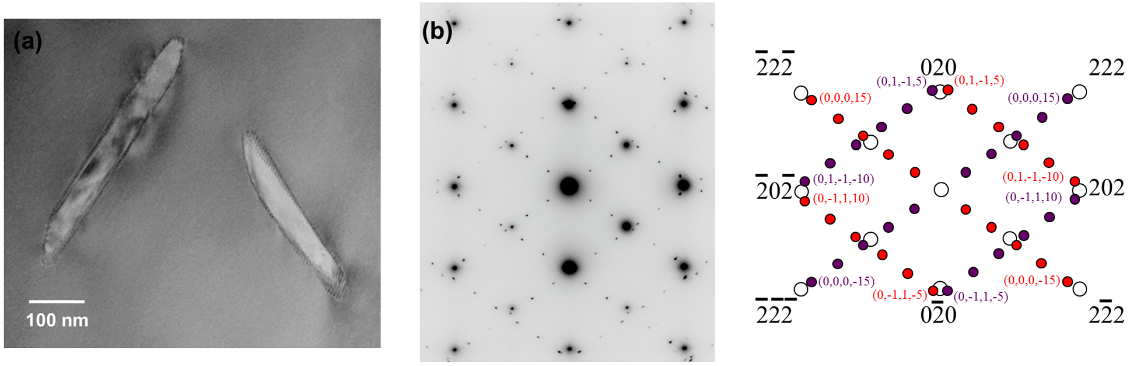

Figure D.6: (a) TEM micrograph showing two Sb_2Te_3 precipitates. Note the offset of the tips of the precipitates away from the mid-plane of the precipitate. The inversion of the tip morphology for the two ends of the left precipitate is consistent with the shared $\overline{3}m$ symmetry of the two crystals. (b) The electron diffraction pattern from these precipitates confirms the orientation relationship discussed in the text. In the indexed schematic the Sb_2Te_3 patterns are indicated by red and blue circles; PbTe is indicated by open circles.

D.4.2 Defect analysis

We analyzed the dislocation content of the observed defects by circuit mapping procedures using the formalism developed by Pond and Hirth [193, 202]. Experimentally, the Burgers vector of an interfacial defect can be determined from an atomic-resolution image by constructing a closed-loop circuit around the image of the defect and calculating the closure-failure in a perfect, bicrystalline reference frame, using the expression:

$$\mathbf{b} = -[\mathbf{C}(\lambda) + \mathbf{P}\mathbf{C}(\mu)], \tag{D.3}$$

where $\mathbf{C}(\lambda)$ and $\mathbf{C}(\mu)$ are the segments of a circuit path in the two crystals, λ (PbTe) and μ (Sb_2Te_3), and $\mathbf{P}$, as given above in Eq. D.2, is a transformation matrix that converts vectors from the μ crystal coordinate system to that of λ. The interface crossings occur at crystallographically equivalent locations.

To illustrate, Fig. D.7b shows a circuit constructed around one of the defects along the flat section of the interface shown in Fig. D.7a. The analysis shows that this defect, as well as the other dislocations in this image, marked by arrows, have Burgers vector of type $\frac{1}{2}\langle 110\rangle$, specifically

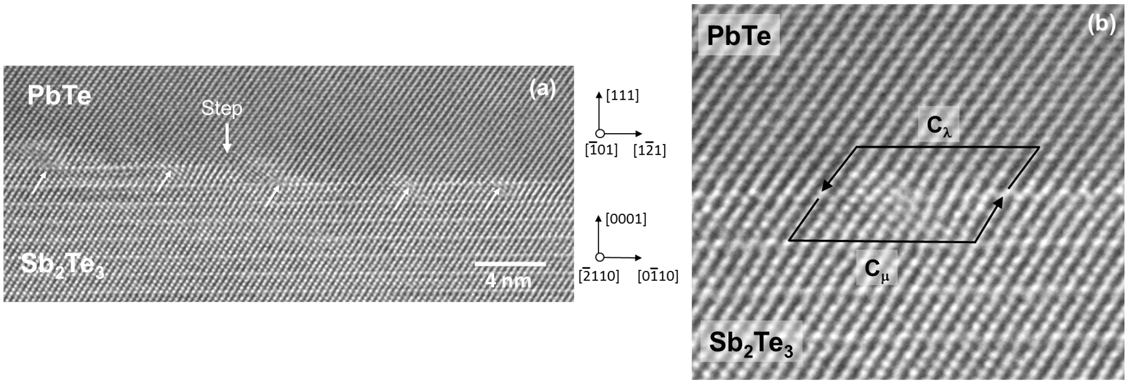

Figure D.7: (a) HRTEM micrograph taken from the middle region of a precipitate showing a step and several interfacial dislocations (indicated by arrows). The dislocations are of type $\frac{1}{2}\langle 110\rangle$ and the step is identified as a -5/-6 disconnection. (b) Circuit analysis of one of the interfacial dislocations with no step. Here, $C(\lambda) = 10 * \frac{1}{4}[\bar{1}2\bar{1}]$ and $C(\mu) = 11 * \frac{1}{2}[\bar{1}\bar{2}0] \pm [100](11 * \frac{1}{2}[0\bar{1}10] \pm \frac{1}{6}[2\bar{1}\bar{1}0]$ in 4-index notation) giving $\mathbf{b} = \frac{1}{2}[\bar{1}10]$ or $\frac{1}{2}[01\bar{1}]$ from Eq. D.3.

$\frac{1}{2}[\bar{1}10]$ or $\frac{1}{2}[01\bar{1}]$. The two possibilities arise because of the ambiguity of determining the sign of the dislocation screw component since that lies along the imaging direction. In either case, the edge component is $\frac{1}{4}[\bar{1}2\bar{1}]$ (i.e. $b_y = -3a_{cub}/2\sqrt{6}$). These defects are of the correct sign, and, as we discuss below, are spaced close to the expected distance required to accommodate the misfit strain on flat $\{111\}_{\mathrm{PbTe}}/(0001)_{\mathrm{Sb2Te3}}$ terraces. Through similar analyses, the step in Fig. D.7a was identified as a -6/-5 disconnection.

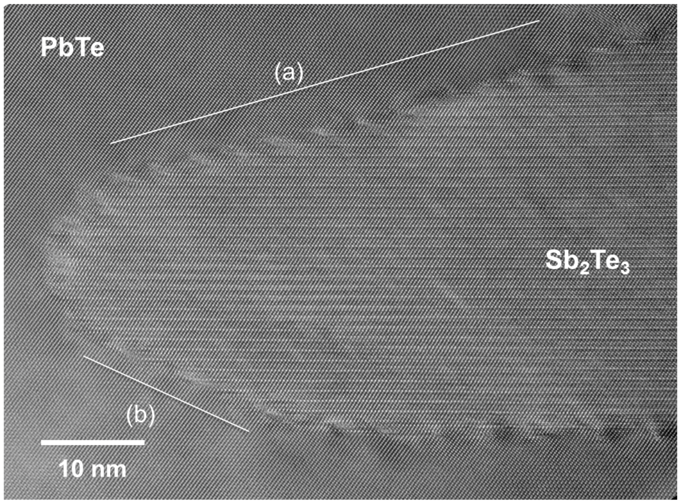

Figure D.8: HRTEM image of Sb_2Te_3 precipitate taken near the tip of a precipitate. Enlargements of regions (a and b), indicated by the white lines, are presented in Fig. D.9.

We focused in particular on analyzing the defects near the leading edge of the precipitates. Fig. D.10 illustrates a circuit constructed around one of the disconnections observed along section (a) of the interface of Figs. D.8 and D.9a. This defect is a +6/+5 disconnection (i.e. consisting of a step that is 6 close-packed planes high in the PbTe crystal and 5 high in the Sb_2Te_3 crystal), and is topologically equivalent to the interfacial disconnection observed previously at a {111}/(0001) interface in the $AgSbTe_2/Sb_2Te_3$ system [72].

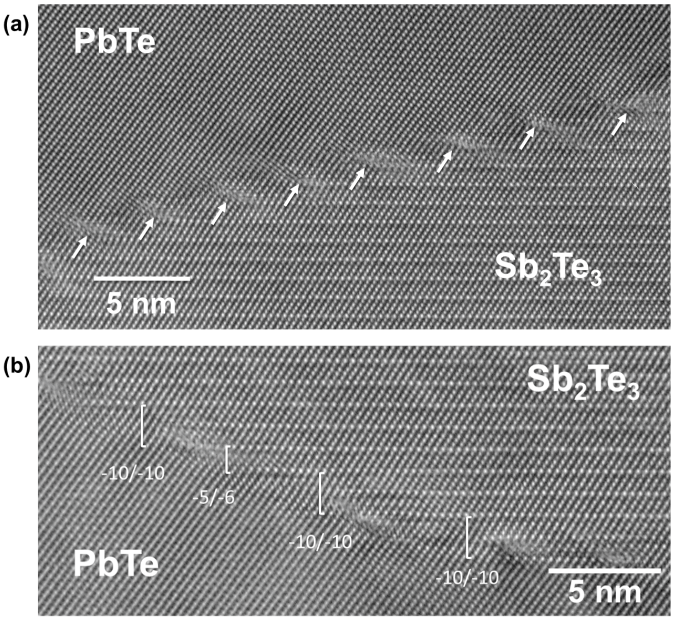

Figure D.9: (a) Array of +6/+5 disconnections separating $(111)_{PbTe}/(0001)_{Sb2Te3}$ terraces along region (a) from Fig. D.8. The arrows indicate the positions of the dislocation cores of these defects. (b) Three -10/-10 disconnections and a -5/-6 disconnection along region (b) of Fig. D.8.

We identified 13 defect cores over section (a) of the interface indicated on Fig. D.8. The positions of the defects are plotted in Fig. D.11. Circuit analyses showed that all but one of these defects were +6/+5 disconnections. The remaining defect was identified as a +10/+10 disconnection.

That an array of +6/+5 disconnections should be present near the tip of the advancing Sb_2Te_3 precipitate is consistent with the proposed role for this defect in the growth of tetradymite precipitates in rocksalt chalcogenides [72], as discussed above in Section D.4.2. It is interesting, therefore, to compare the structures of the interface on the upper and lower sides of the leading edge of the precipitate (i.e. regions (a) and (b) of Fig. D.8). Given the well-ordered array of +6/+5 disconnections on the upper interface one might anticipate a similar arrangement of the complementary -5/-6 disconnections on the lower interface. However, analysis of the defects observed in region (b) of Fig. D.8 (enlarged in Fig. D.9b) shows a more complex situation. Although a -5/-6 disconnection is observed, several -10/-10 disconnections are also present. As we discuss below, this difference in selection of defect structure for the upper and lower leading edges of the precipitate may reflect the relative efficiency of the different possible defects in accommodating the interfacial misfit strain.

D.5 Discussion

D.5.1 Relationship of the interfacial disconnections to the misfit strain

The misfit across {111}/000 1 terraces is quite large for the PbTe/Sb_2Te_3 system. Taking the coherency strain, ϵ_{coh}, as that required to match nearest-neighbor distances within $\{111\}_{PbTe}/\{0001\}_{Sb2Te3}$ terraces gives $\epsilon_{coh} = (a_{hex}\sqrt{2}/a_{cub} - 1) = 0.0668$, or $\sim 6.7\%$. Along a flat interface, without steps, the coherency strain can be accommodated by an array of misfit dislocations spaced at a separation, L, such that the edge component of their in-plane Burgers vector cancels the coherency strain (e.g. L = -b_y/ϵ_{coh}). The edge component, b_y, of a 60° $\frac{1}{2}\langle 110\rangle$ dislocation is 0.396 nm, giving an expected spacing of 6 nm, which is comparable to the defect spacing observed in Fig. D.7, which ranges from 5 to 7 nm.

Similarly, the spacing of the interfacial disconnections should also be related to the misfit strain since they too possess dislocation content. However, a regularly spaced array of disconnections will also change the average inclination of the interface since each defect introduces a step. The resulting inclination angle, h, can be obtained by solving [199, 203]:

$$-\epsilon_{coh} = (b_y \tan\theta + b_z \tan^2\theta)h^{-1}. \tag{D.4}$$

In this expression, b_y and b_z are the Burgers vector components parallel and perpendicular to the terrace, and h is the smaller of the step heights in the two crystals. In this expression, the defects are spaced to fully cancel the coherency strain projected onto the inclined interface plane.

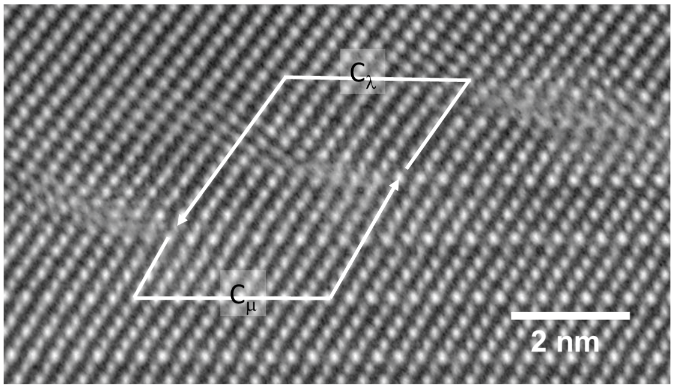

Figure D.10: Example of a circuit path used to characterize the Burgers vectors of the interfacial disconnections. $C(\lambda) = \frac{1}{2}[\bar{7}8\bar{7}]$ and $C(\mu) = \frac{1}{3}[\overline{16}, \overline{32}, 1]$ giving **b** and step heights consistent with a +6/+5 disconnection as described in Table D.1a.

Taking the parameters for an array of +6/+5 disconnections (i.e. b_y = -0.264 nm, b_z = 0.104 nm and $h = h_\mu$ = 1.015 nm), with ϵ_{coh} = +0.0668, predicts an interface inclination angle of 16.2°. We can compare this prediction with the angle measured from region (a) of Fig. D.8, which we determined by fitting a line to the marked defect coordinates (see Fig. D.11). (The +10/+10 disconnection, which is indicated by an open circle, marks a departure from linearity on this plot.) This measurement gives an interface inclination angle, h, of 14.8° relative to the {0001} planes of the Sb_2Te_3 crystal, which is in reasonable agreement with the value predicted from Eq. (D.4).

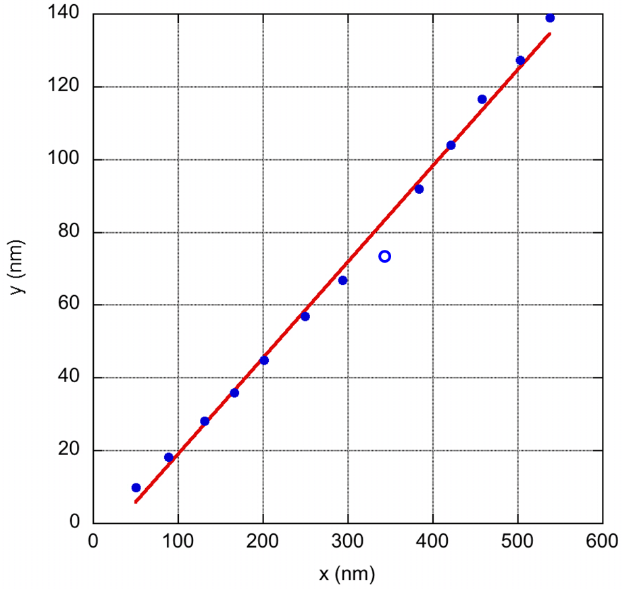

Figure D.11: Positions of the defect cores along the length of interface indicated as (a) in Fig. D.8. The regularly spaced array of steps inclines the interface in this region by 14.8° from the $(111)_{PbTe}/(0001)_{Sb2Te3}$ inclination, as determined from the slope of this plot. The filled dots are the positions of +6/+5 disconnections. The open circle was identified as a +10/+10 disconnection.

Additionally, residual dislocation content perpendicular to the inclined interface plane will rotate the crystals away from the reference orientation (in a manner analogous to the rotation at a wall of edge dislocations at a low-angle tilt boundary). This tilt angle can be calculated from [203]:

$$\phi = 2\sin^{-1}[(b_z\cos\theta - b_y\sin\theta - \epsilon_{coh}h\cos\theta)\sin\theta/2h]. \tag{D.5}$$

Again using the parameters for an array of +6/+5 disconnections, this expression gives a value of $\phi = +1.64°$, representing a clockwise rotation of the PbTe crystal relative to the Sb_2Te_3 crystal. Experimentally, from the orientation of the lattice fringes, we measure a rotation of $\phi = 1.2 \pm 0.5°$, also in the clockwise direction. These results for θ and ϕ show that the arrangement of the +6/+5 defects is close to that required for these defects to fully accommodate the interfacial coherency strain.

As we noted in Section D.4.2, it is somewhat surprising that an analogous array of -5/-6 disconnections is not observed on the lower side of the precipitates leading edge (region (b) of Fig. D.8). Instead, several -10/-10 disconnections are observed. Consideration of the accommodation of misfit

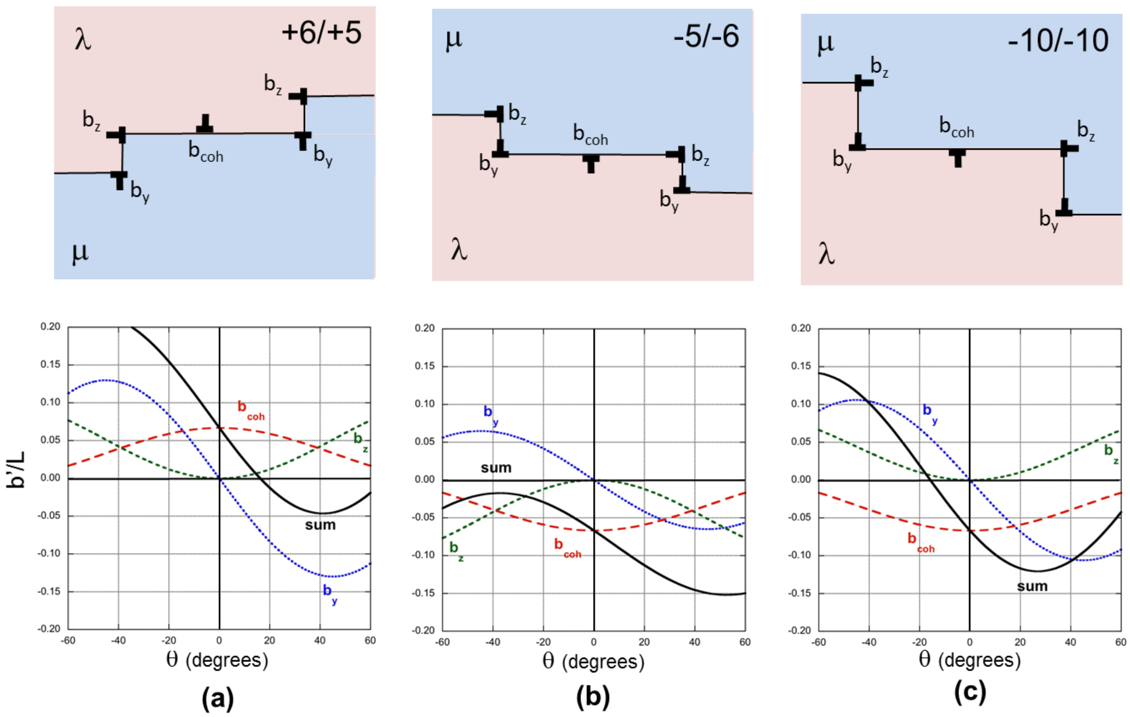

(a) (b) (c)

Figure D.12: Burgers vector density projected onto the average habit plane as a function of the inclination angle for arrays of disconnections in the PbTe/Sb_2Te_3 system. The blue and green curves show the projected values of b_y and b_z, respectively (normalized per unit interface length). The coherency strain on the terraces is represented by b_{coh} indicated in red. For an array of +6/+5 disconnections (a), these dislocation components cancel at an interface inclination angle of 16.2°. The magnitude of b_y is smaller for the -5/-6 disconnections (b). In this case, the increasing component of b_z projected onto the more steeply inclined interface offsets the small magnitude of b_y so that the components never fully cancel. In contrast, -10/-10 disconnections (c) can accommodate the misfit strain because of their larger b_y.

strain suggests a solution to this quandary. Although the magnitudes of the step heights for the +6/+5 and -5/-6 disconnections are the same, the magnitude of the dislocation edge component in the terrace plane (b_y) of a -5/-6 disconnection is only half that of a +6/+5 disconnection because $\mathbf{b}_{\|}$ is oriented at 30° to the defect line direction, which we assume is aligned with the imaging direction. Thus, the -5/-6 disconnections will be less efficient at accommodating the interfacial misfit than the pure edge +6/+5 disconnections we observed along region (a).

Indeed, from Eq. D.4, an array consisting solely of this type of disconnection cannot accommodate the large misfit of the PbTe/Sb_2Te_3 system. The reason is that as the defect spacing is decreased to compensate the coherency strain, the increasing component of b_z projected onto the more steeply inclined interface offsets the small magnitude of b_y. This effect can be seen in Fig. D.12, which plots these projected components as a function of interface inclination angle for arrays of +6/+5 and -5/-6 disconnections. Whereas the +6/+5 disconnections cancel the coherency strain projected onto the inclined interface at an angle of 16.2° (Fig. D.12a) (as given by Eq. D.4 above), there is no inclination angle for which all the components cancel for an array of -5/-6 disconnections (Fig. D.12b). In contrast, because the edge component of the -10/-10 disconnections is much larger, these defects can play a more effective role in accommodating the misfit. Fig. D.12c plots the projected dislocation components for an array of -10/-10 disconnections ($b_y = +0.396$ nm, $b_z = -0.165$ nm, $h = h_k = -1.865$ nm, and $\epsilon_{coh} = -0.0668$). In this case, the array cancels the coherency strain at an inclination angle of -15.7°.

It is conceivable that +6/+5 and -5/-6 disconnections may initially play analogous roles in the transformation from the rocksalt to tetradymite phase at both the upper and lower interfaces. However, in systems such as PbTe/$\mathrm{Sb_2Te_3}$ that have large misfit, development of a stable, extended array of the -5/-6 disconnections is unlikely as this would result in large, uncompensated strains. Instead, these defects would need to convert to a more efficient configuration, such as an array of -10/-10 disconnections, to relieve these strains. Differences in the elastic interactions of evolving defect arrays as well as in the kinetic processes by which they evolve could account for the asymmetry in tip morphology that we observe in a number of the precipitates. An additional consideration is that in the three dimensional precipitate, we would anticipate the interfacial defects to be arrayed in a network with multiple line directions consistent with the interfacial symmetry. Further work quantifying the shape distributions of precipitates in this system and the arrangement of the defect line directions within the interface plane would help to clarify these issues.

D.5.2 Nucleation of new tetradymite layers

Finally, we consider how new disconnections might be generated to nucleate new tetradymite layers. Evidence suggesting a mechanism is found in the HRTEM image shown in Fig. D.13. This image was taken from a region of precipitate away from the growing tip. Here, several contrast features that appear to be alternating up and down steps are indicated. Circuit analysis on one of the clearer features (Fig. D.13b) shows that these are alternating up (+6/+5) and down (-6/-5) disconnections. Since the step heights of the adjacent disconnections cancel, the average interface inclination of this section of interface is parallel with $\{111\}_{PbTe}/(0001)_{Sb2Te3}$. Similarly, the perpendicular component of the dislocation content (b_z) of the adjacent pairs also cancels. In contrast, the dislocation content parallel to the interface remains finite. Summing $\mathbf{b}_{\|}$ for the adjacent +6/+5 and -6/-5 disconnections (see Table D.1), gives (in the rocksalt coordinate frame) total Burgers vectors of:

$$\frac{1}{6}[\bar{1}2\bar{1}] + \frac{1}{6}[\bar{2}11] = \frac{1}{2}[\bar{1}10] \text{ or } \frac{1}{6}[\bar{1}2\bar{1}] + \frac{1}{6}[11\bar{2}] = \frac{1}{2}[01\bar{1}], \tag{D.6}$$

depending on the sign of the defect component along the imaging direction. These total Burgers vectors are equivalent to perfect crystal lattice translation vectors in the rocksalt crystal.

From the above observations we can speculate on the processes involved in the nucleation of new

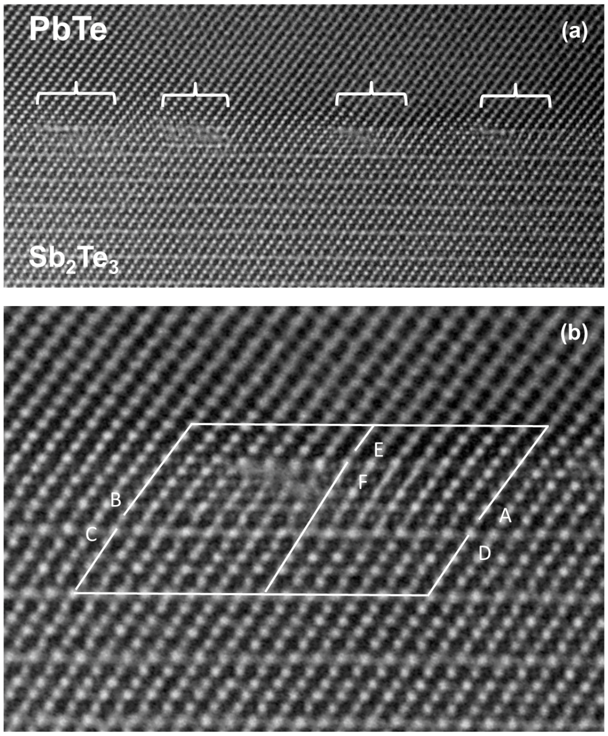

Figure D.13: (a) Alternating up and down steps at a section of the PbTe/Sb_2Te_3 interface away from tip region. (b) Circuit analysis shows that the up step ($\mathbf{C}(\lambda) = \mathbf{EB}$, $\mathbf{C}(\mu) = \mathbf{CF}$) is a +6/+5 disconnection and the down step ($\mathbf{C}(\lambda) = \mathbf{AE}$ and $\mathbf{C}(\mu) = \mathbf{FD}$) is a -6/-5 disconnection. Circuit analysis around the entire defect ($\mathbf{C}(\lambda) = \mathbf{AB}$, $\mathbf{C}(\mu) = \mathbf{CD}$) gives a Burgers vector of $\frac{1}{2}[\bar{1}10]$ or $\frac{1}{2}[01\bar{1}]$, consistent with a crystal lattice dislocation.

tetradymite layers, as illustrated schematically in Fig. D.14. We know that in general the Sb_2Te_3 precipitates are elongated along $\{11\ 1\}_{PbTe}/(0001)_{Sb2Te3}$. To maintain this average inclination the net step content must be zero; yet defects are still required to accommodate the misfit strain. The misfit along flat sections of the elongated $\{111\}_{PbTe}/(0001)_{Sb2Te3}$ precipitate interface can be accommodated by arrays of $\frac{1}{2}\langle 110\rangle$ type crystal lattice dislocations, since if compact, such defects have no step associated with them. However, dissociation of these crystal lattice dislocations into paired +6/+5 and -6/-5 disconnections, as described in Eq. (D.6), would form complementary up and down steps forming the nuclei for a new Sb_2Te_3 layer. In this view, growth of the new layer would proceed by the motion of these disconnections along the $\{111\}_{PbTe}/(0001)_{Sb2Te3}$ interface. As the complementary +6/+5 and -6/-5 disconnections meet, their step components would annihilate, completing a new layer of the tetradymite phase, while their net dislocation content would be retained, as required to accommodate the interfacial misfit. In contrast, at the ends of the new layer, the terminating disconnections would have no counterparts with which to annihilate and thus would be incorporated into the evolving tip of the advancing precipitate. Here, the pure edge-type disconnections (such as the +6/+5 disconnections we have observed) could accommodate the misfit strain on this section of interface, but further rearrangements would be required to convert the mixed character disconnections (such as the -6/-5 defects) to more stable configurations, such as the -10/-10 disconnections we have observed.

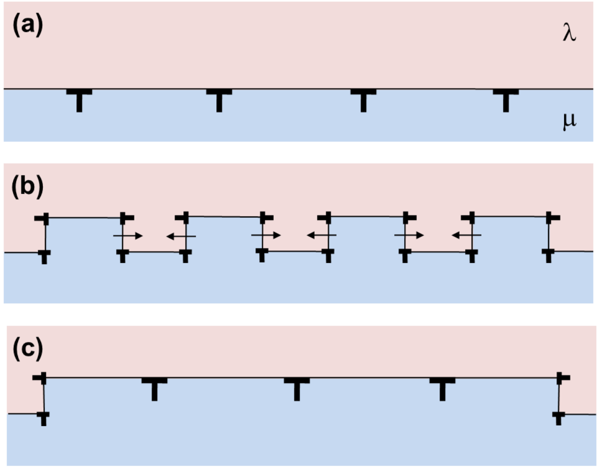

Figure D.14: Proposed step nucleation mechanism. (a) Array of $\frac{1}{2}\langle 110\rangle$ lattice dislocations accommodates the misfit strain along flat sections of $\{111\}_{PbTe}/\{0001\}_{Sb2Te3}$ interface. (b) Dissociation of the $\frac{1}{2}\langle 110\rangle$ dislocations into paired +6/+5 and -6/-5 disconnections, forming initial steps in the interface. These disconnections move laterally and eventually combine with their oppositely signed counterparts. (c) The step and b_z components annihilate, but the $\mathbf{b}_{||}$ components add vectorially to form a new set of $\frac{1}{2}\langle 110\rangle$ dislocations in the translated interface. The remaining disconnections at the ends of the interface are incorporated into the growing tip of the precipitate.

D.6 Conclusions

Our observations highlight the important roles that interfacial line defects can play in the growth of tetradymite plates in rocksalt-structured chalcogenides. In summary, the presence of numerous interfacial +6/+5 type disconnections near the tip of a Sb_2Te_3 plate in PbTe is consistent with the notion that the atomic mechanism for growth of tetradymite plates in rocksalt chalcogenides involves the motion of such step-like defects. Moreover, the arrangement of these defects is consistent with that required to accommodate the rather large misfit strain in the PbTe/Sb_2Te_3 system. The role of these defects in accommodating strain suggests that they cannot move independently, but rather must be coupled to each other through this strain interaction. Our observations also suggest a mechanism for the nucleation of new tetradymite layers. New layers could form by the decomposition of crystal lattice dislocations, present to accommodate misfit on flat regions of interface, into pairs of complementary disconnections with oppositely signed steps. In this view, then, the morphology of the evolving precipitates, both in terms of their macroscopic shape and their local, nanometer-scale roughness, should be sensitively tied to the kinetics of the step nucleation and motion as well as to the interfacial misfit, since the misfit will control the density of interfacial defects.

Interfacial line defects such as we have identified and analyzed here provide the elementary building blocks for constructing higher-level models for interfacial structure and properties. Ultimately, the electronic and thermal transport processes that govern energy conversion efficiency in nanostructured thermoelectric materials are tied to the structure, morphology and strain state of the internal interfaces. Further work exploring the defect mechanisms at such interfaces should be fruitful in yielding improved routes for controlling interfaces for advanced thermoelectric nanocomposites.

Bibliography

[1] B. A. Smith, L. Soderblom, R. Beebe, J. Boyce, G. Briggs, A. Bunker, S. A. Collins, C. J. Hansen, T. V. Johnson, J. L. Mitchell, R. J. Terrile, M. Carr, A. F. Cook, J. Cuzzi, J. B. Pollack, G. E. Danielson, A. Ingersoll, M. E. Davies, G. E. Hunt, H. Masursky, E. Shoemaker, D. Morrison, T. Owen, C. Sagan, J. Veverka, R. Strom, and V. E. Suomi. Encounter with Saturn - Voyager-1 imaging science results. *Science*, 212(4491):163–191, 1981.

[2] B. A. Smith, L. Soderblom, R. Batson, P. Bridges, J. Inge, H. Masursky, E. Shoemaker, R. Beebe, J. Boyce, G. Briggs, A. Bunker, S. A. Collins, C. J. Hansen, T. V. Johnson, J. L. Mitchell, R. J. Terrile, A. F. Cook, J. Cuzzi, J. B. Pollack, G. E. Danielson, A. Ingersoll, M. E. Davies, G. E. Hunt, D. Morrison, T. Owen, C. Sagan, J. Veverka, R. Strom, and V. E. Suomi. A new look at the Saturn system - the Voyager-2 images. *Science*, 215(4532):504–537, 1982.

[3] S. K. Yee, S. LeBlanc, K. E. Goodson, and C. Dames. $ per W metrics for thermoelectric power generation: beyond ZT. *Energy & Environmental Science*, 6(9):2561–2571, Sept 2013.

[4] G. J. Snyder, E. S. Toberer, R. Khanna, and W. Seifert. Improved thermoelectric cooling based on the Thomson effect. *Physical Review B*, 86(4), July 2012.

[5] J. M. O. Zide, D. Vashaee, Z. X. Bian, G. Zeng, J. E. Bowers, A. Shakouri, and A. C. Gossard. Demonstration of electron filtering to increase the Seebeck coefficient in $\mathrm{In_{0.53}Ga_{0.47}As/In_{0.53}Ga_{0.28}Al_{0.19}As}$ superlattices. *Physical Review B*, 74(20), Nov 2006.

[6] J. P. Heremans, V. Jovovic, E. S. Toberer, A. Saramat, K. Kurosaki, A. Charoenphakdee, S. Yamanaka, and G. J. Snyder. Enhancement of thermoelectric efficiency in PbTe by distortion of the electronic density of states. *Science*, 321(5888):554–557, July 2008.

[7] D. M. Rowe, V. S. Shukla, and N. Savvides. Phonon scattering at grain boundaries in heavily doped fine-grained silicon-germanium alloys. *Nature*, 290(5809):765–766, April 1981.

[8] Y. Lan, A. J. Minnich, G. Chen, and Z. Ren. Enhancement of Thermoelectric Figure-of-Merit by a Bulk Nanostructuring Approach. *Advanced Functional Materials*, 20(3):357–376, Feb 2010.

[9] Y. Pei, N. A. Heinz, A. LaLonde, and G. J. Snyder. Combination of large nanostructures and complex band structure for high performance thermoelectric lead telluride. *Energy & Environmental Science*, 4(9):3640–3645, Sept 2011.

[10] Y. Pei, J. Lensch-Falk, E. S. Toberer, D. L. Medlin, and G. J. Snyder. High Thermoelectric Performance in PbTe Due to Large Nanoscale Ag_2Te Precipitates and La Doping. *Advanced Functional Materials*, 21(2):241–249, Jan 2011.

[11] T. Ikeda, N. J. Marolf, K. Bergum, M. B. Toussaint, N. A. Heinz, V. A. Ravi, and G. J. Snyder. Size control of Sb_2Te_3 Widmanstätten precipitates in thermoelectric PbTe. *Acta Materialia*, 59(7):2679–2692, 2011.

[12] T. Ikeda, V. A. Ravi, and G. J. Snyder. Formation of Sb_2Te_3 Widmanstätten precipitates in thermoelectric PbTe. *Acta Materialia*, 57(3):666–672, Feb 2009.

[13] H. J. Goldsmid. Bismuth telluride and some of its alloys. *G.E.C. Journal*, 29(3):158–167, 1962.

[14] Y. Feutelais, B. Legendre, N. Rodier, and V. Agafonov. A study of the phases in the bismuth - tellurium system. *Materials Research Bulletin*, 28(6):591–596, June 1993.

[15] R. J. Cava, H. Ji, M. K. Fuccillo, Q. D. Gibson, and Y. S. Hor. Crystal structure and chemistry of topological insulators. *Journal of Materials Chemistry C*, 1(19):3176–3189, 2013.

[16] O Madelung. *Semiconductors: Data Handbook*. Springer, 2004.

[17] L. L. Wang, M. Huang, S. Thimmaiah, A. Alam, S. L. Bud'ko, A. Kaminski, T. A. Lograsso, P. Canfield, and D. D. Johnson. Native defects in tetradymite $Bi_2(Te_xSe_{3-x})$ topological insulators. *Physical review B*, 87(12), March 2013.

[18] D. O. Scanlon, P. D. C. King, R. P. Singh, A. de la Torre, S. McKeown Walker, G. Balakrishnan, F. Baumberger, and C. R. A. Catlow. Controlling Bulk Conductivity in Topological Insulators: Key Role of Anti-Site Defects. *Advanced Materials*, 24(16):2154–2158, April 2012.

[19] D. M. Rowe, editor. *CRC handbook of thermoelectrics*. CRC Press, 1995.

[20] P. W. Bridgman. Certain physical properties of single crystals of tungsten, antimony, bismuth, tellurium, cadmium, zinc, and tin. *Proceedings of the American Academy of Arts and Sciences*, 60(1/14):305–383, Jun-Dec 1925.

[21] W. G. Pfann. *Zone Melting*. John Wiley & Sons, 1966.

[22] H. J. Goldsmid. The electrical conductivity and thermoelectric power of bismuth telluride. *Proceedings of the Physical Society of London*, 71(460):633–646, 1958.

[23] H. J. Goldsmid. The thermal conductivity of bismuth telluride. *Proceedings of the Physical Society of London section B*, 69(2):203–209, 1956.

[24] N. A. Heinz, T. Ikeda, and G. J. Snyder. Formation of highly oriented large nanoscale In_2Te_3 precipitates in bulk Bi_2Te_3. *Acta Materialia*, 60(11):4461–4467, June 2012.

[25] H. M. Rietveld. A profile refinement method for nuclear and magnetic structures. *Journal of Applied Crystallography*, 2:65–71, 1969.

[26] S. Iwanaga, E. S. Toberer, A. LaLonde, and G. J. Snyder. A high temperature apparatus for measurement of the Seebeck coefficient. *Review of Scientific Instruments*, 82(6), JUN 2011.

[27] D. Bessas, I. Sergueev, H. C. Wille, J. Persson, D. Ebling, and R. P. Hermann. Lattice dynamics in Bi_2Te_3 and Sb_2Te_3: Te and Sb density of phonon states. *Physical Review B*, 86(22), Dec 2012.

[28] Z. M. Gibbs, A. LaLonde, and G. J. Snyder. Optical band gap and the Burstein-Moss effect in iodine doped PbTe using diffuse reflectance infrared Fourier transform spectroscopy. *New Journal of Physics*, 15, July 2013.

[29] G. Schierning, R. Theissmann, N. Stein, N. Petermann, A. Becker, M. Engenhorst, V. Kessler, M. Geller, A. Beckel, H. Wiggers, and R. Schmechel. Role of oxygen on microstructure and thermoelectric properties of silicon nanocomposites. *Journal of Applied Physics*, 110(11):113515, 2011.

[30] D. L. Medlin and G. J. Snyder. Interfaces in bulk thermoelectric materials A review for Current Opinion in Colloid and Interface Science. *Current Opinion In Colloid & Interface Science*, 14(4):226–235, Aug 2009.

[31] B. Zhang, J. He, X. Ji, Terry M. Tritt, and Amar Kumbhar. Controlled two-dimensional coated nanostructures for bulk thermoelectric composites. *Applied Physics Letters*, 89(16):163114, 2006.

[32] P. N. Alboni, X. Ji, J. He, N. Gothard, and Terry M. Tritt. Thermoelectric properties of $La_{0.9}CoFe_3Sb_{12}CoSb_3$ skutterudite nanocomposites. *Journal of Applied Physics*, 103(11):113707, 2008.

[33] X. Ji, J. He, Z. Su, N. Gothard, and T.M. Tritt. Improved thermoelectric performance in polycrystalline p-type Bi_2Te_3 via an alkali metal salt hydrothermal nanocoating treatment approach. *Journal of Applied Physics*, 104(3):034907, 2008.

[34] W. G. Zeier, A. LaLonde, Z. M. Gibbs, C. P. Heinrich, M. Panthöfer, G. J. Snyder, and W. Tremel. Influence of a nano phase segregation on the thermoelectric properties of the p-type doped stannite compound $Cu_{2+x}Zn_{1-x}GeSe_4$. *Journal of the American Chemical Society*, 134(16):7147–54, April 2012.

[35] J. D. Embury and R. M. Fisher. The structure and properties of drawn pearlite. *Acta Metallurgica*, 14(2):147–159, Feb 1966.

[36] T. Ikeda, L. A. Collins, V. A. Ravi, F. S. Gascoin, S. M. Haile, and G. J. Snyder. Self-assembled nanometer lamellae of thermoelectric PbTe and Sb_2Te_3 with epitaxy-like interfaces. *Chemistry of Materials*, 19(4):763–767, Feb 2007.

[37] T. Ikeda, S. M. Haile, V. A. Ravi, H. Azizgolshani, F. Gascoin, and G. J. Snyder. Solidification processing of alloys in the pseudo-binary PbTe-Sb_2Te_3 system. *Acta Materialia*, 55(4):1227–1239, February 2007.

[38] T. Ikeda, V. A. Ravi, L. A. Collins, S. M. Haile, and G. J. Snyder. Development and Evolution of Nanostructure in Bulk Thermoelectric Pb-Te-Sb Alloys. *Journal of Electronic Materials*, 36(7):716–720, June 2007.

[39] T. Ikeda, V. A. Ravi, and G. J. Snyder. Microstructure Size Control through Cooling Rate in Thermoelectric PbTe-Sb_2Te_3 Composites. *Metallurgical and Materials Transactions A-Physical Metallurgy and Materials Science*, 41A(3):641–650, March 2010.

[40] G. A. Edwards, K. Stiller, G. L. Dunlop, and M. J. Couper. The precipitation sequence in Al-Mg-Si alloys. *Acta Materialia*, 46(11):3893–3904, July 1998.

[41] T. Ikeda, M. B. Toussaint, K. Bergum, S. Iwanaga, and G.J. Snyder. Solubility and formation of ternary Widmanstätten precipitates in PbTe in the pseudo-binary PbTe-Bi_2Te_3 system. *Journal of Materials Science*, 46(11):3846–3854, June 2011.

[42] K. A. Hunt, J. D. Jackson. Binary eutectic solidification. *Transactions of the Metallurgical Society of AIME*, 236(6):843–852, 1966.

[43] K. A. Jackson. Mechanism of growth. In *Liquid Metals and Solidification*, pages 174–186. American Society for Metals, Cleveland, Ohio, 1958.

[44] K. A. Jackson. Interface structure. In R. H. Doremus, B. W. Roberts, and D. Turnbull, editors, *Growth and Perfection of Crystals*, pages 319–324. John Wiley & Sons, New York, 1958.

[45] D. A. Pawlak, S. Turczynski, M. Gajc, K. Kolodziejak, R. Diduszko, K. Rozniatowski, J. Smalc, and I. Vendik. How Far Are We from Making Metamaterials by Self-Organization? The Mi-

crostructure of Highly Anisotropic Particles with an SRR-Like Geometry. *Advanced Functional Materials*, 20(7):1116–1124, March 2010.

[46] D. R. Lide, editor. *CRC handbook of chemistry and physics.* 2007.

[47] B. W. Howlett, S. Misra, and M. B. Bever. On the thermodynamic properties of the compounds Sb_2Se_3, Bi_2Se_3, Sb_2Te_3, and Bi_2Te_3. *Transactions of the Metallurgical Society of AIME*, 230(6):1367–1372, 1964.

[48] Shamsuddin. Thermodynamic investigations of lead telluride. *Materials Research Bulletin*, 12(1):7–12, Jan 1977.

[49] O. Kubaschewski, C. B. Alcock, and P. J. Spencer. *Materials Thermo-Chemistry.* Pergamon Press, 6 edition, 1993.

[50] C. W. Bale, E. Bélisle, P. Chartrand, S. A. Decterov, G. Eriksson, K. Hack, I. H. Jung, Y. B. Kang, J. Melançon, A. D. Pelton, C. Robelin, and S. Petersen. FactSage thermochemical software and databases recent developments. *Calphad*, 33(2):295–311, June 2009.

[51] K. J. Lee, C. H. Lee, G. W. Lee, W. S. Hwang, C. H. Lee, S. Yoda, and W. S Cho. Thermophysical properties of $BaTiO_3$ ceramics prepared by aerodynamic levitation. *Thermochimica Acta*, 542:37–41, Aug 2012.

[52] B. Wei, D.M. Herlach, B. Feuerbacher, and F. Sommer. Dendritic and eutectic solidification of undercooled Co-Sb alloys. *Acta Metallurgica et Materialia*, 41(6):1801–1809, June 1993.

[53] L. Liu, J. F. Li, and Y. H. Zhou. Solidification interface morphology pattern in the undercooled Co-24.0 at.% Sn eutectic melt. *Acta Materialia*, 59(14):5558–5567, Aug 2011.

[54] W. A. Tiller, K. A. Jackson, J. W. Rutter, and B. Chalmers. The redistribution of solute atoms during the solidification of metals. *Acta Metallurgica*, 1(4):428–437, July 1953.

[55] K. Kuniyoshi, K. Ozono, M. Ikeda, T. Suzuki, S. G. Kim, and W. T. Kim. Faceted dendrite growth of silicon from undercooled melt of Si-Ni alloy. *Science and Technology of Advanced Materials*, 7(6):595–600, 2006.

[56] B. Chalmers. *Principles of Solidification.* John Wiley & Sons, 1964.

[57] H. J. Wu, S. W. Chen, T. Ikeda, and G. J. Snyder. Formation of ordered nano-wire microstructures in thermoelectric PbAgSbTe. *Acta Materialia*, 60(3):1129–1138, Feb 2012.

[58] H. J. Wu, W. J. Foo, S. W. Chen, and G. J. Snyder. Ternary eutectic growth of nanostructured thermoelectric Ag-Pb-Te materials. *Applied Physics Letters*, 101(2):023107, 2012.

[59] J. W. Cahn. Phase Separation by Spinodal Decomposition in Isotropic Systems. *The Journal of Chemical Physics*, 42(1):93, 1965.

[60] G. A. Chadwick. Eutectic alloy solidification. *Progress in Materials Science*, 12:99–182, Jan 1963.

[61] S. Gorsse, P. Bauer Pereira, R. Decourt, and E. Sellier. Microstructure Engineering Design for Thermoelectric Materials: An Approach to Minimize Thermal Diffusivity. *Chemistry of Materials*, 22(3):988–993, Feb 2010.

[62] D. Cheetham and N. Ridley. The kinetics of isothermal and isovelocity pearlite growth in Cu-Al eutectoid alloy. *Metallurgical Transactions*, 4(11):2549–2556, Nov 1973.

[63] J. D. Livingston. Unidirectional solidification of eutectic and eutectoid alloys. *Journal of Crystal Growth*, 24-25:94–101, Oct 1974.

[64] J. D. Livingston and J. W. Cahn. Discontinuous coarsening of aligned eutectoids. *Acta Metallurgica*, 22(4):495–503, April 1974.

[65] F. M. A. Carpay. The preparation of aligned composite materials by unidirectional solid-state decomposition. *Acta Metallurgica*, 18(7):747–752, July 1970.

[66] F. R. Nabarro. The influence of elastic strain on the shape of particles segregating in an alloy. *Proceedings of the Physical Society*, 52(1):90–93, Jan 1940.

[67] R. D. Doherty. *Physical Metallurgy*, volume II. North-Holland, 1996.

[68] X. Chen, S. Cao, T. Ikeda, V. Srivastava, D. Snyder, G. J.and Schryvers, and R. D. James. A weak compatibility condition for precipitation with application to the microstructure of pbte-sb2te3 thermoelectrics. *Acta Materialia*, 59(15):6124–6132, Sept 2011.

[69] Y. Feutelais, G. Morgant, and J. R. Didry. Thermodynamic evaluation of the system bismuth-antimony. *Calphad-Computer Coupling of Phase Diagrams and Thermochemistry*, 16(2):111–119, 1992.

[70] H. Okamoto. *Binary Alloy Phase Diagrams*, volume 1. ASM International, 2nd edition, 1990.

[71] N. A. Heinz, T. Ikeda, G. J. Snyder, and D. L. Medlin. Interfacial Disconnections at Sb_2Te_3 Precipitates in PbTe: Mechanisms of Strain Accommodation and Phase Transformation at a Tetradymite/Rocksalt Telluride Interface. *Acta Materialia*, 59(20):7724–7735, Dec 2011.

[72] D. L. Medlin and J. D. Sugar. Interfacial defect structure at Sb_2Te_3 precipitates in the thermoelectric compound $AgSbTe_2$. *Scripta Materialia*, 62(6):379–382, March 2010.

[73] J. L. Lensch-Falk, J. D. Sugar, M. A. Hekmaty, and D. L. Medlin. Morphological evolution of Ag_2Te precipitates in thermoelectric PbTe. *Journal of Alloys and Compounds*, 504:37–44, 2010.

[74] N. Savvides and H. J. Goldsmid. Boundary scattering of phonons in fine-grained hot-pressed Ge-Si alloys. II. Theory. *Journal of Physics C: Solid State Physics*, 13(25):4671–4678, Sept 1980.

[75] N. Savvides and H. J. Goldsmid. Boundary scattering of phonons in fine-grained hot-pressed Ge-Si alloys. I. The dependence of lattice thermal conductivity on grain size and porosity. *Journal of Physics C: Solid State Physics*, 13(25):4657–4670, Sept 1980.

[76] C. Dames and G. Chen. *Thermoelectrics Handbook: Macro to Nano.* Taylor & Francis, 2006.

[77] M. Zebarjadi, K. Esfarjani, M. S. Dresselhaus, Z. F. Ren, and G. Chen. Perspectives on Thermoelectrics: From Fundamentals to Device Applications. *Energy & Environmental Science*, 5:5147–5162, 2012.

[78] A. J. Minnich, M. S. Dresselhaus, Z. F. Ren, and G. Chen. Bulk nanostructured thermoelectric materials: current research and future prospects. *Energy & Environmental Science*, 2(5):466–479, 2009.

[79] M. G. Kanatzidis. Nanostructured thermoelectrics: The new paradigm? *Chemistry of Materials*, 22(3):648–659, Feb 2010.

[80] C. B. Vining, W. Laskow, J. O. Hanson, R. R. Van der Beck, and P. D. Gorsuch. Thermoelectric properties of pressure-sintered $Si_{0.8}Ge_{0.2}$ thermoelectric alloys. *Journal of Applied Physics*, 69(8):4333, 1991.

[81] H. Jones. Microstructure of rapidly solidified materials. *Materials Science and Engineering*, 65(1):145–156, July 1984.

[82] D. Bouchard and J. S. Kirkaldy. Prediction of dendrite arm spacings in unsteady-and steady-state heat flow of unidirectionally solidified binary alloys. *Metallurgical and Materials Transactions B*, 28(4):651–663, Aug 1997.

[83] C. Zener. Kinetics of the decomposition of austenite. *Transactions of the American Institute of Mining and Metallurgical Engineers*, 167:550–595, 1946.

[84] H. Jones. Splat cooling and metastable phases. *Reports on Progress in Physics*, 36(11):1425–1497, Nov 1973.

[85] H. H. Liebermann. The dependence of the geometry of glassy alloy ribbons on the chill block melt-spinning process parameters. *Materials Science and Engineering*, 43(3):203–210, May 1980.

[86] A. L. Greer. Metallic glasses. *Science (New York, N.Y.)*, 267(5206):1947–53, March 1995.

[87] W. Xie, X. Tang, Y. Yan, Q. Zhang, and T. M. Tritt. Unique nanostructures and enhanced thermoelectric performance of melt-spun BiSbTe alloys. *Applied Physics Letters*, 94(10):102111, 2009.

[88] H. Li, X. Tang, X. Su, Q. Zhang, and C. Uher. Nanostructured bulk Yb_x $\mathrm{Co}_4\mathrm{Sb}_{12}$ with high thermoelectric performance prepared by the rapid solidification method. *Journal of Physics D: Applied Physics*, 42(14):145409, July 2009.

[89] C. Yu, T. J. Zhu, K. Xiao, J. J. Shen, S. H. Y., and X. B. Zhao. Reduced Grain Size and Improved Thermoelectric Properties of Melt Spun (Hf,Zr)NiSn Half-Heusler Alloys. *Journal of Electronic Materials*, 39(9):2008–2012, Dec 2009.

[90] S. Y. Wang, W. J. Xie, H. Li, X. F. Tang, and Q. J. Zhang. Effects of Cooling Rate on Thermoelectric Properties of n-Type $\mathrm{Bi}_2(\mathrm{Se}_{0.4}\mathrm{Te}_{0.6})_3$ Compounds. *Journal of Electronic Materials*, 40(5):1150–1157, March 2011.

[91] A. Jacquot, T. Jürgen, J. Schumann, M. Jägle, H. Böttner, T. Gemming, J. Schmidt, and D. Ebling. $(\mathrm{Bi,Sb})_2\mathrm{Te}_3$-PbTe chalcogenide alloys: Impact of the cooling rate and sintering parameters on the microstructures and thermoelectric performances. *Journal of Materials Research*, 26(15):1773–1784, May 2011.

[92] L. D. Graham and R. W. Kraft. Coarsening of eutectic microstructures at elevated temperatures. *Transactions of the Metallurgical Society of AIME*, 236(1):94–102, 1966.

[93] H. E. Cline. Shape instabilities of eutectic composites at elevated temperatures. *Acta Metallurgica*, 19(6):481–490, June 1971.

[94] A. N. Kolmogorov. Zur Statistik der Kristallisations-vorgänge in Metallen. *Izv. Akad. Nauk SSSR Ser. Mat.*, 1(3):355–359, 1937.

[95] W. A. Johnson and R. F. Mehl. Reaction kinetics in processes of nucleation and growth. *Transactions of the American Institute of Mining and Metallurgical Engineers*, 135:416–442, 1939.

[96] M. Avrami. Kinetics of Phase Change. I General Theory. *The Journal of Chemical Physics*, 7(12):1103, 1939.

[97] M. Avrami. Kinetics of Phase Change. II Transformation-Time Relations for Random Distribution of Nuclei. *The Journal of Chemical Physics*, 8(2):212, Feb 1940.

[98] M. Avrami. Granulation, Phase Change, and Microstructure Kinetics of Phase Change. III. *The Journal of Chemical Physics*, 9(2):177, 1941.

[99] F. Yang, T. Ikeda, G. J. Snyder, and C. Dames. Effective thermal conductivity of polycrystalline materials with randomly oriented superlattice grains. *Journal of Applied Physics*, 108, Aug 2010.

[100] T. Ikeda, V. A. Ravi, and G. J. Snyder. Evaluation of true interlamellar spacing from microstructural observations. *Journal of Materials Research*, 23(09):2538–2544, Jan 2011.

[101] H. K. Hardy and T. J. Heal. Report on precipitation. *Progress in Metal Physics*, 5:143–278, Jan 1954.

[102] J. L. Burns. Classification of alpha iron-nitrogen and alpha iron-carbon, as age-hardening alloys. *Transactions of the American Institute of Mining and Metallurgical Engineers*, 113:239–261, 1934.

[103] P. D. Merica, R. G. Waltenberg, and H. Scott. Heat treatment and constitution of duralumin. *Transactions of the American Institute of Mining and Metallurgical Engineers*, 64:41–77, 1921.

[104] K. Bergum, T. Ikeda, and G. J. Snyder. Solubility and microstructure in the pseudo-binary PbTe-Ag_2Te system. *Journal of Solid State Chemistry*, 184(9):2543–2552, Sept 2011.

[105] D. A. Porter and K. E. Easterling. *Phase Transformations in Metals and Alloys.* CRC Press, 2 edition, 2001.

[106] M. S. Jeng, R. Yang, D. Song, and G. Chen. Modeling the thermal conductivity and phonon transport in nanoparticle composites using Monte Carlo simulation. *Journal of Heat Transfer-Transactions of the ASME*, 130(4):42410, April 2008.

[107] K. C. Russell. Nucleation in solids: The induction and steady state effects. *Advances in Colloid and Interface Science*, 13(3-4):205–318, Sept 1980.

[108] D. Turnbull. Metastable structures in metallurgy. *Metallurgical Transactions A*, 12(5):695–708, May 1981.

[109] Y. F. Ouyang, X. P. Zhong, and W. M. Wu. Extended solid solubility for Al-W binary system by mechanical alloying. *Science In China Series A-Mathematics Physics Astronomy*, 43(2):180–184, Feb 2000.

[110] J. Eckert, L. Schultz, and K. Urban. Synthesis of Ni-Ti and Fe-Ti alloys by mechanical alloying: formation of amorphous phases and extended solid solutions. *Journal of Non-Crystalline Solids*, 127(1):90–96, Jan 1991.

[111] J. Xu, J. H. He, and E. Ma. Effect of milling temperature on mechanical alloying in the immiscible Cu-Ta system. *Metallurgical and Materials Transactions A*, 28(7):1569–1580, July 1997.

[112] T. Ikeda, L. Haviez, Y. Li, and G. J. Snyder. Nanostructuring of thermoelectric Mg_2Si via a nonequilibrium intermediate state. *Small*, 8(15):2350–5, Aug 2012.

[113] J. W. Cahn and R. L. Fullman. On the use of lineal analysis for obtaining particle size distribution functions in opaque samples. *Transactions of the American Institute of Mining and Metallurgical Engineers*, 206(5):610–612, 1956.

[114] J. He, S. N. Girard, M. G. Kanatzidis, and V. P. Dravid. Microstructure-Lattice Thermal Conductivity Correlation in Nanostructured $PbTe_{0.7}S_{0.3}$ Thermoelectric Materials. *Advanced Functional Materials*, 20(5):764–772, March 2010.

[115] J. Callaway and H. von Baeyer. Effect of Point Imperfections on Lattice Thermal Conductivity. *Physical Review*, 120(4):1149–1154, Nov 1960.

[116] J. C. Russ. *Practical Stereology.* Plenum Press, 1986.

[117] B. D. Cullity and S. R. Stock. *Elements of x-ray diffraction.* Prentice Hall, 3 edition, 2001.

[118] Y. Pei, X. Shi, A. LaLonde, H. Wang, L. Chen, and G. J. Snyder. Convergence of electronic bands for high performance bulk thermoelectrics. *Nature*, 473(7345):66–9, May 2011.

[119] G. V. Semenova, T. P. Sushkova, and V. S. Gorshkov. Solid solubility in the Bi-Sb-As ternary system. *Russian Journal of Inorganic Chemistry*, 51(9):1504–1508, Sept 2006.

[120] N. A. Heinz, S. Howell, H. Wang, T. Ikeda, and G. J. Snyder. Hot pressing and nanostructuring of $Bi_{90}Sb_{10}$ alloys to concurrently improve mechanical and thermoelectric properties. *Physica Status Solidi (a)*, pages 2565–2569, 2012.

[121] S. V. Barabash, V. Ozolins, and C. Wolverton. First-principles theory of competing order types, phase separation, and phonon spectra in thermoelectric $AgPb_mSbTe_{m+2}$ alloys. *Physical Review Letters*, 101(15), 2008.

[122] S. V. Barabash, V. Ozolins, and C. Wolverton. First-principles theory of the coherency strain, defect energetics, and solvus boundaries in the $PbTe-AgSbTe_2$ system. *Physical Review B*, 78(21), 2008.

[123] G. S. Pomrehn, E. S. Toberer, G. J. Snyder, and A. van de Walle. Entropic stabilization and retrograde solubility in Zn_4Sb_3. *Physical Review B*, 83(9), 2011.

[124] Y. Pei, H. Wang, and G. J. Snyder. Band Engineering of Thermoelectric Materials. *Advanced Materials*, Oct 2012.

[125] Y. Pei, N. A. Heinz, and G. J. Snyder. Alloying to increase the band gap for improving thermoelectric properties of Ag_2Te. *Journal of Materials Chemistry*, 21(45):18256, 2011.

[126] Y. Pei, H. Wang, Z. M. Gibbs, A. D. LaLonde, and G. J. Snyder. Thermopower enhancement in $Pb_{1x}Mn_xTe$ alloys and its effect on thermoelectric efficiency. *NPG Asia Materials*, 4(9):e28, Sept 2012.

[127] Y. Pei, A. D. LaLonde, N. A. Heinz, and G. J. Snyder. High Thermoelectric Figure of Merit in PbTe Alloys Demonstrated in PbTe-CdTe. *Advanced Energy Materials*, 2(6):670–675, June 2012.

[128] Stabilizing the optimal carrier concentration for high thermoelectric efficiency. *Advanced Materials*, 23(47):5674–8, Dec 2011.

[129] R. Feigelson, editor. *50 Years Progress in Crystal Growth.* Elsevier, 2004.

[130] W. G. Pfann. Principles of zone-melting. *Transactions of the American Institute of Mining and Metallurgical Engineers*, 194(7):747–753, 1952.

[131] G. J. Snyder and E. S. Toberer. Complex thermoelectric materials. *Nature Materials*, 7(2):105–114, Feb 2008.

[132] Ioffe, A. F. *Semiconductor thermoelements and thermoelectric cooling.* Infosearch, 1957.

[133] Slack, G. A. *Solid State Physics*, volume 34. Academic Press, 1979.

[134] A. J. Minnich and G. Chen. Modified effective medium formulation for the thermal conductivity of nanocomposites. *Applied Physics Letters*, 91(7), Aug 2007.

[135] G. Chen. Thermal conductivity and ballistic-phonon transport in the cross-plane direction of superlattices. *Physical Review B*, 57(23):14958–14973, June 1998.

[136] S. N. Girard, J. He, X. Zhou, D. Shoemaker, C. M. Jaworski, C. Uher, V. P. Dravid, J. P. Heremans, and M. G. Kanatzidis. High performance na-doped pbte-pbs thermoelectric materials: Electronic density of states modification and shape-controlled nanostructures. *Journal of the American Chemical Society*, 133(41):16588–16597, Oct 2011.

[137] D. G. Ebling, A. Jacquot, H. Böettner, L. Kirste, J. Schmidt, and M. Aguirre. Influence of Group IV-Te Alloying on Nanocomposite Structure and Thermoelectric Properties of Bi_2Te_3 Compounds. *Journal of Electronic Materials*, 38(7):1450–1455, July 2009.

[138] L. R. Scherpereel, P. L. Palumbo, and E. A. Peretti. Quasibinary System In_2Te_3-Bi_2Te_3. *Journal of the Less-Common Metals*, 14(1):41–46, 1968.

[139] A. J. Rosenberg and A. J. Strauss. Solid Solutions of In_2Te_3 in Sb_2Te_3 and Bi_2Te_3. *Journal of Physics and Chemistry of Solids*, 19(1-2):105–116, 1961.

[140] A. I. Zaslavskii and V. M. Sergeeva. The polymorphism of In_2Te_3. *Soviet Physics-Solid State*, 2(11):2556–2561, 1961.

[141] R. O. Carlson. Anisotropic diffusion of copper into bismuth telluride. *Journal of Physics and Chemistry of Solids*, 13(1-2):65–70, 1960.

[142] J. D. Keys and H. M. Dutton. Diffusion and solid solubility of silver in single-crystal bismuth telluride. *Journal of Physics and Chemistry of Solids*, 24(4):563–571, 1963.

[143] J. D. Keys and H. M. Dutton. Diffusion and solid solubility of gold in single-crystal bismuth telluride. *Journal of Applied Physics*, 34(6):1830–1831, 1963.

[144] T. G. Zocco and M. R. Plichta. Comparison of solute fluxes during concurrent size and shape coarsening of plate shaped precipitates. *Scripta Metallurgica*, 18(6):555–560, 1984.

[145] T. Karakostas and N. A. Economou. Ordered phases of in_2te_3. *Physica Status Solidi A-Applied Research*, 31(1):89–99, 1975.

[146] T. Karakostas, N. F. Flevaris, N. Vlachavas, G. L. Bleris, and N. A. Economou. Ordered State of In_3Te_4. *Acta Crystallographica Section a*, 34(Jan):123–126, 1978.

[147] G. L. Bleris, T. Karakostas, N. A. Economou, and R. Deridder. Ordered state of In_2Te_3 and its relation to the transition-state. *Physica Status Solidi A-Applied Research*, 50(2):579–586, 1978.

[148] G. L. Bleris and N. A. Economou. Thermodynamic study of the order-disorder transformation for the do_{22} structure of α-in_2te_3. *Physical Review B*, 21(7):2999–3004, 1980.

[149] J. C. Woolley and B. R. Pamplin. The ordered crystal structure of in_2te_3. *Journal of the Less-Common Metals*, 1(5):362–376, 1959.

[150] E. S. Toberer, A. Zevalkink, and G. J. Snyder. Phonon engineering through crystal chemistry. *Chemistry of Materials*, 21:15843–15852, 2011.

[151] H. J. Goldsmid. Recent studies of bismuth telluride and its alloys. *Journal of Applied Physics*, 32:2198–2202, 1961.

[152] T. Caillat, L. Gailliard, H. Scherrer, and S. Scherrer. Transport-properties analysis of single-crystals $(Bi_xSb_{1-x})_2Te_3$ grown by the traveling heater method. *Journal of Physics and Chemistry of Solids*, 54(5):575–581, May 1993.

[153] M. Carle, P. Pierrat, C. Lahalle-Gravier, S. Scherrer, and H. Scherrer. Transport-properties of n-type $Bi_2(Te_{1-x}Se_x)_3$ single-crystal solid-solutions ($x \leq 0.05$). *Journal of Physics and Chemistry of Solids*, 56(2):201–209, Feb 1995.

[154] X. Huang, X. Wang, and B. Cook. Coherent nanointerfaces in thermoelectric materials. *Journal of Physical Chemistry C*, 114(49):21003–21012, Dec 2010.

[155] J. D. Sugar and D. L. Medlin. Precipitation of ag_2te in the thermoelectric material $agsbte_2$. *Journal of Alloys and Compounds*, 47(8):75–82, 2009.

[156] S. R. Bhavsar, G. R. Pandya, S. M. Vyas, K. R. Shah, and P. H. Soni. Transport properties of $In_xBi_{2-x}Te_3$ ($x = 0.1 - 0.5$) crystals. *Proceedings of the Tenth International Workshop on the Physics of Semiconductor Devices*, pages 699–701, 2000.

[157] L. Jansa, P. Lostak, J. Sramkova, and J. Horak. The change of the electric conductivity type in crystals of $Bi_{2-x}In_xTe_3$ solid solutions. *Journal of Materials Science*, 27(22):6062–6066, Nov 1992.

[158] K. Kurata and T. Hirai. Semiconducting properties of several III_B-V_B-VI_B ternary materials and their metallurgical aspects. *Solid-State Electronics*, 9(6):633–640, 1966.

[159] J. Horak, S. Karamazov, and P. Lostak. Point-defects in $m_{(2-X)}in_{(X)}te_{(3)}$ (m = sb or bi) crystals. *Philosophical Magazine B*, 72(6):627–636, Dec 1995.

[160] S. Karamazov, P. Lostak, J. Horak, and R. Kuzel. Point-defects in $Bi_{2-x}In_xTe_3$ single-crystals. *Physica Status Solidi A-Applied Research*, 148(1):229–237, March 1995.

[161] D. G. Cahill, S. K. Watson, and R. O. Pohl. Lower limit to the thermal-conductivity of disordered crystals. *Physical Review B*, 46(10):6131–6140, Sept 1992.

[162] J. Horak, J. Navratil, and Z. Stary. Lattice point-defects and free-carrier concentration in $Bi_{2+x}Te_3$ and $Bi_{2+x}Se_3$. *Journal of Physics and Chemistry of Solids*, 53(8):1067–1072, Aug 1992.

[163] J. P. Fleurial, L. Gaillard, R. Triboulet, H. Scherrer, and S. Scherrer. Thermal-properties of high-quality single-crystals of bismuth telluride. 1. Experimental characterization. *Journal of Physics and Chemistry of Solids*, 49(10):1237–1247, 1988.

[164] J. P. Fleurial, L. Gaillard, R. Triboulet, H. Scherrer, and S. Scherrer. Thermal-properties of high-quality single-crystals of bismuth telluride. 2. Mixed-scattering model. *Journal of Physics and Chemistry of Solids*, 49(10):1249–1257, 1988.

[165] N. A. Heinz, T. Ikeda, Y. Pei, and G. J. Snyder. Applying quantitative microstructure control in advanced functional composites. *Advanced Functional Materials*, 24(15):2135–2153, April 2014.

[166] H. Kohler. Non-parabolic E(k) relation of lowest conduction-band in Bi_2Te_3. *Physica Status Solidi B-Basic Research*, 73(1):95–104, 1976.

[167] Y. Pei, A. D. LaLonde, H. Wang, and G. J. Snyder. Low effective mass leading to high thermoelectric performance. *Energy & Environmental Science*, 5(7):7963–7969, July 2012.

[168] J. G. Goudot, A., Schlicklin, P. M., Stockholm. Thermoelectric material characterization at 300 K. *5th International Conference on Thermoelectric Energy Conversion*, pages 49–55, 1984.

[169] J. Martin. Protocols for the high temperature measurement of the Seebeck coefficient in thermoelectric materials. *Measurement Science & Technology*, 24(8), Aug 2013.

[170] M. P. Banaga, O. B. Sokolov, T. E. Benderskaya, L. D. Dudkin, A. B. Ivanova, and I. I. Fridman. Peculiarities of the structure and thermoelectric properties of $Bi_{0.88}Sb_{0.12}$. *Inorganic Materials*, 22(4):540–543, April 1986.

[171] G. Cochrane and W. V. Youdelis. Transport and thermoelectric properties of bismuth and Bi-12 at pct Sb alloy powder compacts. *Metallurgical Transactions*, 3(11):2843–2850, 1972.

[172] H. J. Goldsmid and E. H. Volckmann. Galvanomagnetic and thermoelectric measurements on polycrystalline $bi_{88}sb_{12}$. *Proceedings of the XVI International Conference on Thermoelectrics*, pages 171–175, 1997.

[173] E. H. Volckmann, H. J. Goldsmid, and J. W. Sharp. Observation of the effect of grain size on the lattice thermal conductivity of polycrystalline bismuth antimony. *Proceedings of the XV International Conference on Thermoelectrics*, pages 22–26, 1996.

[174] V. M. Grabov, O. N. Uryupin, and V. A. Komarov. Thermoelectric properties of polycrystalline bismuth and bismuth-antimony alloys. *Proceedings of the XVII International Conference on Thermoelectrics*, pages 138–140, 1998.

[175] R. Martin-Lopez, A. Dauscher, H. Scherrer, J. Hejtmanek, H. Kenzari, and B. Lenoir. Thermoelectric properties of mechanically alloyed Bi-Sb alloys. *Applied Physics A-Materials Science & Processing*, 68(5):597–602, May 1999.

[176] Y. Suse, Y. H. Lee, H. Morimoto, T. Koyonagi, K. Matsubara, and Y. Kawamoto. Structure and thermoelectric properties of $Bi_{88}Sb_{12}$ ceramics using fine particles produced by hydrogen arc-plasma. *Proceedings of the XII International Conference on Thermoelectrics*, pages 248–251, 1993.

[177] B. Lenoir, A. Dauscher, X. Devaux, R. Martin-Lopez, Y. I. Ravich, H. Scherrer, and S. Scherrer. Bi-Sb alloys: An update. *Proceedings of the XV International Conference on Thermoelectrics*, pages 1–13, 1996.

[178] J. W. Sharp, E. H. Volckmann, and H. J. Goldsmid. The thermal conductivity of polycrystalline $bi_{88}sb_{12}$. *Physica Status Solidi A-Applied Research*, 185(2):257–265, June 2001.

[179] E. Zoro, C. Servant, and B. Legendre. Thermodynamic modeling of the Ag-Au-Sb ternary system. *Journal of Phase Equilibria and Diffusion*, 28(3):250–257, June 2007.

[180] B. Lenoir, M. Cassart, J. P. Michenaud, H. Scherrer, and S. Scherrer. Transport properties of bi-rich bi-sb alloys. *Journal of Physics and Chemistry of Solids*, 57(1):89–99, Jan 1996.

[181] I. Ansara, C. Chatillon, H. L. Lukas, T. Nishizawa, H. Ohtani, K. Ishida, M. Hillert, B. Sundman, B. B. Argent, A. Watson, T. G. Chart, and T. Anderson. A binary database for III-V compound semiconductor systems. *Calphad-Computer Coupling of Phase Diagrams and Thermochemistry*, 18(2):177–222, 1994.

[182] P. Cucka and C. S. Barrett. Crystal structure of Bi and of solid solutions of Pb, Sn, Sb, and Te in Bi. *Acta Crystallographica*, 15(Sept):865–872, 1962.

[183] C. S. Barrett, P. Cucka, and K. Haefner. Crystal structure of antimony at 4.2, 78 and 298°k. *Acta Crystallographica*, 16(6):451–453, 1963.

[184] D. Schiferl and C. S. Barrett. Crystal structure of arsenic at 4.2, 78 and 299°K. *Journal of Applied Crystallography*, 2:30–36, 1969.

[185] K. F. Hsu, S. Loo, F. Guo, W. Chen, J.S. Dyck, C. Uher, T. Hogan, E.K. Polychroniadis, and M.G. Kanatzidis. Cubic $AgPb_mSbTe_{2+m}$: bulk thermoelectric materials with high figure of merit. *Science*, 303(5659):818–821, Feb 2004.

[186] T. Ikeda, E. S. Toberer, V. A. Ravi, G. J. Snyder, S. Aoyagi, E. Nishibori, and M. Sakata. In situ observation of eutectoid reaction forming a pbte-sb_2te_3 thermoelectric nanocomposite by synchrotron x-ray diffraction. *Scripta Materialia*, 60(5):321–324, March 2009.

[187] D. G. Ebling, A. Jacquot, M. Jagle, H. Böettner, U. Kuhn, and L. Kirste. Structure and thermoelectric properties of nanocomposite bismuth telluride prepared by melt spinning or

by partially alloying with IV-VI compounds. *Physica Status Solidi-Rapid Research Letters*, 1(6):238–240, Nov 2007.

[188] H. Böettner, D. Ebling, A. Jacquot, U. Kuehn, and J. Schmiidt. Melt spinning preparation of bismuth telluride and partially alloying with IV-VI compounds for thermoelectric application. In *Thermoelectric power generation*, volume 1044 of *Materials research society symposium proceedings*, pages 115–120. Materials research society, 2008.

[189] J. D. Sugar and D. L. Medlin. Solid-state precipitation of stable and metastable layered compounds in thermoelectric $AgSbTe_2$. *Journal of Materials Science*, 46(6):1668–1679, March 2011.

[190] P. A. Sharma, J. D. Sugar, and D. L. Medlin. Influence of nanostructuring and heterogeneous nucleation on the thermoelectric figure of merit in $AgSbTe_2$. *Journal of Applied Physics*, 107(11):113716, June 2010.

[191] S. N. Zhang, T. J. Zhu, S. H. Yang, C. Yu, and X. B. Zhao. Phase compositions, nanoscale microstructures and thermoelectric properties in $Ag_{2-y}Sb_yTe_{1+y}$ alloys with precipitated Sb_2Te_3 plates. *Acta Materialia*, 58(12):4160–4169, July 2010.

[192] R. W. Armstrong, Jr. Faust, J. W., and W. A. Tiller. A structural study of the compound $AgSbTe_2$. *Journal of Applied Physics*, 31(11):1954–1959, Nov 1960.

[193] J. P. Hirth and R. C. Pond. Steps, dislocations and disconnections as interface defects relating to structure and phase transformations. *Acta Materialia*, 44(12):4749–4763, Dec 1996.

[194] T. L. Anderson and H. B. Krause. Refinement of Sb_2Te_3 and Sb_2Te_2Se structures and their relationship to nonstoichiometric $Sb_2Te_{3-y}Se_y$ compounds. *Acta Crystallographica Section B-Structural Science*, B 30(MAY15):1307–1310, 1974.

[195] H. Berger, A. Lehmann, and M. Schenk. Lattice-parameter variations in pbte single-crystals. *Crystal Research and Technology*, 20(4):579–581, 1985.

[196] V. Munoz, A. Lasbley, S. Klotz, and R. Triboulet. Synthesis and growth of PbTe crystals at low temperature and their characterization. *Journal of Crystal Growth*, 196(1):71–76, Jan 1999.

[197] T. Ikeda, E. S. Toberer, V. A. Ravi, S. M. Haile, and G. J. Snyder. Lattice thermal conductivity of self-assembled PbTe-Sb_2Te_3 composites with nanometer lamellae. In Kim, I, editor, *Proceedings ICT 07: Twenty-Sixth International Conference on Thermoelectrics*, International Conference on Thermoelectrics, pages 1–4. IEEE, 2008.

[198] R. C. Pond. *Dislocations in Solids.* Elsevier Science Publishers, 1989.

[199] R. C. Pond, S. Celotto, and J. P. Hirth. A comparison of the phenomenological theory of martensitic transformations with a model based on interfacial defects. *Acta Materialia*, 51(18):5385–5398, Oct 2003.

[200] D. L. Medlin, D. Cohen, and R. C. Pond. Accommodation of coherency strain by interfacial disconnections at a 90 degrees $< 110 >$ grain boundary in gold. *Philosophical Magazine Letters*, 83(4):223–232, 2003.

[201] N. Frangis, S. Kuypers, C. Manolikas, G. Vantendeloo, J. Vanlanduyt, and S. Amelinckx. Continuous series of one-dimensional structures in compounds based M_2X_3 (M = Sb, Bi, X = Se, Te). *Journal of Solid State Chemistry*, 84(2):314–334, February 1990.

[202] R. C. Pond and J. P. Hirth. Defects at surfaces and interfaces. *Solid State Physics - Advances In Research and Applications, Vol 47*, 47:287–365, 1994.

[203] R. C. Pond, D. L. Medlin, and A. Serra. A study of the accommodation of coherency strain by interfacial defects at a grain boundary in gold. *Philosophical Magazine*, 86(29-31):4667–4684, Oct-Nov 2006.